Ministère de l'Enseignement Supérieur et de la Recherche Scientifique
Université Hassiba Benbouali de Chlef
Faculté des Sciences Exactes et Informatique
Département de Physique

THÈSE

Présentée pour l'obtention du diplôme de

DOCTORAT

Filière : Physique

Spécialité : Physique des Matériaux

Par

Tariq HADJI

Thème :

Étude des propriétés de transports magnéto-électronique et thermo-électrique dans les composés full-Heusler à base des métaux alcalins

Soutenue le 21/06/2022, devant le jury composé de :

Mohamed BENAROUS	Professeur	Université de Chlef	Président
Hafid KHALFOUN	Professeur	Université de Chlef	Rapporteur
Habib RACHED	Professeur	Université de Chlef	Co-rapporteur
Samiha DERGAL	MCA	Université de Chlef	Examinateur
Ali BENTOUAF	Professeur	Université de Saida	Examinateur
Mostefa DJERMOUNI	MCA	Université de Relizane	Examinateur

Doctoral Thesis in Physics

Study of magneto-electronic and thermoelectric properties in full-Heusler compounds based on alkali metals

Tariq Hadji

June 21, 2022

Hassiba Benbouali University of Chlef
Faculty of Exact Sciences and Informatics
Department of Physics

Acknowledgements

I praise ALLAH and thank him for everything, for the blessing of health and reason, and for the strength and patience in accomplishing this work.

After that, I would like to take advantage of this occasion to thank everyone who contributed to the completion of this Thesis, and so I ask ALLAH to reward them well. I begin by extending my sincere thanks to my supervisor, Prof. Dr. Hafid Khalfoun, for guiding my thesis project, as well as for all his constant help and advice. I am very thankful to Prof. Dr. Habib Rached for proposing me the interesting topic of this Thesis, and for his co-supervision.

I would like to thank Prof. Dr. Mohamed Benarous for accepting the presidency of the jury. I would also like to thank the referees, Dr. Samiha Dergal, Prof. Dr. Ali Bentouaf and Dr. Mostefa Djermouni for their acceptance to participate in the formation of the jury to examine and judge this work.

I want to thank my colleague, Dr. Ahmed Azzouz-Rached for his friendship and the helpful discussions I had with him all these years. Also, without forgetting, I would like to thank Leyla Belouari for her administrative support.

Of course, all kinds of help from my family will always make me grateful to them. Finally, I thank everyone who contributed in one way or another to this Thesis and was not mentioned for some reason or because I forgot.

Abstract

This work intends to study from the first principles the structural stability, electronic, magnetic and thermoelectric properties of the new hypothetical full-Heusler compounds Mn_2LiZ (Si, Ge, Sn, Al, Ga and In). We use the density functional theory implemented by the linearized augmented plane wave method to perform structural optimization and electronic structure calculations. As a main result, from the analysis of the total energies of different systems, we find that the compounds with Z is Si, Ge, Al and Ga are structurally, mechanically and thermodynamically more stable in the inverse Heusler structure (XA structure). The electronic structure investigation shows that Mn_2LiSi, Mn_2LiGe and Mn_2LiSn are half-metallic ferrimagnetic with wide energy gaps and smaller total magnetic moments. We obtain a spin gapless semiconductor and nearly spin semimetallic properties with zero total spin moments in the Mn_2LiAl and Mn_2LiGa, respectively. The exchange interactions are determined within the Korringa-Kohn-Rostoker Green's function framework. We show that the calculated inter-sublattice exchange interaction presents a dominant contribution to the exchange. Having determined the exchange interactions, we can deduce the Curie temperature in the mean-field approximation. Due to the large values of the inter-sublattice exchange reactions, we find that the Curie temperature is much higher than room temperature for all compounds, a prerequisite in spintronics. In the present study, we also calculated and discussed the electronic transport properties based on the semi-classical Boltzmann transport theory.

ملخص

يهدف هذا العمل من خلال المبادئ الأولى إلى دراسة الثبات الهيكلي والخواص الإلكترونية والمغناطيسية والكهروحرارية لمركبات هوسلر الكاملة الافتراضية الجديدة (Mn_2LiZ (Si, Ge, Sn, Al, Ga and In. نستخدم نظرية الكثافة الوظيفية المنفذة بواسطة طريقة الموجة المستوية المعززة الخطية لإجراء التحسين الهيكلي وحساب البنية الإلكترونية. كنتيجة رئيسية، انطلاقا من تحليل نتائج الطاقات الكلية للأنظمة المختلفة، نجد أن المركبات مع Z هي Si و Ge و Al و Ga هي أكثر استقرارًا من الناحية الهيكلية والميكانيكية والديناميكية الحرارية في هيكل هوسلر المعكوس (هيكل XA). تبين دراسة البنية الإلكترونية أن Mn_2LiSi و Mn_2LiGe و Mn_2LiSn هم عبارة عن مغانط فيرية نصف معدنية مع فجوات طاقة واسعة وعزوم مغناطيسية اجمالية أصغر. نحصل على خصائص سبين أشباه الموصلات عديمة الفجوة وما يقرب من سبين اشباه معادن مع صفر عزوم مغناطيسية اجمالية في المركبات Mn_2LiAl و Mn_2LiGa، على التوالي. يتم تحديد تفاعلات التبادل ضمن إطار وظيفة غرين بطريقة كورينجا كوهن روستوكر. نظهر أن تفاعل التبادل المحسوب ما بين الشبكات الفرعية يساهم بشكل كبير في التبادل. بعد تحديد تفاعلات التبادل، يمكننا استنتاج درجة حرارة كوري بالاستعانة بتقريب متوسط الحقول. نظرًا للقيم الكبيرة لتفاعلات التبادل ما بين الشبكات الفرعية، نجد أن درجة حرارة كوري تكون أعلى بكثير من درجة حرارة الغرفة لجميع المركبات، وهو شرط أساسي للسبينترونيات. في هذه الدراسة، قمنا أيضًا بحساب ومناقشة خصائص النقل الإلكتروني بناءً على نظرية النقل لبولتزمان الشبه الكلاسيكية.

Contents

Acknowledgements i

Abstract ii

Introduction 1

I Theoretical Background 5

1 Methods for the Ground-State 6

1.1 Born-Oppenheimer approximation 6

1.2 Hartree-Fock approximation 8

1.3 Density functional theory 10

1.3.1 Hohenberg-Kohn theorems 11

1.3.2 Kohn-Sham approach 14

1.4 Spin-polarized system 17

1.5 Exchange-correlation functional 19

1.5.1 Local (spin) density approximation 19

1.5.2 Generalized gradient approximation 20

1.6 Periodic system 20

1.7 Electronic structure methods 21

1.7.1 The linearized augmented plane wave 22

1.7.2 The Korringa-Kohn-Rostoker Green's function 27

2 Methods at Finite-Temperature 40

2.1 Magnetism 40

2.1.1 Origins 40

2.1.2 Localized and itinerant picture 42

2.1.3 Mean-field approximation 44

2.1.4 Exchange interaction from first-principles . . . 48
2.2 Thermoelectric . . . 49
2.2.1 Semiclassical electrons dynamic . . . 49
2.2.2 Boltzmann transport theory . . . 50
2.2.3 Two-current model . . . 53

II Fundamentals of Heusler Compounds 54

3 Heusler Compounds 55
3.1 Introduction . . . 55
3.2 Structural properties . . . 55
3.3 Electronic structure and magnetic properties . . . 57
3.3.1 Half-metallic ferromagnet . . . 57
3.3.2 Half-metallic ferrimagnet/antiferromagnet . . . 61
3.3.3 Spin-gapless semiconductor . . . 63
3.4 Formation and interaction of the magnetic moments . . . 64

III Results and Discussions 66

4 Prediction of High T_C Half-Metallic Ferrimagnetism 67
4.1 Introduction . . . 67
4.2 Structural, mechanical and thermodynamic stability . . . 68
4.3 Electronic structure and magnetic moments . . . 73
4.4 Exchange interactions and Curie temperature . . . 78
4.5 Thermoelectric transport . . . 80

5 Spin Gapless Semiconductor and Nearly Spin Semimetal Antiferromagnets 82
5.1 Introduction . . . 82
5.2 Structural, mechanical and thermodynamic stability . . . 83
5.3 Electronic structure and magnetic moments . . . 87
5.4 Exchange interactions and Curie temperature . . . 92
5.5 Thermoelectric transport . . . 94

6 Summary and Conclusion 96

Bibliography 98

Introduction

For decades, the field of electronics has continued to advance at a faster pace, thanks to the so-called Moore's Law. The latter says that the density of transistors on the electronic chip doubles about every two years. This allows electronic devices to get smaller and smaller and move closer to the nanoworld. But with these nanoscales being reached nowadays, Moore's Law would break down and thus conventional-electronic technology would slow down or even stop progressing. The reason behind this expected decline is that electronic miniaturization cannot continue indefinitely. In addition, the physical concepts through which conventional transistors are constructed are somewhat incompatible with those related to the nanoscale regime.

While electronics approaches its limits due to physical problems of miniaturization at the nanoscale, spintronics is emerging as one of the most promising areas of science and technology. Spin-electronics focuses on the spin as an additional degree of freedom for the electron and makes use of the nanostructure development—thanks to a constant desire for miniaturization—to explore functional materials and develop fast electronic devices. An example of one of the spintronics devices of great interest is the magnetic tunnel junction (MTJ), which consists of two ferromagnetic layers separated by a thin (about one nanometer) insulator such as a MgO compound that acts as a barrier. This structure is a building block for what is called magnetic random access memory (MRAM), as seen in Figure 1. Electrons can tunnel through the barrier very differently depending on the spin orientations of the electrodes. For the parallel orientation, the resistance of the MTJ device is much less than that of the antiparallel one. This relative change in resistance is called the tunnel magnetoresistance(TMR) effect and defines two states, "1"("0"), for high (low) resistance, currently exploited in MRAM to store information.

However, the performance of such spin-based devices depends on some factors. The main one is the need for a highly spin-polarized current in magnetic electrodes. This is a crucial for increasing the TMR ratio in MTJ devices, according to the Jullieres model [1]

$$TMR = \frac{2P_1P_2}{1 - P_1P_2},$$

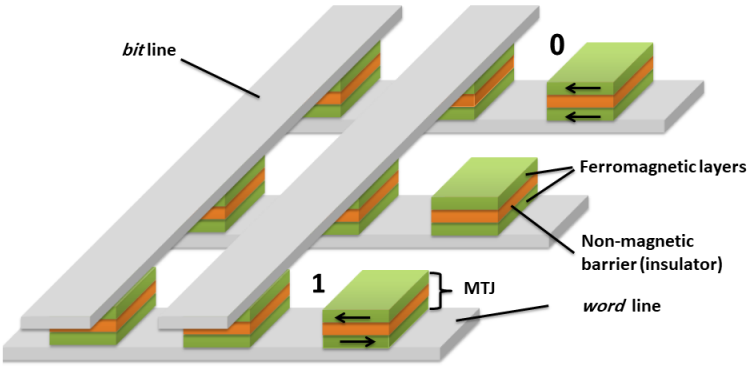

Figure 1: Schematic illustration of the MRAM product in which the MTJ forms a basic element. Arrows indicate the direction of magnetization of the ferromagnetic layers (electrodes), where the binary state is indicated by the relative orientation of the magnetization of the two layers. The so-called *bit* line and word *line* are used for write and read information.

where P_1 and P_2 are the spin-polarization of electrodes. A promising strategy for producing high spin polarization is to use half-metallic ferromagnets (HMFs), which are metals for one spin direction, and semiconductors for the opposite, thus achieving 100% spin polarization at the Fermi level. Under ideal conditions, an infinitely larger effect of TMR can be expected by using HMFs as electrode materials in MTJ structures. For semiconductor spintronics, a high spin-polarized current can be injected into the semiconductor if the HMFs are successfully deposited on top of this semiconductore compound. The first prediction of the half-metallic ferromagnetism in the half-Heusler NiMnSb has triggered enormous research interest in the family of Heusler alloys. These compounds are attractive for practical applications, thanks to their high Curie temperature, a prerequisite for spintronics applications. Moreover, they have cubic crystal structures closely related to that of the existent semiconductor technology, allowing a lattice-constant matching with major substrates. Experimental and theoretical studies show that the physical properties of a large class of Heusler compounds can be tuned by chemical substitution. This flexibility leads to the chemical composition engineering of desired properties, for example tailoring the Fermi level to produce n- or p-type thermoelectric materials. It was found that several Heusler alloys are potential candidates for converting heat into electricity. Heusler compounds are also considered the hot candidates in the exciting new field of spin caloritronics, where spin, charge and heat are coupled to produce new spin-dependent phenomena. The analog of the TMR effect in this field is the tunnel magneto-Seebeck (TMS) effect, in which the temperature gradient is the source power instead of the electrical force.

Heusler compounds are also of great interest for their fundamental aspect in magnetism. Their large family allows for obtaining various magnetic structures. One can

observe ferro-, ferri-, antiferro-magnetism and even non-collinear magnetism between them. The half-metallicity was found to impose certain restrictions on spin fluctuations in Heusler compounds. This unusual behavior is attributed to the electronic hybridization responsible for the formation of the minority gap, which has not been observed in conventional ferromagnets such as Fe, Co and Ni [2].

Nowadays, increasing computational power is prompting material science researchers to design new materials with outstanding properties. In this respect, the vast family of Heusler compounds gives a great possibility and flexibility to conceive potential candidates for spintronics using first-principles calculations, for example, searching compounds with high spin-polarization. Although Heusler compounds are widely studied, particularly for the half-metallic ferromagnetism, they still offer many possibilities for discovering new innovative materials. As such, this work aims to search for desired magnetic properties, such as finding the half-metallicity with a low total magnetic moment and high Curie temperature in new hypothetical stable Heusler compounds. In the framework of density functional theory, and based on some simple design, we consider Li-based full-Heusler compounds for predicting new spintronics materials. One can realize full-Heusler compounds by filling the voids contained in the half-Heusler structure with a small and electropositive alkali-metal element, *i.e.*, Lithium. This design scheme has recently been adopted in the search for a new family of semiconducting Quaternary Heusler compounds based on the 18-electron rule. These materials are suitable for photovoltaic and thermoelectric applications [3].

The Thesis contains five chapters, organized as follows: After this Introduction, Part I introduces physical concepts along with theoretical methods. Part II revolves around the fundamental aspects that characterize the family of magnetic Heusler compounds. While Part III presents and discusses the obtained results.Part I consists of two chapters. In Chapter 1, theoretical methods and approaches are presented to describe the ground-state properties. Here, the central theme is the density functional theory which is the basis of almost all modern electronic structure calculations. First, We introduce the Born-Oppenheimer and Hartree-Fock approaches for giving an elementary presentation of some fundamental concepts, such as the exchange energy, and emphasizing the need for a simpler and more reliable method. This makes it possible to gradually introduce density functional theory, as well as its extension to treat magnetic systems. Afterward, the practical aspect of density functional theory is discussed, and its implementation for periodic solids is explained, including two electronic structure methods: The linearized augmented plane wave (LAPW) and the Korringa-Kohn-Rostoker Green's function (KKR-GF). Chapter 2 is devoted to a brief description of magnetism and thermoelectric transport at a finite temperature, focusing on schemes that allow parameters to be determined from

the first principles. Part II contains Chapter 3. It discusses the structural, electronic and magnetic properties of magnetic Heusler compounds. Part III examines the physical properties of new Heusler compounds. It deals with the structural, electronic, magnetic and electron transport properties for Mn_2LiZ with (Z= Si, Ge and Sn) in Chapter 4 and with (Z = Al, Ga and In) in Chapter 5.

Part I

Theoretical Background

Chapter 1

Methods for the Ground-State

In this chapter, some basic methods for dealing with the ground-state properties of solid systems are presented. The ground state corresponds to the lowest total energy of the system, which can be determined using the variational principle of quantum mechanics. The methods adopted for these schemes are called first-principles or *ab-initio* methods. *Ab-initio* approaches mean that only fundamental physical constants are used as inputs in performing the calculations, and there is no adjustable experimental parameters are needed. Therefore, one begins the study from the basic principle, *i.e.*, the fundamental Hamiltonian of a set of interacting electrons and nuclei is considered a starting point for any first-principles study. Since solving the corresponding Schrodinger equation is difficult, it is possible to simplify it by following some basic approximations.

1.1 Born-Oppenheimer approximation

Understanding the different behaviors and predicting the physical properties of real materials requires sophisticated methods for solving the Schrodinger equation of the solid [4]. However, the solid is made up of a set of N electrons and M nuclei, and all these particles interact with each other by the coulomb forces. It follows that it is difficult to deal with this $N + M$ corps problem exactly. Any practical scheme needs some basic physical approximations. One of them is the Born-Oppenheimer approximation. It assumes that the motion of the electrons can be separated from that of the nuclei due to the large mass difference between electrons and protons (component of the nucleus) [5]. The starting point is the Schrodinger equation of the solid

$$(\hat{H} - E)\Psi(\mathbf{r}_1, \ldots, \mathbf{r}_N; \mathbf{R}_1, \ldots, \mathbf{R}_N) = 0. \tag{1.1}$$

The wave function Ψ is a function of $N+M$ variables, where the vectors $\mathbf{r}_i$ and $\mathbf{R}_l$ denote the Cartesian coordinates of electrons and nuclei, respectively. Using Hartree atomic units, the full Hamiltonian H is given by

$$\begin{aligned}\hat{H} = &\sum_{i=1}^{N} -\frac{1}{2}\nabla_i^2 + \sum_{l=1}^{M} -\frac{1}{2}\nabla_l^2 \\ &+ \sum_{i=1}^{N}\sum_{l=1}^{M} \frac{-Z_l}{|\mathbf{r}_i - \mathbf{R}_l|} + \sum_{i,j=1;i<j}^{N} \frac{1}{|\mathbf{r}_i - \mathbf{r}_j|} + \sum_{l,k=1;l<k}^{M} \frac{Z_l Z_k}{|\mathbf{R}_l - \mathbf{R}_k|},\end{aligned} \tag{1.2}$$

where $\nabla_i = \nabla_{\mathbf{r}_i}$ and $\nabla_l = \nabla_{\mathbf{r}_l}$ are the gradient vectors for the i-th electrons and l-th nuclei, respectively. Z_l is the atomic number of an atom centered at R_l. The first two terms are respectively the kinetic energy of the electrons and the kinetic energy of the nuclei, and the last three terms are the potentials that describe the Coulomb electron-nucleus, electron-electron and nucleus-nucleus interaction, respectively. The motion of electrons is much faster than that of nuclei, and with a good approximation, nuclei can be considered as fixed in their mean positions. The result is that the problem can be reduced to the problem of N electron-corps. The electronic part of the global Hamiltonian, H_e, can be separately considered from the nuclear one with the corresponding Schrodinger equation

$$[\hat{H}_e - E_e(\mathbf{R})]\Phi(\mathbf{r}_1, \ldots, \mathbf{r}_N; \mathbf{R}_1, \ldots, \mathbf{R}_N) = 0, \tag{1.3}$$

$$\hat{H}_e = \sum_{i=1}^{N} -\frac{1}{2}\nabla_i^2 + \sum_{i=1}^{N}\sum_{l=1}^{M} \frac{-Z_l}{|\mathbf{r}_i - \mathbf{R}_l|} + \sum_{i,j=1;i<j}^{N} \frac{1}{|\mathbf{r}_i - \mathbf{r}_j|}. \tag{1.4}$$

Although the problem is reduced to one that relates only to the degree of freedom of the electrons, it still presents difficulties. The presence of the last term (e-e interaction) in the electronic-Hamiltonian implies that the correspondent Schrodinger equation is difficult to deal with exactly. The system to be solved is an interacting-electrons system. Its wave function cannot be factorized into a product of single-particle wave functions. Therefore, further approximation is needed for handling the electronic problem. The Hartree-Fock approach approximates the many-body wave function as a single Slater-determinant that allows mathematically to represent the complex system of interacting electrons into an effective system of non-interacting particles [6].

1.2 Hartree-Fock approximation

The Hartree-Fock approximation is based on the variational principle of quantum mechanics. The total energy of the system is written as

$$E_e = \langle \Phi | \hat{H}_e | \Phi \rangle. \tag{1.5}$$

If the wave function is not a true eigenstate of the Hamiltonian but appropriately chosen to match the physical system, the variational principle can be successfully applied. It states that any trial total energy is an upper bound to the exact ground-state one. At this point, The Hartree-Fock approximation can be applied. Initially, the Hartree approach has been used, which can be understood as a scheme based on the variational principle with the following trial wave function

$$\Phi(\mathbf{r}_1, \ldots, \mathbf{r}_N) = \prod_{i=1}^{N} \varphi(\mathbf{r}_i), \tag{1.6}$$

as the inner product of the single-particle wave functions $\varphi(\mathbf{r}_i)$ of electrons [7]. Since electrons are Fermion particles, they are indistinguishable entities, and their wave function must be antisymmetric to the particle permutation operations. The Hartree-Fock approach takes this fact into account by using the trial wave function as a determinant of the single-particle wave functions, called Slater determinant [8]

$$\Phi(\mathbf{x}_1, \ldots, \mathbf{x}_N) = \frac{1}{\sqrt{N!}} \det \varphi(\mathbf{x}_1, \ldots, \mathbf{x}_N), \tag{1.7}$$

with $\mathbf{x} = \mathbf{r}\sigma$, where $\sigma = \{\uparrow, \downarrow\}$ is the spin variable. $\varphi(\mathbf{x}_1, \ldots, \mathbf{x})$ represents a matrix with single-particle spin-wave function elements

$$\varphi(\mathbf{x}_1, \ldots, \mathbf{x}_N) = \begin{pmatrix} \varphi_1(\mathbf{x}_1) & \varphi_1(\mathbf{x}_2) & \ldots & \varphi_1(\mathbf{x}_N) \\ \varphi_2(\mathbf{x}_1) & \varphi_2(\mathbf{x}_2) & \ldots & \varphi_2(\mathbf{x}_N) \\ \ldots & \ldots & \ldots & \ldots \\ \varphi_N(\mathbf{x}_1) & \varphi_N(\mathbf{x}_2) & \ldots & \varphi_N(\mathbf{x}_N \end{pmatrix}. \tag{1.8}$$

The function $\varphi_\lambda(\mathbf{x}) = \varphi_i(\mathbf{r})\eta_{s_i}(\sigma)$ is the spin orbital with $\lambda = is_i$, where s_i is the spin of the electron occupying orbital i. Assuming spatial orbitals $\varphi_i(\mathbf{r})$, are orthonormal

$$\int \varphi_i^*(\mathbf{r})\varphi_j(\mathbf{r})d\mathbf{r} = \delta_{ij}, \tag{1.9}$$

as well as spin functions $\eta_{s_i}(\sigma)$ is also orthonormal

$$\sum_{\sigma} \eta_{s_i}^*(\sigma)\eta_{s_j}(\sigma) = \delta_{s_i s_j}, \tag{1.10}$$

the explicit expression of the total energy is

$$E = \sum_{i=1}^{N} \int \varphi_i^*(\mathbf{r}) h(\mathbf{r}) \varphi_i(\mathbf{r}) d\mathbf{r} \tag{1.11}$$
$$+ \frac{1}{2} \sum_{i,j=1}^{N} \iint \varphi_i^*(\mathbf{r}) \varphi_j^*(\mathbf{r}') v(\mathbf{r}-\mathbf{r}') \varphi_i(\mathbf{r}) \varphi_j(\mathbf{r}') d\mathbf{r} d\mathbf{r}'$$
$$- \frac{1}{2} \sum_{i,j=1}^{N} \iint \varphi_i^*(\mathbf{r}) \varphi_j^*(\mathbf{r}') v(\mathbf{r}-\mathbf{r}') \varphi_j(\mathbf{r}) \varphi_i(\mathbf{r}') d\mathbf{r} d\mathbf{r}' \delta_{s_i s_j},$$

with

$$h(\mathbf{r}) = -\frac{1}{2}\nabla^2 + \sum_{l=1}^{M} \frac{-Z_l}{|\mathbf{r}-\mathbf{R}_l|}, \tag{1.12}$$

$$v(\mathbf{r}-\mathbf{r}') = \frac{1}{|\mathbf{r}-\mathbf{r}'|}. \tag{1.13}$$

In Equation (1.11), the second term is the Hartree energy, E_H, and the last term is the exchange energy, E_x which equals to zero except for parallel spins, resulting from quantum nature of the exchange—permutation of identical particles—between electrons. In Equation (1.11), the factor $1/2$ is introduced in order to eliminate the double counting existing in both E_H and E_x. In Hartree's expression of energy, terms associated with orbitals such as $s_i = s_j$ are not physical, and they are correctly canceled by that contained in the exchange energy. This non physical contribution is known as the self-interaction energy and is always present in the Hartree approach if the formulation is given by electron density instead of single-particle wave functions. Using the variational principle, Equation (1.11) can be minimized with respect to single-particle states under the constraint of the above normalization. This leads to what are called the Hartree-Fock equations

$$h(\mathbf{r})\varphi_i(\mathbf{r}) + \sum_j \int d\mathbf{r}' |\varphi_j(\mathbf{r}')|^2 v(\mathbf{r}-\mathbf{r}') \varphi_i(\mathbf{r}) \tag{1.14}$$
$$- \sum_j \int d\mathbf{r}' \delta_{s_i s_j} \frac{\varphi_j^*(\mathbf{r}') v(\mathbf{r}-\mathbf{r}') \varphi_i(\mathbf{r}') \varphi_j(\mathbf{r})}{\varphi_i(\mathbf{r})} \varphi_i(\mathbf{r})$$
$$= \epsilon_i \varphi_i(\mathbf{r}).$$

The second term in the left-hand side of Equation (1.14) is the Hartree potential. The third term is the exchange potential which is a nonlocal term. The Hartree-Fock equations are nonlocal single-particle Schrodinger-like equations. However, these equations are non linear—the potential itself incorporates the single-particle states—which can only be solved self-consistently.

1.3 Density functional theory

It is interesting to reduce all the complexity of the many-body Schrodinger equation to the one single-particle Schrodinger equation, as is the case with the Hartree-Fock approximation. However, for solids, the latter approximation has the disadvantage of insufficient accuracy which leave the HF equations rarely used for real materials. The inaccuracy comes from the way of approximating the many-body state, the Slater determinant in the HF treatment completely excludes the correlation between electrons. Therefore, a new scheme that goes beyond the HF approximation is needed. Within density functional theory (DFT), the global system of interacting electrons can be mapped onto an effective non-interacting-system, incorporating the many-body effects in a unique way. The basic idea is that instead of the many-body wave function represented by $3N$ variables, one can be interested in describing the complex system using the electron density $n(\mathbf{r})$, which contains only three variable. The electron density is given by

$$\begin{aligned} n(\mathbf{r}) &= \langle\Phi|\sum_i \delta(\mathbf{r}-\mathbf{r}_i)|\Phi\rangle \\ &= N\int\ldots\int|\Phi(\mathbf{r},\mathbf{r}_2,\ldots,\mathbf{r}_N)|^2 d\mathbf{r}_2\ldots d\mathbf{r}_N. \end{aligned} \tag{1.15}$$

The second part of the electronic-Hamiltonian, Equation (1.4), can be expressed

$$\begin{aligned} \sum_{i=1}^{N}\sum_{l=1}^{M}\frac{-Z_l}{|\mathbf{r}_i-\mathbf{R}_l|} &= \hat{V} \\ &= \sum_{i=1}^{N} v_{ext}(\mathbf{r}_i) \\ &= \sum_{i=1}^{N}\int v_{ext}(\mathbf{r})\delta(\mathbf{r}-\mathbf{r}_i), \end{aligned} \tag{1.16}$$

with $v_{ext}(\mathbf{r}) = \sum_{l=1}^{M}\frac{-Z_l}{|\mathbf{r}-\mathbf{R}_l|}$, is termed the external potential. Thus the expectation value of the operator $\hat{V}$ can be written in terms of the electron density

$$\begin{aligned} \langle\Phi|\hat{V}|\Phi\rangle &= \int v_{ext}(\mathbf{r})\langle\Phi|\sum_{i=1}^{N}\delta(\mathbf{r}-\mathbf{r}_i)|\Phi\rangle d\mathbf{r} \\ &= \int v_{ext}(\mathbf{r})n(\mathbf{r})d\mathbf{r}. \end{aligned} \tag{1.17}$$

One of the main statements of the DFT presenting in the Hohenberg-Kohn theorems is that any ground-state observable is uniquely determined by the electron density [9]. This is a consequence of one-to-one correspondence between the external potential and the electronic density.

1.3.1 Hohenberg-Kohn theorems

DFT is based on two theorems established by Hohenberg and Kohn (HK) in 1964. The first theorem emphasizes the importance of electron density in describing an interacting system via a functional of the density. And the second shows that the energy functional admits in terms of the electron density the variational principle. To see that, we first present the electronic-Hamiltonian, Equation(1.4), in second quantization form using the creation and annihilation field operators $\hat{\psi}^\dagger(\mathbf{r})$ and $\hat{\psi}(\mathbf{r})$, respectively

$$\hat{H}_e = \hat{T} + \hat{W} + \hat{V} \tag{1.18}$$

in which

$$\hat{T} = -\frac{1}{2}\int \hat{\psi}^\dagger(\mathbf{r})\nabla^2\hat{\psi}(\mathbf{r})d\mathbf{r} \tag{1.19}$$

$$\hat{W} = \frac{1}{2}\iint \hat{\psi}^\dagger(\mathbf{r})\hat{\psi}^\dagger(\mathbf{r}')\frac{1}{|\mathbf{r}-\mathbf{r}'|}\hat{\psi}(\mathbf{r}')\hat{\psi}(\mathbf{r})d\mathbf{r}d\mathbf{r}' \tag{1.20}$$

$$\hat{V} = \int v_{ext}(\mathbf{r})\hat{\psi}^\dagger(\mathbf{r})\hat{\psi}(\mathbf{r})d\mathbf{r}. \tag{1.21}$$

It is clear that the Hamiltonian in this form reveals that the interacting system is completely specified by the third term, V, precisely by v_{ext} and the constraint $\int n(\mathbf{r})d\mathbf{r} = N$. In other words, different interacting system is characterized by a different external potential. Therefore, for a given v_{ext}, one can solve the correspondent Schrodinger equation and obtain the ground state $|\Psi\rangle$, and hence the corresponding electron density

$$n(\mathbf{r}) = \langle\Psi|\hat{\psi}^\dagger(\mathbf{r})\hat{\psi}(\mathbf{r})|\Psi\rangle. \tag{1.22}$$

With a non-degenerate ground state, it follows that the electron density is uniquely determined by the external potential. In this case n is a functional of v_{ext}

$$v_{ext} \Longrightarrow |\Psi\rangle \Longrightarrow n. \tag{1.23}$$

The interesting fact is that the reverse path is also possible, *i.e.*, the ground-state electron density determines uniquely the external potential

$$n \Longrightarrow v_{ext}. \tag{1.24}$$

Mathematically

$$v_{ext}[n](\mathbf{r}). \tag{1.25}$$

The external potential is a unique functional of the ground-state density. This result is not self-evident and therefore requires proof. The proof was given by Hohenberg and Kohn using the *reductio ad absurdum* procedure [9]. Suppose there is another system characterized by the Hamiltonian H' and hence the external potential v'_{ext} which differ by more than a constant to v_{ext}. This system has the ground state $|\Psi'\rangle$ and the ground-state energy E'. Assume the two systems with Hamiltonian H and H' have the same ground-state density $n(\mathbf{r})$, one can write

$$\begin{aligned} E &= \langle\Psi|H|\Psi\rangle \\ &= \langle\Psi|H - H'|\Psi\rangle + \langle\Psi|H'|\Psi\rangle \\ &= \int \left[v_{ext}(\mathbf{r}) - v'_{ext}(\mathbf{r})\right] n(\mathbf{r}) d\mathbf{r} + \langle\Psi|H'|\Psi\rangle. \end{aligned} \tag{1.26}$$

Using the variational principle for the wave function one can obtain

$$E' = \langle\Psi'|H'|\Psi'\rangle < \langle\Psi|H'|\Psi\rangle. \tag{1.27}$$

The combination of Equation (1.26) with Equation (1.27) gives

$$E - E' < \int \left[v_{ext}(\mathbf{r}) - v'_{ext}(\mathbf{r})\right] n(\mathbf{r}) d\mathbf{r}. \tag{1.28}$$

Equivalently, the above quantities with primed and unprimed notation can be exchanged to yields

$$E' - E < \int \left[v_{ext}(\mathbf{r}) - v'_{ext}(\mathbf{r})\right] n(\mathbf{r}) d\mathbf{r}. \tag{1.29}$$

Therefore, one can immediately see that addition of Equation (1.28) with Equation (1.29) leads to a contradiction

$$0 < 0. \tag{1.30}$$

Hence v_{ext} is uniquely determined by n.

The first theorem can be stated: *For any system of interacting electrons subject to external potential, the ground-state electron density and this external potential determine each other.* Mathematically, the external potential can be expressed as a functional of the ground-state electron density. Since different systems are only distinguished by external potential, it turns out that v_{ext} fixes H, which implies that the corresponding ground state is a unique functional of the ground-state electron density.

The fact that the ground state $|\Psi\rangle$ is a functional of the density $|\Psi[n]\rangle$ implies that any observable, such as the energy E is a functional of the density

$$E[n] = \left\langle \Psi[n] \left| \hat{H} \right| \Psi[n] \right\rangle. \tag{1.31}$$

By this statement a universal functional $F[n]$ is naturally defined

$$E[n] = F[n] + \int v_{ext}(\mathbf{r}) n(\mathbf{r}) d\mathbf{r}, \tag{1.32}$$

where

$$F[n] = \left\langle \Psi[n] \left| \hat{T} + \hat{W} \right| \Psi[n] \right\rangle. \tag{1.33}$$

This functional is the same for all different systems in which the electrons interact with each other via the Coulomb interaction, it is universal. Let us turn to another more important property. From the previous statement one can write

$$E[n] = \left\langle \Psi[n] \left| \hat{H} \right| \Psi[n] \right\rangle < \left\langle \Psi'[n'] \left| \hat{H} \right| \Psi'[n'] \right\rangle, \tag{1.34}$$

$$\Rightarrow E[n] < E[n']. \tag{1.35}$$

This indicates that the ground-state energy can be expressed as a functional of the ground-state density n' corresponding to any external potential v'_{ext} other than v_{ext} in which $v'_{ext} \neq v_{ext}$+constant. So that, using the variational principle one can determine the correct ground-state density n from the minimum of the ground-state energies.

$$E[n] = \min E[n']. \tag{1.36}$$

Therefore, the exact ground-state electron density minimizes the energy functional which would allow all ground state properties to be determined. This bring us to the second theorem: *For any system of interacting electrons, the functional $E[n']$ with n' are trial densities can exist, and the lower bound of this functional represents the ground-state total energy $E[n]$ with n is the ground-state density.*

Hence, if the expression of the total-energy functional of the interacting-system is known, one can minimized it over admissible trial densities to determine the correct ground-state electron density using the following variational principle

$$\frac{\delta}{\delta n'(\mathbf{r})} \left\{ E[n'] - \mu \left(\int n'(\mathbf{r}) d\mathbf{r} - N \right) \right\} \Bigg|_{n'(\mathbf{r})=n(\mathbf{r})} = 0, \tag{1.37}$$

where μ is the Lagrange multiplier introduced to insure that the system contains the correct N number of electrons, so μ it is exactly the chemical potential.

The HK theorems can readily be generalized to describe systems with degenerate ground states [10].

1.3.2 Kohn-Sham approach

Evidently, the HK theory gives the possibility to treat any interacting electronic system in terms of the electron density. This theory proves that all ground-state properties can be determined if the ground-states electron density is determined. Very importantly, the second HK theorem states that the exact ground-state electron density $n(\mathbf{r})$ can be obtained by minimizing the energy functional $E[n']$. Unfortunately, the expression of one part of this energy functional, the universal functional, $F[n']$, is not explicitly known. Therefore, for practical purposes, any scheme needs to approximate this functional.

Kohn and Sham gives an elegant way to map the interacting-system onto effective non-interacting one [11]. The ansatz that Kohn and Sham worked on was to find an auxiliary non-interacting system with an effective potential $v_s(\mathbf{r})$ in a such way that the ground-state electron density of this system $n_s(\mathbf{r})$ is the same with the true one, that is

$$n_s(\mathbf{r}) = n(\mathbf{r}). \tag{1.38}$$

Therefore, an inhomogeneous system of independent particles can be simply solved using the single-particle Schrodinger equations

$$\left(-\frac{1}{2}\nabla^2 + v_s(\mathbf{r})\right)\varphi_i(\mathbf{r}) = \epsilon_i\varphi_i(\mathbf{r}), \tag{1.39}$$

where the corresponding electron density can be expressed in terms of $\varphi_i(\mathbf{r})$ KS states as

$$n_s(\mathbf{r}) = \sum_{i=1}^{N} |\varphi_i(\mathbf{r})|^2, \tag{1.40}$$

in which the sum is restricted to occupied states. In this way, the energy functional of the non-interacting system is given

$$E_s[n] = T_s[n] + \int v_s(\mathbf{r})n(\mathbf{r})d\mathbf{r}, \tag{1.41}$$

where $T_s[n]$ is the kinetic energy of system of independent particles which can be expressed in terms of the KS states

$$\begin{aligned} T_s[n] &= \left\langle \Phi_s[n] \left| \hat{T} \right| \Phi_s[n] \right\rangle \\ &= -\frac{1}{2}\sum_{i=1}^{N} \int \varphi_i^*(\mathbf{r})\nabla^2\varphi_i(\mathbf{r})d\mathbf{r}. \end{aligned} \tag{1.42}$$

The state $|\Phi_s[n]\rangle$ is the Slater determinant of the auxiliary KS system. At this stage, the

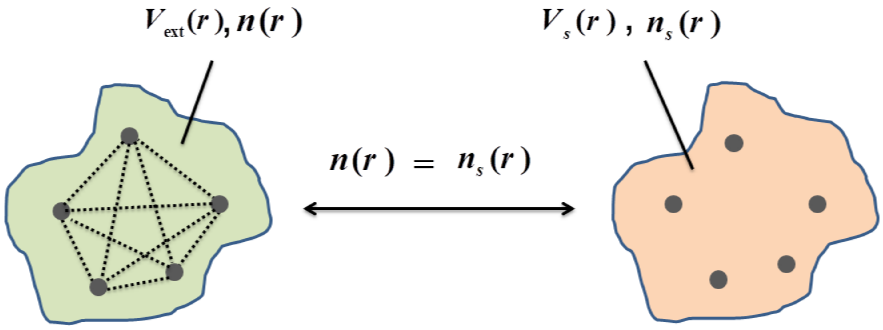

Figure 1.1: Correspondence between the interacting system (in the left) and the effective non-interacting system (in the right), with the constraint that the two systems have the same electron density

problem is reduced to how the KS potential $v_s(\mathbf{r})$ is determined. The expression of the universal functional can be decomposed into known and unknown parts

$$F[n] = T_s[n] + W_H[n] + E_{xc}[n], \tag{1.43}$$

and hence the ground-state total energy is given

$$E[n] = T_s[n] + W_H[n] + E_{xc}[n] + \int v_s(\mathbf{r})n(\mathbf{r})d\mathbf{r}. \tag{1.44}$$

The explicit expression of the first term in Equation (1.44) is given above and the second term is the Hartree energy which is the major part of the Coulomb repulsion, reads

$$W_H[n] = \frac{1}{2}\iint \frac{n(\mathbf{r})n(\mathbf{r}')}{|\mathbf{r}-\mathbf{r}'|}d\mathbf{r}d\mathbf{r}', \tag{1.45}$$

and the third term is called the exchange-correlation energy defined as

$$E_{xc}[n] = T[n] - T_s[n] + W[n] - E_H[n]. \tag{1.46}$$

This functional contains all the many-body effects, and is the unknown part which has to be approximated. From the second theorem of Hohenberg and Kohn one can use the variational principle Equation (1.37) for energy functional of the interacting system

$$\begin{aligned}\left.\frac{\delta E[n']}{\delta n'(\mathbf{r})}\right|_{n'=n} &= \left.\frac{\delta T_s[n']}{\delta n'(\mathbf{r})}\right|_{n'=n} + v_{ext}(\mathbf{r}) \\ &+ \int \frac{n(\mathbf{r})}{|\mathbf{r}-\mathbf{r}'|}d\mathbf{r}' + \left.\frac{\delta E_{xc}[n']}{\delta n'(\mathbf{r})}\right|_{n'=n} \\ &= \mu.\end{aligned} \tag{1.47}$$

Equally, one can do the same for the effective non-interacting system

$$\begin{aligned} \left.\frac{\delta E_s[n']}{\delta n'(\mathbf{r})}\right|_{n'=n} &= \left.\frac{\delta T_s[n']}{\delta n'(\mathbf{r})}\right|_{n'=n} + v_s(\mathbf{r}) \\ &= \mu. \end{aligned} \tag{1.48}$$

Combining Equation (1.47) with Equation (1.48) one can deduce the expression of the effective potential

$$v_s(\mathbf{r}) = v_{ext}(\mathbf{r}) + v_H(\mathbf{r}) + v_{xc}(\mathbf{r}), \tag{1.49}$$

where the second term is the Hartree potential

$$v_H(\mathbf{r}) = \int \frac{n(\mathbf{r}')}{|\mathbf{r} - \mathbf{r}'|} d\mathbf{r}', \tag{1.50}$$

and $v_{xc}(\mathbf{r}) = \left.\frac{\delta E_{xc}[n']}{\delta n'(\mathbf{r})}\right|_{n'=n}$ is termed as the exchange-correlation potential.

Now, the famous single-particle Schrodinger-like equation called the KS equation is given

$$\left\{ -\frac{1}{2}\nabla + v_{ext}(\mathbf{r}) + v_H[n](\mathbf{r}) + v_{xc}[n](\mathbf{r}) \right\} \varphi_i(\mathbf{r}) = \epsilon_i \varphi_i(\mathbf{r}). \tag{1.51}$$

Note that the effective potential depends on the electron density, and the density itself depends on the single-particle KS orbitals. So that the KS equations must be solved self-consistently similar to the HF equations. The way to find solutions is as follows: the starting point is the assumption of a suitable initial trial-density n^1 that allows to construct a trial KS potential without the use of KS orbitals. Then the KS equations are solved and from the solutions a new trial density n^2 is build and from that a new KS potential is constructed. This procedure is continued in iterative manner until this self-consistency is reached. The self-consistent solution is only found when the trial density n^i equal to the correct one, $n^i = n$. This is consistent with the variational principle related to the DFT.

For the ground-state total energy, Equation (1.44), an alternative expression can be derived. From Equation (1.41) one deduce the kinetic energy of KS system

$$\begin{aligned} T_s[n] &= E_s[n] - \int v_s(\mathbf{r}) n(\mathbf{r}) d\mathbf{r} \\ &= \sum_i \epsilon_i - \int v_s(\mathbf{r}) n(\mathbf{r}) d\mathbf{r}, \end{aligned} \tag{1.52}$$

and insert it in Equation (1.44) to obtain

$$E[n] = \sum_i \epsilon_i - W_H[n] - \int v_{xc}(\mathbf{r}) n(\mathbf{r}) d\mathbf{r} + E_{xc}[n]. \tag{1.53}$$

The derivation of an expression for the ground-state energy to this particular form is useful, because in numerical application the evaluation of the gradient of the KS orbitals is avoided. It should be noticed that the KS eigenfunctions and eigenvalues have in general no physical meaning, except that the eigenvalue of the highest occupied state is identical to the negative first ionization energy, as proven by Janaks theorem [11]. The exact KS gap is inevitably smaller than the true gap by some amount Δ_{xc} related to the so-called derivative discontinuity. Nevertheless, they are often used successfully to interpret excitation spectra, especially for systems of weakly correlated electrons [12]. Therefore for weakly correlated solids, it is a good approximation to assumes the KS states as Bloch states and the KS energies as band energies.

1.4 Spin-polarized system

The extension of the DFT to spin-system can somewhat follows the same arguments as for non-polarized case [13, 14]. At the ground-state, it can be shown that the total energy is a unique functional of both the electron density $n(\mathbf{r})$ and the magnetization density $\mathbf{m}(\mathbf{r})$, with

$$\mathbf{m}(\mathbf{r}) = \langle \Psi | \mu_{\mathrm{B}} \sum_{i=1}^{N} \sigma_i \delta(\mathbf{r} - \mathbf{r}_i) | \Psi \rangle, \tag{1.54}$$

where σ denotes the 2×2 Pauli matrices, and μ_{B} is the Bohr magneton. Therefore, the ground-state total energy functional is given by

$$\begin{aligned} E[n, \mathbf{m}] = F[n, \mathbf{m}] &+ \int v_{ext}(\mathbf{r}) n(\mathbf{r}) d\mathbf{r} \\ &- \int \mathbf{B}_{ext}(\mathbf{r}) \mathbf{m}(\mathbf{r}) d\mathbf{r}, \end{aligned} \tag{1.55}$$

and $\mathbf{B}_{ext}(\mathbf{r})$ is the external magnetic field. The universal functional is given

$$F[n, \mathbf{m}] = \left\langle \Psi[n, \mathbf{m}] \left| \hat{T} + \hat{W} \right| \Psi[n, \mathbf{m}] \right\rangle. \tag{1.56}$$

The functional $E[n, \mathbf{m}]$ is a lower bound over all trail densities n' and $\mathbf{m}'$

$$E[n, \mathbf{m}] < E[n', \mathbf{m}']. \tag{1.57}$$

This generalization is necessary for systems subject to static magnetic fields or spontaneously magnetic systems including atoms, molecules, clusters or solids. In many cases, magnetic systems are characterized by collinear spins arrangements, so the functional of the energy can be simplified to be represented by scalar densities instead of $\mathbf{m}(\mathbf{r})$ which is a vector density. The simplified variables are the scalar spin-resolved densities, $n_\uparrow$ and $n_\downarrow$, where the arrows indicates the up- and down-spin, respectively [10]

$$E[n_\uparrow, n_\downarrow] = F[n_\uparrow, n_\downarrow] + \int v_{ext}(\mathbf{r})(n_\uparrow + n_\downarrow)d\mathbf{r} - \mu_\mathrm{B} \int B_{ext}(\mathbf{r})(n_\uparrow - n_\downarrow)d\mathbf{r}, \tag{1.58}$$

where

$$n(\mathbf{r}) = n_\uparrow(\mathbf{r}) + n_\downarrow(\mathbf{r}), \tag{1.59}$$

and

$$m(\mathbf{r}) = \mu_\mathrm{B}\left[n_\uparrow(\mathbf{r}) - n_\downarrow(\mathbf{r})\right]. \tag{1.60}$$

With this simplified version of the spin-DFT the variational principle can be used for each spin channel separately

$$\frac{\delta}{\delta n'_\sigma(\mathbf{r})}\left\{E[n'_\uparrow, n'_\downarrow] - \mu_\sigma\left(\int n'_\sigma(\mathbf{r})d\mathbf{r} - N_\sigma\right)\right\}\Big|_{n'_\sigma(\mathbf{r})=n_\sigma(\mathbf{r})} = 0, \tag{1.61}$$

where $\sigma = \{\uparrow, \downarrow\}$ and μ_σ is the Lagrange parameter that controls the spin-resolved electron numbers $N_\sigma = \int n_\sigma(\mathbf{r})d\mathbf{r}$. This particular representation of the ground-sate energy functional is relevant for systems feature collinear magnetism such as ferro-, antiferro- and ferrri-magnetism. Therefore, using the above variational minimization the spin-dependent KS equations are given

$$\left(-\frac{1}{2}\nabla^2 + v_s^\sigma(\mathbf{r})\right)\varphi_{i\sigma}(\mathbf{r}) = \epsilon_{i\sigma}\varphi_{i\sigma}(\mathbf{r}), \tag{1.62}$$

$$v_s^\sigma(\mathbf{r}) = v_{ext}(\mathbf{r}) + v_H(\mathbf{r}) + \mathrm{sign}(\sigma)\mu_\mathrm{B}B_{ext}(\mathbf{r}) + v_{xc}^\sigma(\mathbf{r}), \tag{1.63}$$

$$v_{xc}^\sigma(\mathbf{r}) = \frac{\delta E[n'_\uparrow, n'_\downarrow]}{\delta n_\sigma(\mathbf{r})}. \tag{1.64}$$

In the absence of the external magnetic field the effective potential is still spin-dependent through the exchange-correlation term. So many systems can exhibit spin polarization which yield internal magnetization.

1.5 Exchange-correlation functional

So far, all attempts we have discussed in the previous sections are an exact formulation of the interacting system. We have seen how the many-body problem is transferred into the self-consistent single-particle Schrodinger-like equations problem, so-called the KS equations. On the other hand, the largest contribution to the total energy representing the classical part is explicitly known. While the rest, the exchange-correlation contribution, which has only a small fraction of the total energy is not known. Therefore, for practical use of the density functional theory via the the KS equations, the exchange-correlation functional must be approximated

1.5.1 Local (spin) density approximation

The simplest and very successful approximation for DFT is the local (spin) density approximation (L(S)DA) [9, 15, 16]. The main motivation behind this approximation is to exploit the properties of the very well-studied system, the homogeneous gas of interacting electrons. For slowly varying electron spin densities, the exchange-correlation functional can be approximated by

$$E_{xc}^{\mathrm{L(S)DA}}[n_\uparrow, n_\downarrow] = \int \epsilon_{xc}(n_\uparrow(\mathbf{r}), n_\downarrow(\mathbf{r}))n(\mathbf{r})\, d\mathbf{r}. \tag{1.65}$$

For non-polarized systems, the description is given by equal spin densities $n_\uparrow = n_\downarrow$. In Equation (1.65), the energy per electron $\epsilon_{xc}(n_\uparrow, n_\downarrow)$ is defined locally as the exchange-correlation energy of uniform electron gas of spin densities $n_\uparrow$ and $n_\downarrow$. Further, this energy function can be divided into two contributions

$$\epsilon_{xc}(n_\uparrow, n_\downarrow) = \epsilon_x(n_\uparrow, n_\downarrow) + \epsilon_c(n_\uparrow, n_\downarrow). \tag{1.66}$$

The first part expresses the exchange energy in a homogenous gas, and this term is known analytically [17]

$$\epsilon_x(n_\uparrow, n_\downarrow) = -3\left(\frac{3}{4\pi}\right)^{\frac{1}{3}} \frac{1}{n}\left(n_\uparrow^{\frac{4}{3}} + n_\downarrow^{\frac{4}{3}}\right). \tag{1.67}$$

The second part, $\epsilon_c(n_\uparrow, n_\downarrow)$, is the correlation energy per electron of the homogeneous electron gas. The general expression of $\epsilon_c(n_\uparrow, n_\downarrow)$ is not known. Nevertheless, explicit expressions can exist in the high- and low-density limit. On the basis of quantum Monte-Carlo simulations, the regime between high and low densities can be interpolated, leading to several parameterizations [13, 18, 19, 20, 21]. For many systems, results calculated

based on the L(S)DA are surprisingly accurate, where L(S)DA performs very well in a sufficiently inhomogeneous system. However, as a simple approximation, the LDA fails in systems with rapidly varying electron density such as atoms or molecules. For example it tends to overestimate the binding energies of molecules.

1.5.2 Generalized gradient approximation

A further step to account for the high inhomogeneity of electron density is the generalization of L(S)DA to include in addition to electron density its gradients. This is called the generalized gradient approximation (GGA). The functional GGA is an improvement over L(S)DA. For spin-polarized system the GGA functional take the general form

$$E_{xc}^{\mathrm{GGA}}[n_\uparrow, n_\downarrow] = \int f(n_\uparrow, n_\downarrow, \nabla n_\uparrow, \nabla n_\downarrow) d\mathbf{r}, \tag{1.68}$$

where f is some function has to be constructed very carefully so that a number of physical conditions are fulfilled. However, the construction is not unique, leading to different forms of GGA-functionals. For solids, the most popular is the PBE functional proposed by Perdew, Burke and Ernzerhof in 1996 [22]. GGA appears on many occasions to give very good results than the L(S)DA. In particular, a better description of structural and magnetic properties is found using GGA. It was found that, while both L(S)DA and GGA produce accurate KS gaps, they tend to underestimate the true gap. This is because these approximate functionals do not have the discontinuous behavior, which result in Δ_{xc} is equal to zero.

1.6 Periodic system

Periodic assumption is a translational symmetry that can be used to reduce the computational effort when we are dealing with bulk systems. We can assume that the effective potential of the bulk system is a periodic function $V(\mathbf{r}) = V(\mathbf{r} + \mathbf{T})$, with $\mathbf{T}$ is a translational-vector of a given crystal structure. Therefore the domain of the real-space vector $\mathbf{r}$ is restricted to a small unit-cell called Wigner-Seitz cell. The crystal structure is defined as a repetition in the three spatial directions of unit-cell using the vector $\mathbf{T}$. The direct consequence of the translational symmetry in quantum mechanics is the Bloch theorem. It states that the single-particle wave function of periodic system obeys the following relation

$$\psi_{\mathbf{k}}(\mathbf{r}) = u_{\mathbf{k}}(\mathbf{r}) e^{i\mathbf{kr}}, \tag{1.69}$$

where the function $u_{\mathbf{k}}(\mathbf{r})$ is termed the envelope function and has the lattice periodicity

$$u_{\mathbf{k}}(\mathbf{r}) = u_{\mathbf{k}}(\mathbf{r} + \mathbf{T}). \tag{1.70}$$

The vector $\mathbf{k}$ which label the wave function is a good quantum number. It is in a fact a wave vector in which the wave function and the corresponding eigenvalues $\epsilon_{\mathbf{k}}$ are periodic functions in reciprocal space

$$\psi_{\mathbf{k}}(\mathbf{r}) = \psi_{\mathbf{k}+\mathbf{G}}(\mathbf{r}) \tag{1.71}$$

$$\epsilon_{\mathbf{k}} = \epsilon_{\mathbf{k}+\mathbf{G}}, \tag{1.72}$$

and $\mathbf{G}$ is the translational-vector of the reciprocal lattice defined by the condition $e^{i\mathbf{GT}} = 1$. Therefore it is obvious that the domain of $\mathbf{k}$ is limited to some unit cell in the reciprocal lattice. This unit cell can be chosen to define what is called the first Brillouin zone. It is the smallest volume that can be constructed in reciprocal lattice. It follows that the $\mathbf{k}$-integration for periodically systems can be reduced to the Brillouin zone domain.

1.7 Electronic structure methods

One way to efficiently solve the KS equations is to formulate the problem as a linear algebra eigenvalue equations. To do this, the single-particle KS wave function is expressed as linear combination of basis functions as

$$\psi_{i\mathbf{k}}(\mathbf{r}) = \sum_m c_{im}(\mathbf{k})\chi_m(\mathbf{r}). \tag{1.73}$$

In this regard, the methods of electronic structure differ according to the types of orbitals (basic functions) used, $\chi_m(\mathbf{r})$. There is a type of methods characterized by its use of analytic orbitals (called fixed orbitals) such as LCAO (linear combination of atomic orbitals). Other methods, based on augmentation, use partial waves as a basis function like the LAPW (linear augmented plane waves) and LMTO (linear muffin-tin orbitals). Following the Rayleigh-Ritz principle, the expansion coefficients, $c_{im}(\mathbf{k})$, are determined from the following secular equation:

$$\sum_m \left[H_{mm'} - \epsilon(\mathbf{k})S_{mm'}\right] c_{im}(\mathbf{k}) = 0, \tag{1.74}$$

where

$$H_{mm'} = \int_\Omega \chi_m^*(\mathbf{r}) \left(-\frac{1}{2}\nabla^2 + V(\mathbf{r})\right) \chi_{m'}(\mathbf{r}) d\mathbf{r} \tag{1.75}$$

are the Hamiltonian matrix elements and

$$S_{mm'} = \int_{\Omega} \chi_m^*(\mathbf{r})\chi_{m'}(\mathbf{r})d\mathbf{r} \tag{1.76}$$

are overlap matrix elements . The integrals in the above equations are evaluated over the unit cell volume, Ω, of a given crystal. The above set of linear equations can be formulated in a matrix form as

$$\det |H_{mm'} - \epsilon(\mathbf{k})S_{mm'}| = 0. \tag{1.77}$$

The diagonalization gives for each wave vector $\mathbf{k}$ the energy eigenvalues, which actually represent the band structure $\epsilon_n(\mathbf{k})$ of a given solid. The integer n is called the band index in which the energies distributed within bands.

Some electronic structure methods proceed differently in solving the electronic structure problem. These methods use the scattering theory as a basic approach. The Korringa-Kohn-Rostoker Green's function is one of this methods, which will be described later.

1.7.1 The linearized augmented plane wave

In fact, It results from the Bloch theorem that plane waves are natural candidates to form a complete set of basis functions. The advantage is that their overlap matrices are unitary matrices, because the plane waves are orthogonal. Moreover, the kinetic energy part of the single-particle Hamiltonian is diagonal in the basis of planes waves. However, we know for atoms close to the core region (the nucleus) that the wave function varies strongly with distance. So a large number of plane waves are required to better represents the wave function inside the core region. Furthermore, the rapid variation of the wave function leads to a poor convergence when using plane waves. Therefore, it is impractical in computations to use the plane waves as basis functions in direct manner. An approach to overcoming this problem is to work with a pseudopotential and a pseudo-wave function instead of the original potential and wave function. This technique is called pseudopotential method and treats very precisely the valence-band states with only a small set of plane waves. This desirable feature is due to the fact that the effective potential (pseudopotential) is a weak potential and thus the corresponding pseudo-wave-function is a very smoother function.

There is an another way to achieve the purpose—the accuracy and efficiency—of the pseudopotential method with additionally the all electrons (core and valence electrons) are treated carefully. This approach is based on the partitioning of space, consists in using for each region of space suitable basis functions. One of the first attempts in this direction is the augmented plane wave (APW) method introduced by Slater in 1937 [23].

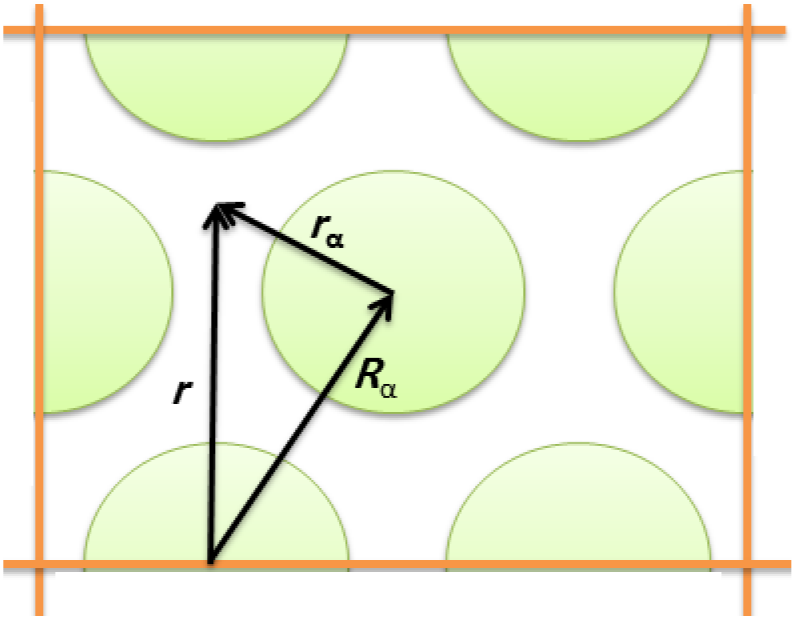

Figure 1.2: Schematic illustration of the muffin-tin spheres.

The APW approach

The idea behind the APW approach is that in region far away from the nuclei, the electrons are near free-like particles, and thus their wave functions can be sufficiently expanded by a small set of plane waves. Conversely, close to the nuclei, the electrons feels as if they are in free atoms, and their wave functions can be efficiently expressed by atomic-like functions. Therefore, the natural way to divide the space is the muffin-tin approximation (see Figure 1.2). In the muffin-tin construction, the space looks as a collection of non-overlapping spheres, each sphere centered on the atomic site $\mathbf{R}_\alpha$ of radius S_α. The remaining space, the region outside the spheres called the interstitial region. Inside the spheres the potential V is considered spherically symmetric and constant otherwise.

$$V(\mathbf{r}) = \begin{cases} \sum_\alpha v_\alpha(r_\alpha) & r_\alpha \in S_\alpha \\ \\ \text{constant} & \mathbf{r} \in \text{interstitial.} \end{cases} \tag{1.78}$$

Therefore, the plane waves provide a set of basis functions for the interstitial region. While a set of a linear combination of the products between radial wave functions and

spherical harmonics are the basis functions inside the spheres

$$\chi^{\mathrm{APW}}_{\mathbf{k}+\mathbf{G}_m} = \begin{cases} \frac{1}{\sqrt{\Omega}} e^{i(\mathbf{k}+\mathbf{G}_m)\mathbf{r}} & \mathbf{r} \in \text{interstitial} \\ \sum_{L\alpha} A^{\alpha}_{L}(\mathbf{k}+\mathbf{G}_m,\epsilon) u_{\ell\alpha}(r_\alpha,\epsilon) Y_L(\hat{\mathbf{r}}_\alpha) & r_\alpha \in S_\alpha, \end{cases} \tag{1.79}$$

where the index $L = (\ell, m_\ell)$ refers to the angular momentum and $Y_L(\hat{\mathbf{r}}) = Y_L(\theta,\phi)$ are the spherical harmonics with θ and ϕ are respectively the polar and azimuthal angles of the vectors $\mathbf{r}_\alpha = \mathbf{r} - \mathbf{R}_\alpha$. The coefficients $A^{\alpha}_{L}(\mathbf{k}+\mathbf{G}_m,\epsilon)$ are the expansion coefficients which have to be determined from the matching conditions. The functions, $u_{\ell\alpha}(r,\epsilon)$, are the regular solutions of the radial Schrodinger equation for atom α and energy ϵ

$$\left(-\frac{\partial^2}{\partial r^2} + \frac{\ell(\ell+1)}{r^2} + v_\alpha(r) - \epsilon\right) r u_{\ell\alpha}(r,\epsilon) = 0. \tag{1.80}$$

We can see that plane waves are augmented by partial waves inside the spheres leading to energy-dependent basis function. In other words, without specifying boundary conditions, the energy in the last equation can takes any value. For determining the expansion coefficients, A^{α}_{L}, one must confirms that the different basis functions are continues in value at the muffin-tin radius S_α. This matching condition can be easily imposed using Bauer's identity. Around the center of an atom α , plane waves are expanded in terms of spherical harmonics

$$\begin{aligned} e^{i\mathbf{K}_m\mathbf{r}} &= e^{i\mathbf{K}_m\mathbf{R}_\alpha} e^{i\mathbf{K}_m\mathbf{r}_\alpha} \\ &= 4\pi e^{i\mathbf{K}_m\mathbf{R}_\alpha} \sum_L i^\ell Y^*_L(\widehat{\mathbf{K}}_m) Y_L(\hat{\mathbf{r}}_\alpha) j_\ell(K_m r_\alpha), \end{aligned} \tag{1.81}$$

where $\mathbf{r} = \mathbf{r}_\alpha + \mathbf{R}_\alpha$, $\mathbf{K}_m = \mathbf{k} + \mathbf{G}_m$ and $j_\ell(kr)$ are spherical Bessel functions. $\widehat{\mathbf{K}}_m$ and $\hat{\mathbf{r}}_\alpha$ are the angular part of $\mathbf{K}_m$ and $\mathbf{r}_\alpha$ vectors, respectively. Therefore, the continuity condition at the muffin-tin surface sphere leads to

$$A^{\alpha}_{L}(\mathbf{K}_m,\epsilon) = \frac{4\pi}{\Omega} e^{i\mathbf{K}_m\mathbf{R}_\alpha} Y^*_L(\widehat{\mathbf{K}}_m) i^\ell \frac{j_\ell(K_m S_\alpha)}{u_{\ell\alpha}(S_\alpha,\epsilon)}. \tag{1.82}$$

At this point, both Hamiltonian and overlap matrices can be defined using the explicit expression of the APW-basis functions $\chi_{\mathbf{k}+\mathbf{G}_m}(\mathbf{r})$. This leads to a set of linear homogeneous equations of the following form

$$\mathbf{M}(\epsilon)\mathbf{c} = \mathbf{0}, \tag{1.83}$$

where $\mathbf{M}(\epsilon)$ is a matrix in which its elements depend nonlinearly in energy and $\mathbf{c}$ is a vector of the corresponding coefficient elements. The detailed derivation of the above

equation is found in the book by Loucks (1967) [24]. It should be pointed out that, due to this nonlinear eigenvalue problem, the solution of the Equation (1.83) cannot be easily determined in a single diagonalization as in the standard linear algebra problem. This makes the APW method slower than other methods such as the pseudopotential method, although the size of its basis functions set is much smaller.

The concept of linearization

The problem of nonlinear energy dependence in the secular equation can be avoided by using the idea of linearization. The concept was introduced by Andersen in 1975 [25]. It gives a set of linear homogeneous equations that are linear in energy, combining desired features of a partial waves (accuracy) and fixed functions (efficiency) based methods. The way to do this is to energy linearizes the radial solution $u_\ell(r,\epsilon)$, by a Taylor expansion around an arbitrary reference energy ϵ_ν:

$$u_\ell(r,\epsilon) = u_\ell(r,\epsilon_\nu) + \dot{u}_\ell(r,\epsilon_\nu)(\epsilon-\epsilon_\nu) + O(\epsilon-\epsilon_\nu)^2, \tag{1.84}$$

where $\dot{u}_\ell = \frac{\partial u_\ell}{\partial \epsilon}$ is the energy derivative of the radial function, and $O(\epsilon-\epsilon_\nu)^2$ is the error that can be made which is quadratic in $\epsilon-\epsilon_\nu$. While the error in the wave-functions is of the order of $O(\epsilon-\epsilon_\nu)^2$, the corresponding band energies which are determined from the variational principle are accurate with $O(\epsilon-\epsilon_\nu)^4$ error. Therefore, the linearization of the APW leads to an accuracy over a wider energy window. It can be shown that the functions, $\dot{u}_\ell(r,\epsilon_\nu)$, are orthogonal to the radial functions, $u_\ell(r,\epsilon_\nu)$. This indicates that these two functions can be linearly combined to form a new radial function for basis functions inside the spheres

$$\chi^{\mathrm{LAPW}}_{\mathbf{k}+\mathbf{G}_m} = \begin{cases} \frac{1}{\sqrt{\Omega}} e^{i(\mathbf{k}+\mathbf{G}_m)\mathbf{r}} & \mathbf{r} \in \text{interstitial} \\ \sum_{L\alpha} \left\{ a^\alpha_L(\mathbf{k}+\mathbf{G}_m) u_{\ell\alpha}(r_\alpha,\epsilon_\nu) + b^\alpha_L(\mathbf{k}+\mathbf{G}_m)\dot{u}_{\ell\alpha}(r_\alpha,\epsilon_\nu) \right\} Y_L(\hat{\mathbf{r}}_\alpha) & r_\alpha \in S_\alpha, \end{cases} \tag{1.85}$$

These are the linearized augmented plane wave (LAPW) basis functions which are energy independent functions. The expansion coefficient $a^\alpha_L(\mathbf{k}+\mathbf{G}_m)$ and $b^\alpha_L(\mathbf{k}+\mathbf{G}_m)$ are determined by requiring the basis functions to be continuous in value and in slope at the muffin-tin sphere α. The energy derivative of the radial function is determined from the the energy derivative of the radial Schrodinger equation, Equation (1.80), as

$$\left(-\frac{\partial^2}{\partial r^2} + \frac{\ell(\ell+1)}{r^2} + v_\alpha(r) - \epsilon \right) r\dot{u}_{\ell\alpha}(r,\epsilon) = r u_{\ell\alpha}(r,\epsilon). \tag{1.86}$$

The Hamiltonian and overlap matrices in terms of LAPW basis functions are slightly modified from that based on APW method, with the advantage that the LAPW matrices are energy independent. As a result, only a simple diagonalization of the corresponding secular equation can be made to solve the electronic problem.

The LAPW method accurately deals with sufficiently extended states such as valence states. The core states are very localized around each atom, defined with a good approximation to be orthogonal to the valence states. These localized states are treated separately from the LAPW method using atomic-like calculations, which pose no problem. However, in the intermediate between core and valence states, there are the so-called semi-core states that pose some difficulties. The semi-core states cannot be treated separately as core states. Because they are neither fully enclosed in muffin-tin spheres nor high enough in energy to be accurately treated as valence states. Extension like Local Orbital (LO) scheme and related concepts work well for this kind of problems, and the interested reader is referred to the book provided by Singh and Nordstrom for a detailed description [26].

Full potential

To go beyond muffin-tin approximation, it requires scheme that employs no shape approximation for the potential. The LAPW method can be easily generalized to include the non-spherical part of the potential. This approach is called a full-potential LAPW (F-LAPW) method [27, 28]. The procedure is done by expanding the potential by plane waves in the interstitial region and by spherical harmonics inside each sphere

$$V(\mathbf{r}) = \begin{cases} \sum_{\mathbf{G}} \tilde{V}_{\mathbf{G}} e^{i\mathbf{G}\mathbf{r}} & \text{interstitial region} \\ \sum_{L} V_L(r) Y_L(\hat{\mathbf{r}}) & \text{muffin-tin spheres.} \end{cases} \tag{1.87}$$

Similarly, the electron density, $n(\mathbf{r})$, is also expanded

$$n(\mathbf{r}) = \begin{cases} \sum_{\mathbf{G}} \tilde{n}_{\mathbf{G}} e^{i\mathbf{G}\mathbf{r}} & \text{interstitial region} \\ \sum_{L} n_L(r) Y_L(\hat{\mathbf{r}}) & \text{muffin-tin spheres,} \end{cases} \tag{1.88}$$

where $\tilde{V}_{\mathbf{G}}$ and $\tilde{n}_{\mathbf{G}}$ are the Fourier components of potential and electron density, respectively. For efficient procedure, the above expansions are subject to symmetry constraint; lattice harmonics inside the spheres and stars in the interstitial [26].

1.7.2 The Korringa-Kohn-Rostoker Green's function

In principle, all information about the electronic structure of a given system that is provided by wave functions-based methods (in terms of eigenvalues E_μ and eigenfunctions ψ_μ) can also be obtained through the description based on the Green's function [29]. The latter can be determined directly in the Korringa-Kohn-Rostoker scheme. In this approach, the propagation of the electron in the solid is viewed as a multiple scattering problem. The formal introduction is the resolvent of the single- particle Schrodinger equation [30]

$$(E - H)\, G(\mathbf{r}, \mathbf{r}', E) = \delta(\mathbf{r} - \mathbf{r}'). \tag{1.89}$$

Using the spectral representation, the Green's function can be reads

$$G(\mathbf{r}, \mathbf{r}', E) = \lim_{\epsilon \to 0} \sum_{\mu} \frac{\psi_\mu(\mathbf{r}) \psi_\mu^*(\mathbf{r}')}{E + i\epsilon - E_\mu}. \tag{1.90}$$

The charge density $\rho(\mathbf{r})$ and the density of states $n(E)$ are directly expressed by energy and volume integral of the imaginary part of the Green's function, respectively:

$$\rho(\mathbf{r}) = -\frac{1}{\pi}\int^{E_\mathrm{F}} \Im G(\mathbf{r},\mathbf{r},E)d\mathbf{r}, \tag{1.91}$$

$$n(E) = -\frac{1}{\pi}\int_V \Im G(\mathbf{r},\mathbf{r},E)d\mathbf{r}. \tag{1.92}$$

The multiple scattering formalism gives a direct way to determine the Green's function, and hence a direct access to physical quantities. In operator representation, $G(\mathbf{r},\mathbf{r}',E) = \langle\mathbf{r}|G(E)|\mathbf{r}'\rangle$ and $\delta(\mathbf{r},\mathbf{r}') = \langle\mathbf{r}|\mathbf{r}'\rangle$ with $|\mathbf{r}\rangle$ is the ket associated to the wave function in the $\mathbf{r}$-representation, the operator form of the Green's function, $G(E)$, is written

$$\begin{aligned} G(E) &= (E - H_0 - V)^{-1} \\ &= (E - H_0)^{-1}\left[1 + VG(E)\right] \\ &= G^0(E) + G^0(E)VG(E), \end{aligned} \tag{1.93}$$

with $G^0(E) = (E - H_0)^{-1}$ is the Green's function operator of the reference system, assumed to be easy determined. The potential V is the source of all scattering events that can occur. For bulk systems, the free-space can represent the reference system in order to compute the Green's function. The structure of the $G(E)$ in the last equation allows it to decompose self-consistently into a sum of infinite terms

$$\begin{aligned} G &= G^0 + G^0VG \\ &= G^0 + G^0V(G^0 + G^0VG) \\ &= G^0 + G^0VG^0 + G^0VG^0VG^0 + \ldots, \end{aligned} \tag{1.94}$$

which can be written in a compact form

$$G = G^0 + G^0TG^0. \tag{1.95}$$

The operator T writes

$$\begin{aligned} T &= V + VG^0V + \ldots \\ &= V + VG^0T \\ &= \left(1 - VG^0\right)^{-1}V. \end{aligned} \tag{1.96}$$

In $\mathbf{r}$-representation the Green's function can be expressed as

$$\begin{aligned} G(\mathbf{r},\mathbf{r}',E) = G^0(\mathbf{r},\mathbf{r}',E) + \iint G^0(\mathbf{r},\mathbf{r}_1,E) \\ \times T(\mathbf{r}_1\mathbf{r}_2,E)G^0(\mathbf{r}_2,\mathbf{r}',E)d\mathbf{r}_1d\mathbf{r}_2, \end{aligned} \tag{1.97}$$

with $G^0(\mathbf{r},\mathbf{r}',E) = \langle\mathbf{r}|G^0(E)|\mathbf{r}'\rangle$ and $T(\mathbf{r},\mathbf{r}',E) = \langle\mathbf{r}|T(E)|\mathbf{r}'\rangle$. The wave function can also be expressed by the T-operator through the Lippmann-Schwinger equation. First, the wave function is written as an integral containing the potential

$$\psi(\mathbf{r}) = \chi(\mathbf{r}) + \int G^0(\mathbf{r},\mathbf{r}',E)V(\mathbf{r}')\psi(\mathbf{r}')d\mathbf{r}', \tag{1.98}$$

with the corresponding Schrodinger equations $(H_0+V)\psi = E\psi$ and $H_0\chi = E\chi$. To make it easier, we proceed with the operator formalism, where $\psi(\mathbf{r}) = \langle\mathbf{r}|\psi\rangle$, $\chi(\mathbf{r}) = \langle\mathbf{r}|\chi\rangle$ and using the closure relation $\int|\mathbf{r}\rangle\langle\mathbf{r}|d\mathbf{r} = 1$, the Lippmann-Schwinger equation is written

$$|\psi\rangle = |\chi\rangle + G^0V|\psi\rangle. \tag{1.99}$$

Or

$$|\psi\rangle = |\chi\rangle + G^0T|\chi\rangle. \tag{1.100}$$

By identification we find a useful relation

$$V|\psi\rangle = T|\chi\rangle. \tag{1.101}$$

Hence in $\mathbf{r}$-representation

$$\psi(\mathbf{r}) = \chi(\mathbf{r}) + \iint G^0(\mathbf{r},\mathbf{r}_1,E)T(\mathbf{r}_1,\mathbf{r}_2,E)\chi(\mathbf{r}_2)d\mathbf{r}_1d\mathbf{r}_2, \tag{1.102}$$

At this point it is obvious that the solution to the problem lies in how to deal with the T-operator, which contains all the information about scattering. The first step is to solve the single-site scattering problem by decomposing the system into atomic regions. The way to do this, is to consider an isolated atomic region (sphere bounding the potential region) embedded in free-electron-like space. This requires solving the radial Schrodinger differential equation and the spherical Bessel differential equation inside and outside the spheres, respectively. At this level, it is shown that the single-site T-matrix describes the on-site scattering from the incoming wave to outgoing one. In the second step, the entire system with embedded multi-atomic regions in the free space is treated as a multiple scattering problem. In this formalism, the free wave propagation between spheres is described by what is called a structure constant. The latter connects the scattering events between the scatterer centers. This provides the feature that the potential aspects of the system are separated from the structural aspects. The information about the atoms is contained in the single-site T-matrix, while everything about the crystal structure is given by structure constants.

Single-site scattering problem

- **Spherical potential**

The subject of multiple scattering theory is the study of the electronic structure of the overall system as a problem of a propagation of electrons through a collection of single scatterers. The idea is to decompose the potential V of the system into a sum of nonoverlapping single-site potential, v^n, as

$$V(\mathbf{r}) = \sum_n v^n(\mathbf{r}). \tag{1.103}$$

The first procedure consists in dealing with a single scatterer. Thus, at this step, only the individual potential, v^n, is considered. This is the aim of the single-site scattering formalism. In the simplest case, the potential of the single-site scatterer enclosed by a sphere of radius S is assumed to be spherically symmetric, where

$$v^n(\mathbf{r}) = \begin{cases} v^n(r) & r \leq S \\ \\ 0 & \text{otherwise.} \end{cases} \tag{1.104}$$

The procedure can be straightforwardly generalized to an arbitrarily potential of general shape. In the region of a free electron system, $v^n(\mathbf{r}) = 0$, the Green's function is expressed as

$$G^0(\mathbf{r}, \mathbf{r}', E) = -\frac{1}{4\pi} \frac{e^{ik|\mathbf{r}-\mathbf{r}'|}}{|\mathbf{r}-\mathbf{r}'|}, \tag{1.105}$$

where $k = \sqrt{E}$. The Green's function of the free-electron system can be expanded in terms of spherical harmonics

$$G^0(\mathbf{r}, \mathbf{r}', E) = \sum_L Y_L(\hat{\mathbf{r}}) G^0_\ell(r, r', E) Y_L(\hat{\mathbf{r}}'), \tag{1.106}$$

with $G^0_\ell(r, r', E) = -i\sqrt{E} j_\ell(\sqrt{E} r_<) h_\ell(\sqrt{E} r_>)$, where $r_<(r_>)$ indicates the smaller (larger) value of r and r', or the free Green's function can be written as

$$G^0(\mathbf{r}, \mathbf{r}', E) = -i\sqrt{E} \sum_L j_L(\sqrt{E}\mathbf{r}_<) h_L(\sqrt{E}\mathbf{r}_>), \tag{1.107}$$

where $j_L(\sqrt{E}\mathbf{r}) = j_\ell(\sqrt{E}r) Y_L(\hat{\mathbf{r}})$ and $h_L(\sqrt{E}\mathbf{r}) = h_\ell(\sqrt{E}r) Y_L(\hat{\mathbf{r}})$ with j_ℓ are the spherical Bessel functions, h_ℓ are the spherical Hankel functions. $h_\ell = j_\ell + i n_\ell$, with n_ℓ are the spherical Neumann functions. It can be seen that both regular j_ℓ and

irregular h_ℓ solutions are required for the spherical partial-waves expansion of the Green's function of the free system. Expanding the wave functions of the free space in spherical harmonic and partial-waves

$$\begin{aligned}\chi(\mathbf{r}) &= e^{i\mathbf{kr}} \\ &= 4\pi \sum_L i^\ell Y_L^*(\hat{\mathbf{k}}) Y_L(\hat{\mathbf{r}}) j(\sqrt{E}r) \\ &= 4\pi \sum_L i^\ell Y_L^*(\hat{\mathbf{k}}) \chi_L(\mathbf{r}),\end{aligned} \tag{1.108}$$

with $\chi_L(\mathbf{r}) = j_\ell(\sqrt{E}\mathbf{r})Y_L(\hat{\mathbf{r}})$. Analogously, the wave function of the single-site scattering region can also be expanded

$$\psi^n(\mathbf{r}) = 4\pi \sum_L i^\ell Y_L^*(\hat{\mathbf{k}}) \psi_L^n(\mathbf{r}). \tag{1.109}$$

The partial waves, $\psi_L^n(\mathbf{r})$, are not known analytically, but can be determined numerically. Inserting both Equation (1.108) and Equation (1.109) in the Lippmann-Schwinger equations, Equation (1.98), and using the orthonormality relation of the spherical harmonics, $\int Y_L^*(\hat{\mathbf{k}}) Y_{L'}(\hat{\mathbf{k}}) d\hat{\mathbf{k}} = \delta_{LL'}$, respectively yields

$$\psi_L^n(\mathbf{r}) = \chi_L(\mathbf{r}) + \int G^0(\mathbf{r}, \mathbf{r}', E) v^n(\mathbf{r}') \psi_L^n(\mathbf{r}') d\mathbf{r}'. \tag{1.110}$$

For the case of the potential with spherical symmetry, $\psi_L^n(\mathbf{r}, E) = R_\ell^n(r, E)Y_L(\hat{\mathbf{r}})$, where the radial basis function, $R_\ell^n(r, E)$, is a regular function, *i.e.*, it vanishes at the origin (converged). For the individual potential the corresponding radial basis functions $R_\ell^n(r, E)$ obey the radial differential Schrodinger equations

$$\left(-\frac{1}{r}\frac{\partial^2}{\partial r^2} r + \frac{\ell(\ell+1)}{r^2} + v^n(r) - E \right) R_\ell^n(r, E) = 0. \tag{1.111}$$

By making $d\mathbf{r} = r^2 dr d\hat{\mathbf{r}}$ with $d\hat{\mathbf{r}} = \sin(\theta) d\theta d\phi$ and using the orthogonality relations in real-space $\int Y_L^*(\hat{\mathbf{r}}) Y_{L'}(\hat{\mathbf{r}}) d\hat{\mathbf{r}} = \delta_{LL'}$,

$$R_\ell^n(r, E) = j_\ell(\sqrt{E}r) + \int_0^S G_\ell^0(r, r', E) v^n(r') R_\ell^n(r', E) r'^2 dr'. \tag{1.112}$$

In which for $(r > S)$, the spherical free Green's function can be replaced with its expression, and we obtain

$$\begin{aligned}R_\ell^n(r, E) = j_\ell(\sqrt{E}r) - i\sqrt{E} h_\ell(\sqrt{E}r) \\ \times \int_0^S j_\ell(\sqrt{E}r') v^n(r') R_\ell^n(r', E) r'^2 dr'.\end{aligned} \tag{1.113}$$

The multiplication from the left of Equation (1.101) by $\langle\chi|$ yields in the single-site scattering problem

$$\langle\chi|v^n|\psi\rangle = \langle\chi|t^n|\chi\rangle, \tag{1.114}$$

which can be written in **r**-representation as

$$\int \chi^*(\mathbf{r})v^n(r)\psi(\mathbf{r})d\mathbf{r} = \iint \chi^*(\mathbf{r})t^n(\mathbf{r},\mathbf{r}',E)\chi(\mathbf{r}')d\mathbf{r}d\mathbf{r}'. \tag{1.115}$$

Expressing the wave functions with their angular-momentum partial-wave expansions, and using the orthogonality relation of the spherical harmonics in **k**-space we obtain

$$\int \chi_L^*(\mathbf{r})v^n(r)\psi_L(\mathbf{r})d\mathbf{r} = \iint \chi_L^*(\mathbf{r})t^n(\mathbf{r},\mathbf{r}',E)\chi_L(\mathbf{r}')d\mathbf{r}d\mathbf{r}'. \tag{1.116}$$

The above equality can be written in a final form by expressing the integral in polar coordinates. Using both orthogonality and orthonormality relations in **r**-space and expanding the single-site T-matrix in terms of spherical harmonics

$$t^n(\mathbf{r},\mathbf{r}',E) = \sum_L Y_L(\hat{\mathbf{r}})t_\ell^n(r,r',E)Y_L(\hat{\mathbf{r}}'), \tag{1.117}$$

which yields

$$\begin{aligned}\int_0^{r=S} j_\ell(\sqrt{E}r)v^n(r)R_\ell^n(r,E)r^2dr = &\int_0^{r=S}\int_0^{r'=S} j_\ell(\sqrt{E}r) \\ &\times t_\ell^n(r,r',E)j_\ell(\sqrt{E}r')r^2drr'^2dr' \\ &= t_\ell^n(E).\end{aligned} \tag{1.118}$$

or, in Dirac notation

$$\begin{aligned}\langle j_\ell|v^n|R_\ell^n(E)\rangle &= \langle j_\ell|t^n(E)|j_\ell\rangle \\ &= t_\ell^n(E),\end{aligned} \tag{1.119}$$

with $j_\ell(\sqrt{E}r) = \langle\sqrt{E}r|j_\ell\rangle$, $R_\ell^n(r,E) = \langle r|R_\ell^n(E)\rangle$ and $v^n(r)\delta(r-r') = \langle r|v^n|r'\rangle$. The scattering quantities, $t_\ell^n(E)$, are the single-site T-matrix elements in the L-representation. They can be evaluated by an integration using the left-hand side of Equation (1.118), assuming that R_ℓ^n can be calculated.
Thus, the regular solutions can be expressed outside the sphere (free-space) in terms of the single-site T-matrix elements t_ℓ^n as

$$R_\ell^n(r,E) = j_\ell(\sqrt{E}r) - i\sqrt{E}t_\ell^n(E)h_\ell(\sqrt{E}r) \qquad (r \geq S). \tag{1.120}$$

For practical purposes, the single-site T-matrix elements are determined by matching between solutions as well as their first-derivatives inside and outside muffin-tin region

$$\left.\frac{R_\ell^{n\prime}(r,E)}{R_\ell^n(r,E)}\right|_{r=S} = \left.\frac{j_\ell{}'(\sqrt{E}r) - t_\ell^n(E)h_\ell{}'(\sqrt{E}r)}{j_\ell(\sqrt{E}r) - t_\ell^n(E)h_\ell(\sqrt{E}r)}\right|_{r=S}, \tag{1.121}$$

then

$$t_\ell^n(E) = \left.\frac{1}{i\sqrt{E}}\frac{R_\ell^n(r,E)j_\ell{}'(\sqrt{E}r) - R_\ell^{n\prime}(r,E)j_\ell(\sqrt{E}r)}{R_\ell^n(r,E)h_\ell{}'(\sqrt{E}r) - R_\ell^{n\prime}(r,E)h_\ell(\sqrt{E}r)}\right|_{r=S}, \tag{1.122}$$

where $f' = \frac{df}{dr}$ [31].
In analogy with the expression of the Green's function of the free system, the single-site Green's function can also be expanded in terms of regular and irregular solutions. To proceed, we use the ansatz

$$G^n(\mathbf{r},\mathbf{r}',E) = \sum_L Y_L(\hat{\mathbf{r}})G_\ell^n(r,r',E)Y_L(\hat{\mathbf{r}}'), \tag{1.123}$$

and inserting this expression with both Equation (1.106) and Equation (1.117) in the single site form of Equation (1.102). Using the spherical harmonics orthogonality relations we obtain

$$\begin{aligned} G_\ell^n(r,r',E) = G_\ell^0(r,r',E) + \int_0^{r_1=S}\int_0^{r_2=S} & G_\ell^0(r,r_1,E) \\ & \times t_\ell^n(r_1r_2,E)G_\ell^0(r_2,r',E){r_1}^2dr_1{r_2}^2dr_2, \end{aligned} \tag{1.124}$$

or in operator formalism

$$G_\ell^n(E) = G_\ell^0(E) + G_\ell^0(E)t_\ell^n(E)G_\ell^0(E). \tag{1.125}$$

In the case of $(r > r' > S)$ and with use of the spherical (polar) coordinates taking into account the orthogonality relation of the spherical harmonic functions, one finds

$$\begin{aligned} G_\ell^n(\mathbf{r},\mathbf{r}',E) &= -i\sqrt{E}j_L(\sqrt{E}\mathbf{r}_<)h_L(\sqrt{E}\mathbf{r}_>) \\ &\quad - Eh_L(\sqrt{E}\mathbf{r}_<)t_\ell^n(E)h_L(\sqrt{E}\mathbf{r}_>) \\ &= -i\sqrt{E}\left[j_L(\sqrt{E}\mathbf{r}_<) - i\sqrt{E}t_\ell^n(E)h_L(\sqrt{E}\mathbf{r}_<)\right]h_L(\sqrt{E}\mathbf{r}_>). \end{aligned} \tag{1.126}$$

Thus, the single-site Green's function can be written in the same way as the free Green's function

$$G^n(\mathbf{r},\mathbf{r}',E) = -i\sqrt{E}\sum_L R_L^n(\mathbf{r}_<,E)H_L^n(\mathbf{r}_>,E), \tag{1.127}$$

with the regular and irregular solution are defined respectively,

$$R_L^n(\mathbf{r}, E) = j_L(\sqrt{E}\mathbf{r}) - i\sqrt{E}t_\ell^n(E)h_L(\sqrt{E}\mathbf{r}), \tag{1.128}$$

$$H_L^n(\mathbf{r}, E) = h_L(\sqrt{E}\mathbf{r}) \qquad \text{for} \qquad r \geq S. \tag{1.129}$$

From another point of view, a different kind of regular Z_L and irregular J_L functions, called scattering solutions, are adopted in order to write the Green's function in terms of scattering quantities [32].

$$Z_L^n(\mathbf{r}, E) = j_L(\sqrt{E}\mathbf{r})t_\ell^n(E)^{-1} - i\sqrt{E}h_L(\sqrt{E}\mathbf{r}), \tag{1.130}$$

$$J_L^n(\mathbf{r}, E) = j_L(\sqrt{E}\mathbf{r}) \qquad \text{for} \qquad r \geq S. \tag{1.131}$$

Eventually, the single-site Green's function can be rewritten as

$$G^n(\mathbf{r}, \mathbf{r}', E) = \sum_L Z_L^n(\mathbf{r}, E)t_L^n(E)Z_L^n(\mathbf{r}', E) - \sum_L Z_L^n(\mathbf{r}_<, E)J_L^n(\mathbf{r}_>, E). \tag{1.132}$$

- **Full potential**

  In general, the potential is anisotropic, which has a non-spherical contribution, especially for those systems with open structures or systems with broken symmetry. The generalization to potential of arbitrary shape can be done by expanding the potential and the basis functions in terms of spherical harmonics functions [33, 34].

$$V(\mathbf{r}) = \sum_L V_L(r)Y_L(\hat{\mathbf{r}}), \tag{1.133}$$

$$R_L(\mathbf{r}, E) = \sum_{L'} R_{LL'}(r, E)Y_L(\hat{\mathbf{r}}). \tag{1.134}$$

  Then, all the required integrals are convoluted using the the shape function $\Theta(\mathbf{r})$. The latter is also expanded in spherical harmonics

$$\Theta(\mathbf{r}) = \sum_L \Theta_L(r)Y_L(\hat{\mathbf{r}}), \tag{1.135}$$

  which equal 1(0) inside(outside) the Wigner-Seitz cell.
  This procedure further complicates the calculations, since system of coupled radial equations have to be solved. Practically, this problem can be bypassed by iterative schemes in which the non-spherical part of the potential can be treated as a perturbation. This can be justified because the potential inside the sphere is of central-like character, so the expansion of a finite amount of angular-momentum is sufficient.

Multiple scattering theory

In the general case the potential consists of multiple scatterers embedded in free space. In multiple scattering theory, the potential V of the total system is treated as a collection of single-potentials v^n. In operator representation the potential reads $V = \sum_n v^n$, and the corresponding T-matrix is written

$$\begin{aligned} T &= \sum_n v^n + \sum_{n,m} v^n G^0 v^m + \sum_{n,m,l} v^n G^0 v^m G^0 v^l + \dots \\ &= \sum_n T_n, \end{aligned} \tag{1.136}$$

with T^n is defined and expressed in terms of the single-site T-matrix as

$$\begin{aligned} T_n &= v^n + \sum_m v^n G^0 v^m + \sum_{m,l} v^n G^0 v^m G^0 v^l + \dots \\ &= v^n + v^n G^0 \left(\sum_{m \neq n} T_m - T_n \right) \\ &= t^n + t^n G^0 \sum_{m \neq n} T_m. \end{aligned} \tag{1.137}$$

where the single-site T-matrix elements is defined as

$$t^n = \left(1 - v^n G^0\right)^{-1} v^n. \tag{1.138}$$

In terms of the *scattering path operator*, τ^{nm} [35], the T-matrix can be re-expressed as

$$T = \sum_{n,m} \tau^{nm}. \tag{1.139}$$

This implies

$$T_n = \sum_m \tau^{nm}. \tag{1.140}$$

One can write Equation (1.137) as

$$T_n = t^n + t^n G^0 \left(\sum_m T_m - T_n \right). \tag{1.141}$$

Inserting the expression of T^n, Equation (1.140), in both sides of the last equation

$$\sum_m \tau^{nm} = \sum_m t^n \delta_{nm} + t^n G^0 \left(\sum_m \sum_k \tau^{km} - \sum_m \tau^{nm} \right). \tag{1.142}$$

The sum can be eliminated

$$\begin{aligned}\tau^{nm} &= t^n\delta_{nm} + t^n G^0\left(\sum_k \tau^{km} - \tau^{nm}\right) \\ &= t^n\delta_{nm} + t^n G^0 \sum_{k\neq n} \tau^{km}.\end{aligned} \tag{1.143}$$

Or in **r**-representation

$$\begin{aligned}\tau^{nm}(\mathbf{r},\mathbf{r}') = t^n(\mathbf{r},\mathbf{r}')\delta_{nm} + \sum_{k\neq n}\iint t^n(\mathbf{r},\mathbf{r}'') \\ \times G^0(\mathbf{r}'',\mathbf{r}''')\tau^{km}(\mathbf{r}''',\mathbf{r}')d\mathbf{r}''d\mathbf{r}'''.\end{aligned} \tag{1.144}$$

While t_l^n defines all the scattering events produced at a single site, τ^{nm} describes the scattering effects from one site to another one including all the scattering events in-between. Further manipulation in Equation (1.143) leads to

$$\sum_k \left[(t^n)^{-1}\delta_{nk} - G^0(1-\delta_{nk})\right]\tau^{kn} = \delta_{nm}. \tag{1.145}$$

This can be reformulated in a matrix form in which the scattering path operator reads

$$\tau = M^{-1}, \tag{1.146}$$

$$M_{nm} = (t^n)^{-1}\delta_{nm} - G^0(1-\delta_{nm}). \tag{1.147}$$

It is convenient to work with cell-centered coordinates, where $\mathbf{r} = \mathbf{r}_n + \mathbf{R}_n$ and $\mathbf{r}' = \mathbf{r}'_m + \mathbf{R}_m$. The coordinates $\mathbf{r}_n$ and $\mathbf{r}'_m$ are respectively confined inside cells n and m. The cells are centered at the atomic positions $\mathbf{R}_n$ and $\mathbf{R}_m$. In this framework, the free Green's function is expanded by the spherical harmonics using the real-space structure constants, $G_{LL}^{0,nm}(E)$, as expansion coefficients which called KKR structure constants, [36, 37]

$$\begin{aligned}G^0(\mathbf{r}_n+\mathbf{R}_n,\mathbf{r}'_m+\mathbf{R}_m) = \delta_{nm}G^0(\mathbf{r}_n,\mathbf{r}'_n) \\ + (1-\delta_{nm})\sum_{LL'} j_L(\sqrt{E}\mathbf{r}_n)G_{LL'}^{0,nm}(E)j_{L'}(\sqrt{E}\mathbf{r}'_m),\end{aligned} \tag{1.148}$$

with

$$\begin{aligned}G^0(\mathbf{r}_n,\mathbf{r}'_n) = -i\sqrt{E}\Bigg[\sum_L j_L(\sqrt{E}\mathbf{r}_n)h_L(\sqrt{E}\mathbf{r}'_n)\Theta(\mathbf{r}'_n-\mathbf{r}_n) \\ + \sum_L h_L(\sqrt{E}\mathbf{r}_n)j_L(\sqrt{E}\mathbf{r}'_n)\Theta(\mathbf{r}_n-\mathbf{r}'_n)\Bigg],\end{aligned} \tag{1.149}$$

where $\Theta(r)$ is the Heaviside function equal to 1(0) when $r > (<)0$. Replacing the expression of the free Green's function in the Equation (1.144) with its new cell-centered form (the above equation), multiplying from the left and from the right of Equation (1.144) by $J_L(\sqrt{E}\mathbf{r}_n)$ and $J_{L'}(\sqrt{E}\mathbf{r}'_m)$, respectively, and carrying the integrals in $\mathbf{r}_n$- and $\mathbf{r}'_m$-space gives the fundamental equation of motion for the scattering path operator in multiple scattering theory

$$\tau^{nm}_{LL'}(E) = t^n_L(E)\delta_{nm} + t^n_L(E)\left(\sum_{k\neq n}\sum_{L''} G^{0,nk}_{LL''}(E)\tau^{km}_{L''L'}(E)\right), \tag{1.150}$$

with the scattering path operator elements are defined

$$\tau^{nm}_{LL'}(E) = \iint j_L(\sqrt{E}\mathbf{r}_n)\tau^{nm}(\mathbf{r}_n + \mathbf{R}_n, \mathbf{r}'_m + \mathbf{R}_m, E) j_{L'}(\sqrt{E}\mathbf{r}'_m) d\mathbf{r}_n d\mathbf{r}'_m. \tag{1.151}$$

In terms of matrices the equation of motion reads,

$$\begin{aligned}\underline{\tau}^{nm}(E) &= \underline{t}^n(E)\delta_{nm} + \underline{t}^n(E)\sum_{k\neq n}\underline{G}^{0,nk}(E)\underline{\tau}^{kn}(E) \\ &= \underline{t}^n(E)\delta_{nm} + \sum_{k\neq m}\underline{\tau}^{nk}\underline{G}^{0,km}(E)\underline{t}^n(E),\end{aligned} \tag{1.152}$$

where the underlined objects are matrices with respect to angular-momentum index L, for instance, $(\underline{\tau}^{nm}_{LL'}) = \tau^{nm}_{LL'}$.
In the case of periodic system the above equation of motion can be solved by a Brillouin zone (BZ) integration

$$\underline{\tau}^{nm}(E) = \frac{1}{\Omega_{\mathrm{BZ}}}\int_{\mathrm{BZ}}\left[\underline{t}(E)^{-1} - \underline{G}^0(\mathbf{k}, E)\right]^{-1} e^{-i\mathbf{k}\mathbf{R}_{nm}} d\mathbf{k}, \tag{1.153}$$

where $\underline{G}^0(\mathbf{k}, E)$ is the Fourier transform of the real-space structure constant matrix.

Green's Function

In the previous subsections, we have seen two fundamental steps for the construction of the Green's function for a system of a multi scatterers. In terms of the scattering path operator, the Green's function can be written with cell-centered coordinates as

$$\begin{aligned}G(\mathbf{r}_n + \mathbf{R}_n, \mathbf{r}'_m + \mathbf{R}_m) &= G^0(\mathbf{r}_n + \mathbf{R}_n, \mathbf{r}'_m + \mathbf{R}_m) \\ &+ \sum_{ij}\iint G^0(\mathbf{r}_n + \mathbf{R}_n, \mathbf{r}''_i + \mathbf{R}_i)\tau^{ij}(\mathbf{r}''_i + \mathbf{R}_i, \mathbf{r}'''_j + \mathbf{R}_j) \\ &\times G^0(\mathbf{r}'''_j + \mathbf{R}_j, \mathbf{r}'_m + \mathbf{R}_m) d\mathbf{r}'' d\mathbf{r}'''.\end{aligned} \tag{1.154}$$

We can reformulate the expression of the free Green's function, Equation (1.148), in vector and matrix notation

$$\begin{aligned} G^0(\mathbf{r}_n + \mathbf{R}_n, \mathbf{r}'_m + \mathbf{R}_m) = (1 - \delta_{nm}) \left\langle J(\mathbf{r}_n) \left| \underline{G}^{0,nm} \right| J(\mathbf{r}'_m) \right\rangle \\ - i\sqrt{E}\delta_{nm} \left[\langle J(\mathbf{r}_n) | H(\mathbf{r}'_n) \rangle \, \Theta(\mathbf{r}'_n - \mathbf{r}_n) \right. \\ \left. + \, \langle H(\mathbf{r}_n) | J(\mathbf{r}'_n) \rangle \, \Theta(\mathbf{r}_n - \mathbf{r}'_n) \right]. \end{aligned} \tag{1.155}$$

Here, $|F\rangle$ denotes a vector with f_L elements. Inserting the above equation in Equation (1.154) and with some manipulation and simplification taking into account that $\tau^{nm}(\mathbf{r}_n + \mathbf{R}_n, \mathbf{r}'_m + \mathbf{R}_m)$ is zero when its arguments are outside the muffin-tin spheres, hence

$$\underline{\tau}^{nm} = \int_0^S \int_0^S |J(\mathbf{r}_n)\rangle \tau^{nm}(\mathbf{r}_n + \mathbf{R}_n, \mathbf{r}'_m + \mathbf{R}_m) \langle J(\mathbf{r}'_m)| d\mathbf{r}_n d\mathbf{r}'_m, \tag{1.156}$$

one can obtains for $\mathbf{r}_n$ and $\mathbf{r}'_m$ greater than S the following expression of the Green's function

$$\begin{aligned} G(\mathbf{r}_n + \mathbf{R}_n, \mathbf{r}'_m + \mathbf{R}_m) = & - E \left\langle H(\mathbf{r}_n) \left| \underline{\tau}^{nm} \right| H(\mathbf{r}'_m) \right\rangle \\ & + \langle J(\mathbf{r}_n)| \left[\underline{G}^{0,nm} + \sum_{i \neq n, j \neq m} \underline{G}^{0,ni} \underline{\tau}^{ij} \underline{G}^{0,jm} \right] |J(\mathbf{r}_m)\rangle \\ & - i\sqrt{E} \langle J(\mathbf{r}_n)| \left[\Theta(\mathbf{r}'_n - \mathbf{r}_n)\delta_{nm} + \sum_{i \neq n} \underline{G}^{0,ni} \underline{\tau}^{im} \right] |H(\mathbf{r}'_m)\rangle \\ & - i\sqrt{E} \langle J(\mathbf{r}_n)| \left[\Theta(\mathbf{r}_n - \mathbf{r}'_n)\delta_{nm} + \sum_{j \neq m} \underline{\tau}^{nj} \underline{G}^{0,jm} \right] |H(\mathbf{r}'_m)\rangle. \end{aligned} \tag{1.157}$$

Further, the manipulation in the equation of motion of the scattering path operator, Equation (1.152), yields useful quantities

$$\sum_{i \neq n} \underline{G}^{0,ni} \underline{\tau}^{im} = \underline{m}^n \underline{\tau}^{nm} - \delta_{nm} \tag{1.158}$$

$$\sum_{j \neq m} \underline{\tau}^{nj} \underline{G}^{0,jm} = \underline{\tau}^{nm} \underline{m}^m - \delta_{nm} \tag{1.159}$$

$$\underline{G}^{0,nm} + \sum_{i \neq n, j \neq m} \underline{G}^{0,ni} \underline{\tau}^{ij} \underline{G}^{0,jm} = \underline{m}^n \underline{\tau}^{nm} \underline{m}^m - \underline{m}^n \delta_{nm}, \tag{1.160}$$

where $\underline{m}^n = (\underline{t}^n)^{-1}$, with these considerations and using the relation $\Theta(r) - 1 = -\Theta(-r)$, one arrives at the final form of the Green's function written in terms of the scattering

solutions

$$\begin{aligned} G(\mathbf{r}_n + \mathbf{R}_n, \mathbf{r}'_m + \mathbf{R}_m) = &\langle Z^n(\mathbf{r}_n) \,|\underline{\tau}^{nm}|\, Z^n(\mathbf{r}'_m)\rangle \\ &- \delta_{nm}\left[\langle Z^n(\mathbf{r}_n)|J^n(\mathbf{r}'_n)\rangle\Theta(\mathbf{r}'_n - \mathbf{r}_n)\right. \\ &\left. + \langle J^n(\mathbf{r}_n)|Z^n(\mathbf{r}'_n)\rangle\Theta(\mathbf{r}_n - \mathbf{r}'_n)\right], \end{aligned} \tag{1.161}$$

with the regular and irregular functions being defined, respectively,

$$|Z^n(\mathbf{r})\rangle = \underline{m}^n|J(\mathbf{r})\rangle - i\sqrt{E}|H(\mathbf{r})\rangle \tag{1.162}$$

$$|J^n(\mathbf{r})\rangle = |J(\mathbf{r})\rangle. \tag{1.163}$$

So far, this expression of the Green's function has only been accessed by the arguments $\mathbf{r}_n$ and $\mathbf{r}'_m$ outside of muffin-tin spheres. However, it can also be valid on and inside the muffin-tins. This is because that the Green's function is an object that satisfies a second order differential equation in all space [38].

Chapter 2

Methods at Finite-Temperature

In principle, the generalization of DFT to include temperature-dependent effects is possible, and such an attempt was made earlier by Mermin (1956)[39]. However, for magnetism, Mermin's temperature-dependent DFT encounters obstacles in use due to the difficulties associated with the temperature-dependent exchange-correlation approximation [40]. In the adiabatic approximation, the Heisenberg model is an approach that works well in practice. It simply and accurately deals with magnetism at finite temperatures. In electronic transport, the study of real materials subjected to external fields is a non-equilibrium statistical problem. It is a task that is difficult to deal with using a complete microscopic theory. Alternatively, one can use the Boltzmann transport theory under the semi-classical approximation of electron dynamics. Under these assumptions (adiabatic and semiclassical), DFT provides the starting point and input parameters for temperature-dependent study.

2.1 Magnetism

2.1.1 Origins

Bohr and van Leeuwen show that the phenomena of magnetism in thermal equilibrium cannot be explained from classical approaches. It is found that all successful approaches are based on quantum mechanical descriptions. Magnetism is a quantum-statistical phenomenon that emerged from the interplay of the Coulomb interaction with the Fermionic nature of electrons. This can be understood from the Hartree-Fock approximation, where the exchange interaction only occurs for electrons of the same spin quantum number. Therefore the HF equations can be regarded as spin-dependent equations through spin-dependent potentials. The potential can be different for each spin projection, $\{\uparrow, \downarrow\}$,

leading to spin-imbalance for electron occupancy in some systems and thus producing a spontaneous magnetization[41, 42].

For more illustration, consider a system of two electrons interacting with each other by Coulomb repulsion, subjected to external potential given by hydrogen molecule. [43]. The system is characterized by two atomic orbitals, φ_A and φ_B, at a long distance between the hydrogen atoms. The spatial wave function can be approximated by a product of these two orbitals. The spin degree of freedom can be taken into account using the singlet and triplet spin functions for a system of two spin-1/2 particles. The wave function of the system is divided into two different wave functions, singlet and triplet, in order to respect the Pauli exclusion principle. The singlet is the product of the symmetric spatial wave function and the singlet spin function, while the triplet is the product of the antisymmetric spatial function (here the electrons avoid each other than in the symmetric case, thus reducing the Coulomb repulsion) and the triplet spin function. At the lowest energies, the Hamiltonian is diagonal in the singlet and triplet states. It directly gives two different energies, ϵ_s and ϵ_t. The energy ϵ_s corresponds to the single state with spin $S = 0$, while ϵ_t is associated with the triplet states of spin $S = 1$. Within the limit of small overlap between atomic orbitals,

$$\epsilon_t - \epsilon_s \simeq -2J, \tag{2.1}$$

where

$$J = \iint \varphi_A^*(\mathbf{r})\varphi_B^*(\mathbf{r}')\frac{1}{|\mathbf{r}-\mathbf{r}'|}\varphi_B(\mathbf{r})\varphi_A(\mathbf{r}')d\mathbf{r}d\mathbf{r}' \tag{2.2}$$

is the exchange energy. This approach was introduced by Heitler and London (1927) to describe the binding energy of the H_2-molecule. Depending on the overlap, the exchange integral can be positive or negative, determining the most stable spin configuration—triplet or singlet state. The exchange integral can always be positive if the orbitals are orthogonal, as for two electrons in the same atom. Hence the triplet state is the most favorable. This is the origin of Hund's first rule: Within an atom, electrons are distributed in the incompletely filled shell such that the spin multiplicity has the greatest value. It was noticed by Dirac and Heisenberg independently that both singlet and triplet energies are solutions of the following effective Hamiltonian

$$H_{eff} = \epsilon_s + \frac{1}{2}(\epsilon_t - \epsilon_s)\mathbf{S}^2. \tag{2.3}$$

Which acts only on the spin functions. This Hamiltonian can be reformulated to another form using the relation $(\mathbf{S}_1 + \mathbf{S}_2)^2 = \mathbf{S}_1^2 + \mathbf{S}_2^2 + 2\mathbf{S}_1\mathbf{S}_2$, with the fact that $\mathbf{S}_1^2 + \mathbf{S}_2^2 = \frac{3}{4} + \frac{3}{4}$

to obtain

$$H_{eff} = \epsilon_s - 2(\epsilon_t - \epsilon_s)(\mathbf{S}_1\mathbf{S}_2 + \frac{3}{4}) = \text{constant} - 2J\mathbf{S}_1\mathbf{S}_2. \tag{2.4}$$

In this form, the Hamiltonian is known as the Heisenberg model for a system with two spin moments. It indicates that the magnetic state is ferromagnetic (parallel spin) if J is positive, while antiferromagnetic (antiparallel) if J is negative.

In general, the magnetic moments of atoms or ions are the sum of their orbital and spin moments. It has been shown that for ferromagnetic transition metals and magnetic Heusler compounds, the orbital contribution associated with d electrons is almost zero because it is quenched by crystal field splitting. Thus only their spin moments can be survived [44]. The Heisenberg Hamiltonian can be generalized to a large number of spin moments centered on sites i and j by assuming a sum concerning all pair spin-interaction J_{ij} as:

$$H = -\sum_{ij} J_{ij}\mathbf{S}_i\mathbf{S}_j. \tag{2.5}$$

The exchange interaction in this description is called direct exchange because it is nonzero only if the overlap between orbitals exists. Direct exchange is the characteristic of systems with short interatomic distances. However, most magnetic materials have a large atomic separation which prevents such a mechanism from being possible. For ferromagnetic metals, the indirect exchange is the dominant mechanism, as conduction electrons play the role of mediator in the coupling of distant magnetic moments. This interaction is long-ranged and oscillates between ferromagnetic and antiferromagnetic coupling known as RKKY (Ruderman-Kittel-Kasuya- Yosida) interaction [45]. Another indirect exchange mechanism consists of the small covalent hybridization between the d states of local moments and the sp states of nonmagnetic atoms. Therefore, two local moments interact via hybridization through the intermediate nonmagnetic atoms, and the interaction is called superexchange [46]. This mechanism is usually characteristic of magnetic insulators and mostly leads to antiferromagnetic coupling between the magnetic moments.

2.1.2 Localized and itinerant picture

The Heisenberg model implies that the exchange interaction occurs between well-defined local atomic moments. In this localized picture, the magnetic moments are assumed to be integrals, and hence their origin is explained based on Hund's first rule. However, the observation of many magnetic materials such as Fe, Co and Ni ferromagnetic metals reveals that the magnetic moments are not integral multiples of the Bohr

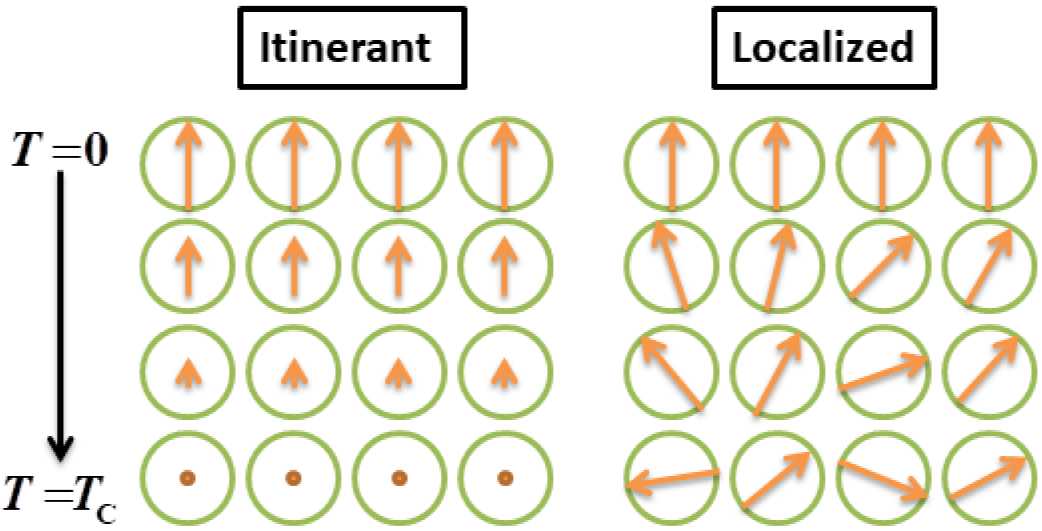

Figure 2.1: Comparison between Stoner and Heisenberg models.

magneto, but it takes any value. In solids, the atoms are influenced by their surrounding through the overlap of orbitals corresponding to their valence states. It results in an alteration of the magnetic state of atoms because the valence electrons—which are responsible to the magnetism—are itinerant and not localized at atomic sites. In this case, the electronic structure is an indispensable factor to describe the magnetism, at least in the ground state. One of the simplest approachs is the Stoner model. It predicts the ferromagnetic order in itinerant systems if the Stoner conduction

$$I\rho(E_{\mathrm{F}}) > 1 \tag{2.6}$$

is satisfied. The Stoner exchange parameter, I, is responsible for the spin splitting of the energy bands, and the density of states $\rho(E_{\mathrm{F}})$ is for the system in its nonmagnetic phase. It was found that the Stoner criterion is fulfilled for narrow-band systems such as Fe, Co and Ni transition metals. Their predicted magnetic moments are in fair agreement with experimental ones, if the Stoner theory is combined with realistic band-structure calculations [40]. Narrow bands are characteristic of d and f states. The d states, although they are itinerant, still have sufficient localized character around their atomic sites. This fact results in a high density of states at the Fermi level, which leads to high kinetic energy in the non-magnetic configuration. For avoiding the necessary energy penalty in the formation of the non-magnetic state, the system prefers the magnetic state through the exchange interaction mechanism. Therefore, Stoner's theory justifies why magnetism usually occurs for materials with d and f states.

Although Stoner's theory succeeded in describing magnetism at zero temperature, it failed at a finite temperature. In the Stoner picture, the spin fluctuation consists of the excitation of electrons from the spin-majority band to the spin-minority one, resulting in the creation of electron-hole pairs. This is called the longitudinal spin-fluctuation; with increasing temperature, the rate of the spin-flip excitations across the stoner gap increases, causing the gradual decrease of the magnetic moments until they finally vanish at T_{C}, as illustrated in Figure 2.1. Because the energy required for the Stoner excitation is of the order of the exchange splitting, the expected T_{C} is very high. Indeed, the Stoner calculation of T_{C} for ferromagnetic transition metals shows much higher values than the experimental ones [40]. In contrast, the transversal spin-fluctuations necessitate excitations of low energies, represented by spin waves arising as natural excitation in the Heisenberg model. In this context, what cannot be described by one of the two models is easily accounted for by the other model. Because spin dynamics of many ferromagnetic transition metals can decouple (adiabatic approximation) from the motion of electrons, the Heisenberg model describes the temperature-dependent magnetic properties of these materials very well. [47]

2.1.3 Mean-field approximation

In this thesis, We adopt the Heisenberg local moment picture to describe magnetic systems at finite temperatures. The starting point is following Hamiltonian

$$H = -\sum_{ij} J_{ij}\mathbf{S}_i\mathbf{S}_j - g\mu_{\mathrm{B}}B\sum_i S_i^z, \tag{2.7}$$

where in addition to the Heisenberg Hamiltonian, we added the Zeeman term to describe systems of interacting spin subject to a uniform external magnetic field B (assumed to be pointing in the z-direction). The numerical constant $g = 2$ is the g-factor of the electron. In general, one cannot exactly solve the statistical problem associated with this Hamiltonian. The mean-field approximation is the simplest way to deal with this problem. The approach is based on the simple idea that the interaction of each particular spin with all others is replaced by a mean-field one independent of each sites. The procedure is to write $\mathbf{S}_i = \langle\mathbf{S}_i\rangle + \delta\mathbf{S}_i$, where $\delta\mathbf{S}_i = \mathbf{S}_i - \langle\mathbf{S}_i\rangle$ are the fluctuations. At first-order in

fluctuation, ($\delta\mathbf{S}_i\delta\mathbf{S}_j = 0$), the product of the spins is given by

$$\begin{aligned}\mathbf{S}_i\mathbf{S}_j &= \Big(\langle\mathbf{S}_i\rangle + \delta\mathbf{S}_i\Big)\Big(\langle\mathbf{S}_j\rangle + \delta\mathbf{S}_j\Big) \\ &= \langle\mathbf{S}_i\rangle\langle\mathbf{S}_j\rangle + \langle\mathbf{S}_i\rangle\delta\mathbf{S}_j + \delta\mathbf{S}_i\langle\mathbf{S}_j\rangle \\ &= -\langle\mathbf{S}\rangle^2 + \langle\mathbf{S}\rangle\Big(\mathbf{S}_i + \mathbf{S}_i\Big),\end{aligned} \tag{2.8}$$

where we have assumed $\langle\mathbf{S}_i\rangle = \langle\mathbf{S}_j\rangle = \langle\mathbf{S}\rangle$. In the ferromagnetic state where all spin point in z-direction the Hamiltonian with this spin product reads

$$\begin{aligned}H &= -\sum_i\Big(g\mu_{\mathrm{B}}B + 2\langle S\rangle\sum_j J_{ij}\Big)S_i^z + \sum_i\langle S\rangle^2\sum_j J_{ij} \\ &= -\sum_i\Big(g\mu_{\mathrm{B}}B + 2\langle S\rangle J_i\Big)S_i^z + \sum_i\langle S\rangle^2 J_i \\ &= \sum_i\Big(-g\mu_{\mathrm{B}}B_{eff}S_i^z + \langle S\rangle^2 J_0\Big),\end{aligned} \tag{2.9}$$

with $B_{eff} = B + \frac{2J_0}{g\mu_{\mathrm{B}}}\langle S\rangle$. We have used periodic boundary conditions (satisfied for bulk systems), $J_i = J_j = J_0$, with $J_0 = \sum_i J_{0i}$ is called the onsite exchange interaction. The problem of interacting spins is reduced via the mean-filed approach into effective paramagnetic (independent spins) one subject to the effective magnetic field B_{eff}. The effective field (also known as the Weiss field) must be determined in a self-consistent manner because it depends on the solution to the problem, that is the quantity $\langle S\rangle$. The magnetic properties at a finite temperature of a paramagnetic system are determined easily using the partition function of Boltzmann statistic $Z = (Z_\alpha)^N$, where Z_α is the partition function of a single atom written as

$$\begin{aligned}Z_\alpha = \sum_n e^{-\beta E_n} &= \sum_{m=-S}^{S} e^{-\beta\langle S\rangle J_0}e^{-\beta|g|\mu_{\mathrm{B}}B_{eff}m} \\ &= \sum_{m=-S}^{S} aq^m \\ &= aq^{-S}\sum_{i=1}^{2S+1} q^{i-1},\end{aligned} \tag{2.10}$$

with $\beta = \frac{1}{k_{\mathrm{B}}T}$ and the abbreviations $a = e^{-\beta\langle S\rangle J_0}$ and $q = e^{-\beta|g|\mu_{\mathrm{B}}B_{eff}}$ are used. Evaluating the sum of the geometrical series, the last line of the above equation directly yields

$$a\left(\frac{q^{-(S+\frac{1}{2})} - q^{S+\frac{1}{2}}}{q^{-\frac{1}{2}} - q^{\frac{1}{2}}}\right), \tag{2.11}$$

and hence

$$Z_\alpha = e^{-\beta\langle S\rangle J_0}\frac{\sinh\left[\beta|g|\mu_{\mathrm{B}}B_{eff}\left(S+\frac{1}{2}\right)\right]}{\sinh\left[\frac{\beta|g|\mu_{\mathrm{B}}B_{eff}}{2}\right]}. \tag{2.12}$$

The average spin $\langle S\rangle$ along the direction of the effective field can be reads

$$\begin{aligned}\frac{\langle S\rangle}{S} &= (SZ_\alpha)^{-1}\sum_{m=-S}^{S} me^{-\beta|g|\mu_{\mathrm{B}}B_{eff}m} \\ &= -\frac{1}{|g|\mu_{\mathrm{B}}\beta S}\frac{\partial\log(Z_\alpha)}{\partial B_{eff}} \\ &= \mathrm{B}_S(\beta|g|\mu_{\mathrm{B}}B_{eff}S),\end{aligned} \tag{2.13}$$

where $\mathrm{B}_S(x)$ is known as the Brillouin function, given by

$$\mathrm{B}_S(x) = \frac{2S+1}{2S}\coth\left(\frac{2S+1}{2S}x\right) - \frac{1}{2S}\coth\left(\frac{1}{2S}x\right). \tag{2.14}$$

One can reformulate Equation (2.13) to an appropriate form. Without an applied field we can write

$$x = \frac{|g|\mu_{\mathrm{B}}SB_{eff}}{k_{\mathrm{B}}T} \tag{2.15}$$

$$\begin{aligned}&= -\frac{2J_0S^2}{k_{\mathrm{B}}T}\frac{\langle S\rangle}{S}, \\ &\Rightarrow \frac{k_{\mathrm{B}}T}{2J_0S^2}x = \mathrm{B}_S(x).\end{aligned} \tag{2.16}$$

We can solve the last self-consistent equation graphically by plotting separately the functions located on the left- and the right-hand side. The intersections between the straight lines on the left-hand side of the Equation (2.16) and the Brillouin function determine the solutions, which correspond to the average magnetic moments (see Figure 2.2) [43].

From Figure 2.2, one can identify two distinct regions separated by a straight line that corresponds to a specific critical temperature (Curie temperature). The region above the Curie temperature indicates an intersection associated with zero magnetization: the intersection occurs at $x = 0$ and hence $\langle S\rangle = 0$. The same solution survives below T_{C}, but it cannot be stable because it leads to a maximum in the free energy. However, within this temperature range, there exists another solution corresponding to finite magnetization

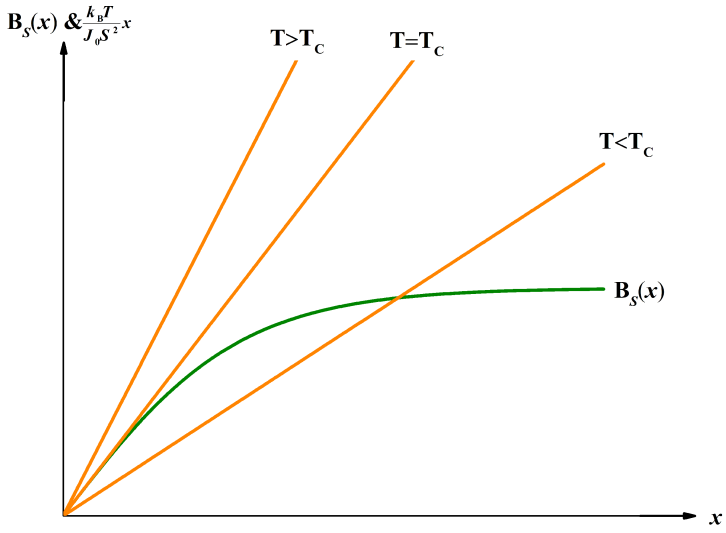

Figure 2.2: Graphical illustration of the intersection between the Brillouin function and straight lines of the temperature-dependent slopes.

whose free energy is lower. Mathematically, the Curie temperature is obtained by equating the slope of both functions of Equation (2.16) at $x = 0$

$$\frac{k_B T_C}{2 J_0 S^2} = \left.\frac{d B_S(x)}{dx}\right|_{x=0} \tag{2.17}$$

$$= \frac{S+1}{3S},$$

$$\Rightarrow T_C = \frac{2}{3k_B} J_0 S(S+1). \tag{2.18}$$

In the case when the spins can be considered as classical vectors ($S \to \infty$), the Brillouin function reduces to the Langevin function, and the critical temperature is given by

$$T_C = \frac{2}{3k_B} J_0 S^2. \tag{2.19}$$

In the mean-field approach, the fluctuations of the spins around their mean value should be negligible for a better description. For long-range exchange interaction, the fluctuations play a minimal role in materials characterized by the crystalline structure of high coordination number (the nearest neighbor of each spin), such as the fcc structure.

The mean-field approach can be generalized to multi-sublattice systems starting from the classical limit of the Heisenberg Hamiltonian [48]

$$H = -\sum_{\mu \neq \nu} \sum_{\mathbf{R} \neq \mathbf{R}'} J^{\mu\nu}_{\mathbf{R}\mathbf{R}'} \mathbf{e}^{\mu}_{\mathbf{R}} \mathbf{e}^{\nu}_{\mathbf{R}'}, \tag{2.20}$$

where μ and ν denote the sublattices, $\mathbf{R}$ and $\mathbf{R}'$ are lattice vectors specifying the magnetic atoms within the sublattices. The unite vector $\mathbf{e}^{\mu}_{\mathbf{R}}$ points in the direction of the corresponding magnetic moment specified by $\mathbf{R}$ in sublattice μ. Here, the exchange pair parameter $J^{\mu\nu}_{\mathbf{R}\mathbf{R}'}$ is defined to incorporate the product $S^{\mu}S^{\nu}$. Directly, the Curie temperature of the multi-sublattice system is obtained by solving the following coupled equations

$$\frac{3}{2}k_{\mathrm{B}}T_{\mathrm{C}}\left\langle \mathbf{e}^{\mu}\right\rangle = \sum_{\nu} J_{0}^{\mu\nu}\left\langle \mathbf{e}^{\nu}\right\rangle, \tag{2.21}$$

With

$$J_{0}^{\mu\nu} = \sum_{\mathbf{R}\neq 0} J_{0\mathbf{R}}^{\mu\nu}. \tag{2.22}$$

$\langle \mathbf{e} \rangle$ is the average z-component of the vector $\mathbf{e}$. One can formulate the above-coupled equations as an eigenvalue matrix problem

$$(\mathbf{J} - \epsilon\mathbf{I})\mathbf{E} = \mathbf{0}. \tag{2.23}$$

With $\epsilon = \frac{3k_{\mathrm{B}}T}{2}$, $\mathbf{J}$ is a matrix of $J_0^{\mu\nu}$, $\mathbf{I}$ is a unit matrix and E is a vector of $\langle e^{\mu} \rangle$. The largest eigenvalue of $\mathbf{J}$ gives the value of the Curie temperature[49, 50].

2.1.4 Exchange interaction from first-principles

There are two commonly used approaches to evaluate the exchange interactions from *ab initio* calculations. In all of them, the complex itinerant magnets described by the first principles in the framework of DFT are mapped onto the Heisenberg Hamiltonian. This procedure relays on the adiabatic assumption that the motion related to transverse excitation (spin waves) is much slower than the motion associated with the hopping of electrons (involving Stoner transitions) [51]. One can ensure this in systems characterized by magnetic atoms with large exchange splitting, *e.g.*, Mn atoms, implying the presence of a well-defined local magnetic moment, with a good approximation, is almost insensitive to any arbitrary rotations in its magnitude.

Based on this fact multiscale study is introduced for modeling magnetic materials[52]. The first approach for determining the exchange parameters works in reciprocal space, called the frozen-magnon approach. The scheme consists of the calculation of the total energies $E(\mathbf{q})$ of the constrained spin-spiral configurations characterized by reciprocal wave vectors $\mathbf{q}$ [53, 54, 55, 56, 57]. The exchange coupling parameters are retrieved by performing a back-Fourier transformation of those defined in reciprocal space. The latter are extracted from the solution of a system of coupled equations.

In contrast, the second approach performs differently, where one can directly obtain the exchange parameters by a real-space scheme [58]. This method is based on the magnetic force theorem. The total energy difference related to infinitesimal rotations can be directly approximated by the band energy difference of the ground states of a collinear spin structure [59, 60]. Accordingly, in the context of the multiple scattering theory, the energy change caused by an infinitesimal perturbation of the angle between two magnetic moments is calculated using Lloyd's formula [61]. Therefore, an expression of the pair exchange parameters can be written as a function of the scattering parameters

$$J_{ij} = -\frac{1}{4\pi}\Im \int^{E_{\mathrm{F}}} \mathrm{Tr}\left(t_{i\uparrow}^{-1} - t_{i\downarrow}^{-1}\right)\tau_{\uparrow}^{ij}\left(t_{j\uparrow}^{-1} - t_{j\downarrow}^{-1}\right)\tau_{\downarrow}^{ji} dE, \tag{2.24}$$

with t is the single-site matrix and τ is the scattering path operator. The arrows indicate the spin projection along the quantization axis (*e.g.*, z-direction). This formalism is implemented in the SPRKKR program [29, 62], and we will use it to determine the pair exchange interactions of Heusler compounds.

2.2 Thermoelectric

2.2.1 Semiclassical electrons dynamic

In the Drude model of the free electron system, the motion of electrons between two collisions is described using simply the classical equations of motion. In quantum mechanics, the same equations appear if we consider the dynamics of the electron wave packets. The wave packets are constructed by a superposition of plane waves. The generalization to systems of an arbitrary periodic potential is given by the semiclassical approach. In this framework, the wave packet is a superposition of the stationary Bloch waves $\psi_{n\mathbf{k}}(\mathbf{r})$ with energies $\epsilon_n(\mathbf{k})$ that lie in the same band

$$W_{n\mathbf{k}}(\mathbf{r}, t) = \sum_{\mathbf{k}'} w(\mathbf{k}')\psi_{n\mathbf{k}'}(\mathbf{r})e^{-i\frac{\epsilon_n(\mathbf{k}')t}{\hbar}}, \tag{2.25}$$

with $w(\mathbf{k}') \approx 0$ for $|\mathbf{k} - \mathbf{k}'| > \Delta k$. This wave packet is assumed to be characterized by a wave vector $\mathbf{k}$ if Δk is much smaller than the size of the Brillouin zone $\Delta k \ll \frac{1}{a}$, where a is the lattice constant. Hence, from the limitation imposed by the Heisenberg uncertainty principle $\Delta r \Delta k \approx 1$, the wave packet spreads over many unit cells $\Delta r \gg a$.

Under the assumption of slowly varying applied electric $\mathbf{E}(\mathbf{r}, t)$ and magnetic $\mathbf{B}(\mathbf{r}, t)$ fields over the characteristic size of the wave packet, the evolution of the centers of mass

$(\mathbf{r}, \mathbf{k})$ of this packet is described by the following semiclassical equations

$$\frac{d\mathbf{r}}{dt} = \mathbf{v}_n(\mathbf{k}) \tag{2.26}$$
$$= \frac{1}{\hbar}\frac{\partial \epsilon_n(\mathbf{k})}{\partial \mathbf{k}},$$
$$\hbar\frac{d\mathbf{k}}{dt} = -e\left[\mathbf{E}(\mathbf{r}, t) + \frac{1}{c}\mathbf{v}_n(\mathbf{k}) \wedge \mathbf{B}(\mathbf{r}, t)\right], \tag{2.27}$$

with $\mathbf{v}_n(\mathbf{k})$ is the average velocity of Bloch electrons interpreted as the group velocity of the wave packet, and e is the positive elementary charge. The rate of change of $\hbar\mathbf{k}$ is equal to the external forces. In contrast to the free-electron system, the quantity, $\hbar\mathbf{k}$, is called crystal momentum rather than electron momentum because it is not the eigenvalue of the momentum operator acting on the Bloch states. The validity of the semiclassical approximation relays on the assumption that electrons must stay in a given band. Therefore, the magnitude of the applied forces should not be large so that there is no transition between the bands [63, 64]. In the semi-classical model, one can treat classically the applied forces. However, due to variation of the periodic potential over distances smaller than the wave packet size, the effect of the crystal is included quantum mechanically through the band dispersion.

Among the consequences of the semi-classical model is that filled bands are inert, *i.e.*, only electrons in the unfilled band are subject to electric current. Moreover, the semiclassical description allows the introduction of the concept of holes which is practical for interpreting some transport properties.

2.2.2 Boltzmann transport theory

Applying a uniform electric field or temperature gradient to metals permits conduction electrons to respond as a direct electric current. The system thus changes from the thermal equilibrium state described by the Fermi-Dirac distribution

$$f(\mathbf{k}) = \frac{1}{e^{\left[\frac{\epsilon(\mathbf{k})-\mu}{k_{\mathrm{B}}T}\right]} + 1}, \tag{2.28}$$

where μ is the chemical potential, to the non-equilibrium distribution function $g(\mathbf{r}, \mathbf{k}, t)$. The latter function is defined so that the number of electrons in phase-space volume element around the point $(\mathbf{r}, \mathbf{k})$ at time t is

$$2g(\mathbf{r}, \mathbf{k}, t)\frac{d\mathbf{r}d\mathbf{k}}{(2\pi)^3}. \tag{2.29}$$

In the absence of collisions, this quantity remains conserved with time evolution

$$2g(\mathbf{r},\mathbf{k},t)\frac{d\mathbf{r}d\mathbf{k}}{(2\pi)^3} = 2g(\mathbf{r}+\dot{\mathbf{r}}t,\mathbf{k}+\dot{\mathbf{k}}t,t+dt)\frac{d\mathbf{r}'d\mathbf{k}'}{(2\pi)^3}, \tag{2.30}$$

with $\mathbf{r}' = \mathbf{r}+\dot{\mathbf{r}}t$ and $\mathbf{k}' = \mathbf{k}+\dot{\mathbf{k}}t$, where the point indicates the time derivative. Liouville's theorem states that the phase-space volume element remains unchanged during the motion, $d\mathbf{r}d\mathbf{k} = d\mathbf{r}'d\mathbf{k}'$, which allows writing

$$g(\mathbf{r},\mathbf{k},t) = g(\mathbf{r}+\dot{\mathbf{r}}t,\mathbf{k}+\dot{\mathbf{k}}t,t+dt). \tag{2.31}$$

Expanding to first order the right-hand side and dividing all by dt, yields

$$\frac{dg}{dt} = \frac{\partial g}{\partial t} + \dot{\mathbf{r}}\frac{\partial g}{\partial \mathbf{r}} + \dot{\mathbf{k}}\frac{\partial g}{\partial \mathbf{k}} = 0, \tag{2.32}$$

which represents the continuity equation in phase-space, and remains valid as long as the collision process is absent during the motion. However, in solids, the collisions stem from various sources of scattering, such as impurities and phonons. The transport equation, Equation (2.32), can include these collisions by adding a collision term, $\left(\frac{\partial g}{\partial t}\right)_{coll}$, to its right-hand side. Proceeding from the observation that collisions in a shorter time (the relaxation time τ) restore the state of equilibrium after removing the applied force, the collision term can be approximated by

$$\left(\frac{\partial g(\mathbf{r},\mathbf{k},t)}{\partial t}\right)_{coll} = -\frac{g(\mathbf{r},\mathbf{k},t)-f(\mathbf{r},\mathbf{k})}{\tau}, \tag{2.33}$$

where $f(\mathbf{r},\mathbf{k})$ is a local equilibrium Fermi-Dirac function, depends on vector r through temperature and chemical potential. This approach is the simplest approximation known as the relaxation time approximation. The corresponding semiclassical Boltzmann equation is

$$\frac{\partial g}{\partial t} + \mathbf{v}_n(\mathbf{k})\frac{\partial g}{\partial \mathbf{r}} - \frac{e}{\hbar}\mathbf{E}\frac{\partial g}{\partial \mathbf{k}} = \frac{g-f}{\tau}, \tag{2.34}$$

employing the semiclassical equations $\dot{\mathbf{r}} = \mathbf{v}_n(\mathbf{k})$ and $\hbar\dot{\mathbf{k}} = -e\mathbf{E}$. The Boltzmann equation in the relaxation time approximation, Equation (2.34), admits a solution with rather general aspects. In some aspects, a simplification is possible for calculating more simply the transport properties. Accordingly, in the limit of slow semiclassical dynamics over the moments of the order of τ, the non-equilibrium distribution function is given [64]

$$g_n = f_n + \tau\mathbf{v}_n(\mathbf{k})\left(-\frac{\partial f}{\partial \epsilon}\right)\left[-e\mathbf{G} - \frac{\epsilon(\mathbf{k})-\mu}{T}(\nabla T)\right], \tag{2.35}$$

with $\mathbf{G} = \mathbf{E} + \frac{\nabla\mu}{e}$ is the electrochemical potential. One can define the electric current as

$$\mathbf{j} = -2e \sum_n \int \frac{d\mathbf{k}}{(2\pi)^3} \mathbf{v}_n(\mathbf{k}) g, \tag{2.36}$$

where the factor, 2, is set to account for spin degeneracy. The first term on the right-hand side of Equation (2.35) does not contribute to the current because no current can exist in the equilibrium state. Thus, after integration, the electrical current is given as a linear response to external forces as

$$\mathbf{j} = \mathcal{L}^{(0)}\mathbf{G} + \frac{\mathcal{L}^{(1)}}{eT}\left(-\nabla T\right), \tag{2.37}$$

with

$$\mathcal{L}^{(\nu)} = e^2 \int \sigma(\epsilon)(\epsilon - \mu)^\nu \left(-\frac{\partial f}{\partial \epsilon}\right) d\epsilon \tag{2.38}$$

is called the generalized transport coefficients and the the tensor $\sigma(\epsilon)$ is defined as

$$\sigma(\epsilon) = \sum_n \int \frac{d\mathbf{k}}{4\pi^3} \tau\left(\epsilon(\mathbf{k})\right) \mathbf{v}_n(\mathbf{k}) \otimes \mathbf{v}_n(\mathbf{k}) \delta\left(\epsilon - \epsilon(\mathbf{k})\right). \tag{2.39}$$

The electric current results from applying the electric (electrochemical) field and/or a temperature gradient. The effect produced by the latter is called the Seebeck effect. For cubic systems, the transport properties are isotropic, and thus the transport coefficient tensors reduce to scalar quantities. The electrical conductivity $\sigma(T) = \frac{j}{E}$ and the Seebeck coefficient $S(T) = \frac{G}{\nabla T}$ write in terms of the generalized transport coefficients as

$$\sigma(T) = \mathcal{L}^{(0)} \tag{2.40}$$

$$S(T) = \frac{1}{eT}\frac{\mathcal{L}^{1)}}{\mathcal{L}^{(0)}}. \tag{2.41}$$

One can define the Seebeck coefficient as the fact that the application of a temperature gradient induces charge accumulation at the boundary of the sample, thus the creation of an electrochemical potential difference (voltage), as seen in Figure 2.3. The Seebeck effect can be exploited in thermelectrics to harness energy out of heat waste.

The above formalism is implemented in the BoltzTraP code, which allows us to determine the transport properties from the first-principles band structure calculations using the interpolation scheme [65].

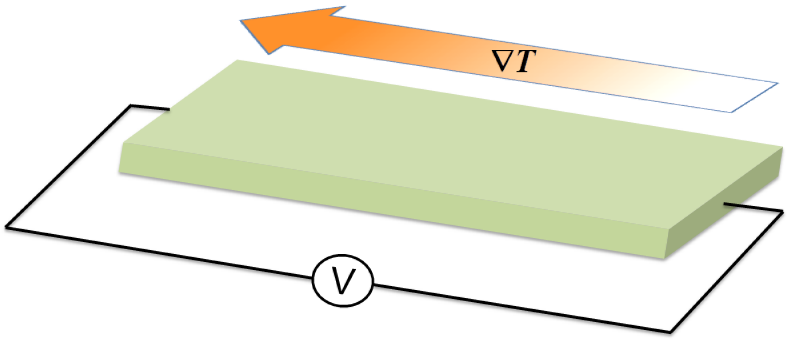

Figure 2.3: Schematic illustration of the generation of the electrical voltage (charge accumulation at the boundaries of a sample) using a temperature gradient.

2.2.3 Two-current model

In magnets, exchange splitting lifts spin degeneracy, and this has a strong effect on electronic transport. Therefore, the charge current in ferromagnets depends on the spin orientation, producing a spin polarization. In fact, the two spin channels are dependent due to the spin-flip scattering. This mechanism mixes the two spin channels by some interactions such as spin-orbit coupling. In the two-current model, one can ignore the spin-flip scattering assuming that spin-up and spin-down carriers form two different conductors, each with its own resistance. [66]. The total electrical current is then given as a sum of the current of the two spin channels

$$\mathbf{j} = \mathbf{j}_\uparrow + \mathbf{j}_\downarrow, \tag{2.42}$$

where

$$\mathbf{j}_\sigma = -e \sum_n \int \frac{d\mathbf{k}}{(2\pi)^3} \mathbf{v}^\sigma(\mathbf{k}) g_\sigma \tag{2.43}$$

is spin-dependent through spin-resolved band dispersion $\epsilon_{n\sigma}(\mathbf{k})$. Further manipulations yields

$$\sigma = \sigma_\uparrow + \sigma_\downarrow \tag{2.44}$$

$$S = \frac{S_\uparrow \sigma_\uparrow + S_\downarrow \sigma_\downarrow}{\sigma_\uparrow + \sigma_\downarrow}. \tag{2.45}$$

The electrical conductivity is a sum of conductivities from both spin directions. However, it is not the same for the Seebeck coefficient but it is an average of that of the two spin channels weighted by the corresponding conductivities. The two-current model well describes the transport properties of layered structures. It can also be applied, with good approximation, to study bulk magnets with non-heavy elements and high Curie temperature.

Part II

Fundamentals of Heusler Compounds

Chapter 3

Heusler Compounds

3.1 Introduction

Heusler compounds were discovered by Fritz Heusler in 1903 with his discovery of ferromagnetism in the new Cu_2MnZ compounds (Z are *sp* elements), although none of the constituent elements of this compounds are ferromagnetic. Subsequently, these class of compounds was named after its discoverer. The Heusler family of compounds is characterized by its large class containing more than 1000 compounds. They aroused enormous interest after discovering half-metallic ferromagnetism in half-Heusler NiMnSb in 1983. After that many properties, almost all kinds of magnetism, thermoelectric, superconductivity and topological insulator were found among the family of Heusler compounds.

This chapter gives a theoretical overview of Heusler compounds for their structural, electronic and magnetic properties.

3.2 Structural properties

The crystal structure of the full-Heusler compounds with the general formula X_2YZ (where X and Y are usually transition-metal elements and Z is one of the main group elements, see Figure 3.1) consists of four interpenetrating fcc sublattices denoted A, B, C and D with coordinates $(0, 0, 0)$, $(1/4, 1/4, 14)$, $(2/4, 2/4, 2/4)$ and $(3/4, 3/4, 3/4)$ respectively. There exist two different arrangements of atoms in Heusler compounds: In the $L2_1$ structure (space group no. 225: $Fm\overline{3}m$), the prototype is Cu_2MnAl, the two X elements equally occupy the A and C sublattices, while B and D host the Y and Z atoms, respectively. However, It is observed that Heusler compounds rather crystallize in the XA structure (space group no. 216: $F\overline{4}3m$), the prototype Hg_2TiCu when the

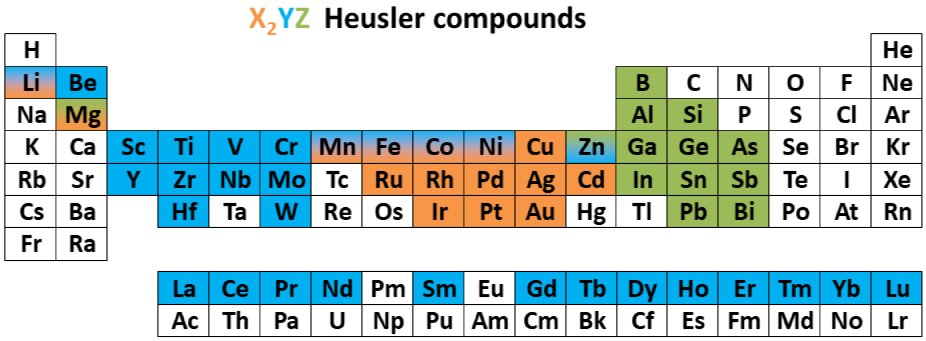

Figure 3.1: As the periodic table shows, the Heusler compounds are a large family because the formation of many combinations is possible [67].

valence of X is smaller than that of the Y. In this structure, the X atom at the C sublattice interchanged with the Y atom at the B sublattice. The structure is referred to half-Heusler ($C1_b$ structure, space group no. 216: $F\bar{4}3m$) if one of the transition-metal sublattices is vacant. Both XA and $C1_b$ structures have no inversion symmetry.

In the literature, it is well known that many Mn_2-based Heusler compounds prefer to crystallize in the tetragonal structure [68, 69]. There is two variant tetragonal structure in Heusler compounds. The one with space group 139 is derived from the cubic $L2_1$ structure by lattice distortion with an increasing or decreasing c/a_t ratio. The out-of-plane lattice parameter c and the in-plane parameter a_t are defined for cubic structures by $c = a$ and $a_t = a/\sqrt{2}$, with a being the lattice parameter of the cubic lattice. Therefore, for cubic structures, the c/a_t ratio is equal to $\sqrt{2}$, and any deviation from this value results in distortion of the cubic lattice into the tetragonal structure. Equivalently, the other tetragonal structure has the space group 119. It is a tetragonal distortion by increasing or decreasing the c/a_t ratio of the XA structure, see Figure 3.2.

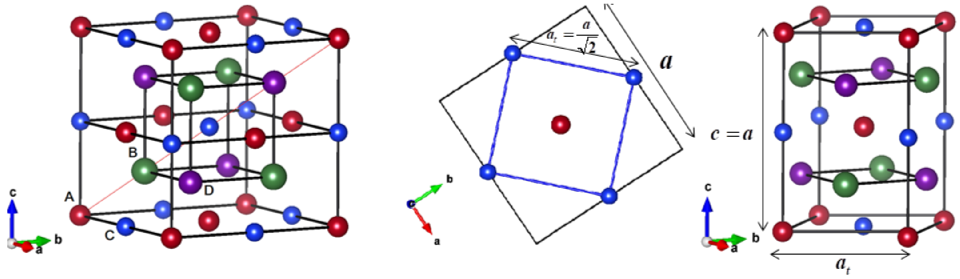

Figure 3.2: Structure of Heusler compounds: Cubic structure (left panel) and tetragonal structure (right panel).

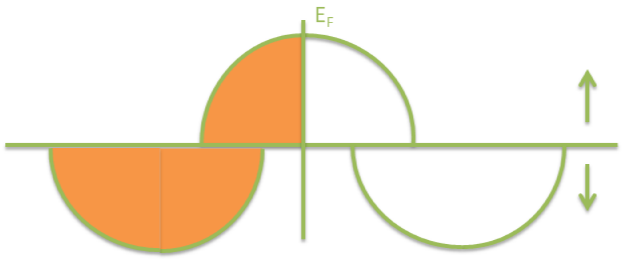

Figure 3.3: A schematic illustration of the DOS that is characteristic of HM compounds.

3.3 Electronic structure and magnetic properties

3.3.1 Half-metallic ferromagnet

Heusler compounds are considered the potential candidates to be half-metallic magnets. Half-metallic materials are compounds that exhibit a metallic state for one spin direction while having a semiconductor nature for the opposite one. Consequently, in terms of the density of states (DOS), the compounds are fully spin-polarized ($P = 100\%$) at the Fermi level. This can be seen with the help of Figure 3.3, with the definition of the spin polarization

$$P = \frac{N_\uparrow - N_\downarrow}{N_\uparrow + N_\downarrow} = 100\%, \tag{3.1}$$

where N is the state density at the Fermi level, and the arrows indicate the spin directions. As a result, the electric currents are almost totally from one spin direction if the compounds are half-metals with high Curie temperatures. Calculating electronic structure from the first principles is the easiest way to deal with the half-metallic nature of materials [70]. In this respect, Heusler alloys have been of particular interest since the advent of the concept of half-metallic ferromagnetism in the half-Heusler compound NiMnSb. For example, Table 3.1 summarizes half-metallic or nearly half-metallic Heusler compounds with their magnetic properties.

- **Electronic structure of the gapped channel**

  The electronic structure of the half-metallic Heusler compounds is intimately connected to their crystal structures—whether the structure is half- or full-Heusler. The half-metallic ferromagnet differs from the ordinary ferromagnetic metal in that its minority bands show a semiconductor character, where the Fermi level instead of crossing the bands (metallic channel) falls in the gap (gapped channel). The

Table 3.1: Magnetic properties of some magnetic Heusler compounds [71].

Structure	**Compound**	**Magnetic moment** (μ_B)	**Magnetic state**	$\mathbf{T_C}$(K)
$C1_b$	NiMnSb	4	FM	730
	CoMnSb	2.96	FM	490
$L2_1$	Co_2TiAl	1	FM	
	Co_2TiGa	1	FM	
	Co_2TiSi	2	FM	380
	Co_2TiGe	2	FM	380
	Co_2TiSn	2	FM	355
	Co_2VSi	2.9	FM	
	Co_2VGe	3	FM	
	Co_2VSn	3	FM	
	Co_2CrAl		FM	330
	Co_2CrGa	2.99	FM	495
	Co_2FeSi	5.9	FM	1100
	Co_2FeGe		FM	
	Co_2FeAl	4.5	FM	1170
	Co_2FeGa		FM	
	Co_2MnSi	4.94	FM	985
	Co_2MnGe	5	FM	905
	Co_2MnSn	4.98	FM	829
	Co_2MnAl	3.97	FM	693
XA	Mn_2VAl	2	FiM	768
	Mn_2CoAl	2	FiM	720
	Mn_2CoGa	2	FiM	740
	Mn_2CoIn	1.95	FiM	
	Mn_2CoSi	2.99	FiM	
	Mn_2CoGe	2.99	FiM	
	Mn_2CoSn	2.99	FiM	
	Mn_2CoSb	3.99	FiM	

bands of this gapped channel have different origins between half- and full-Heusler compounds. As an illustration, we take the NiMnSb as the prototype of the half-

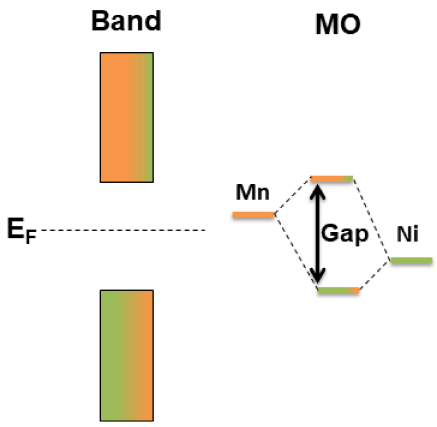

Figure 3.4: Molecular orbital (right panel) and band diagram (Left panel) representation of the NiMnSb compound.

Heusler alloys. At the Fermi level, the energy gap locates in-between the bonding and antibonding bands, formed primarily by the covalent hybridization between the Mn d states and Ni d states [72]. The schematic molecular orbital for the hybridization of the transition-metal atoms is sketched in Figure 3.4. In the gapped channel, the formation of the bonding bands has a significant contribution from the Ni atom, leaving the antibonding bands to be formed mainly from the Mn atom. This can be explained by the electronegativity difference where the high-valent Ni d states are lower in energy and the low-valent Mn d states are higher in energy. Therefore, the bonding states have mainly their weight at the Ni site while the antibonding at the Mn atom, as seen in the schematic molecular orbital depicted in Figure 3.4. The Sb atom serves to accommodate the effective charge coming from the transition metals because its sp bands are effectively deep-lying in energy [72]. The existence of a band gap in one of the spin-bands has been shown to contribute to the structural stability of half-Heusler compounds [73].

The situation becomes quite complex in the case of the full-Heusler structure where the vacuum site is occupied by another transition metal. Galanakis *et al* [74]., have explained based on the symmetry argument, the origin of the energy gap of full-Heusler compounds such as the Co_2-based Heusler compounds (crystallizing in the $L2_1$ structure). The possible hybridization between the atoms is schematically sketched in Figure 3.5. First, the Co d states hybridize with each other to form the bonding and antibonding states. Then, the resulting bonding states hybridize with the Mn d states to form new bonding and antibonding states separated by a significant hybridization gap [74]. The remaining antibonding states of the Co atoms do not hybridize with the Mn d states, and thus they are localized mainly at Co sites. Therefore, The Fermi level falls in the small gap formed in between t_{1u}

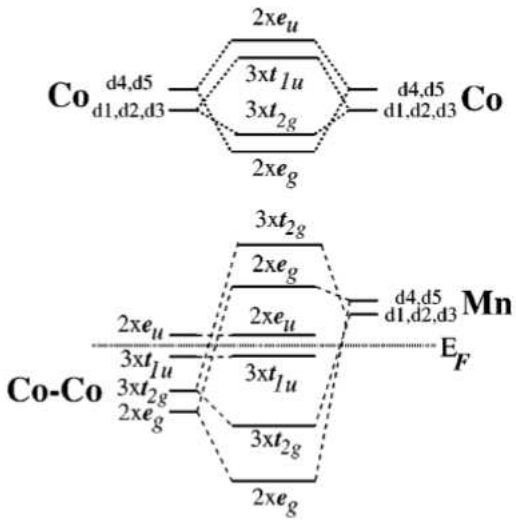

Figure 3.5: Possible hybridization responsible for the gap formation in half-metallic full-Heusler compounds [74].

and e_u nonbonding states. The actual gap width is small compared to the covalent one, and the interplay between the crystal field and the hybridization splitting of the Co d states can determine its value. If the half-metallic gap in the $L2_1$ structure contributes to the structural stability, the hybridization gap between the X-X and Y d states should be sufficiently wider. This may be ensured by a large difference in electronegativity between the X and Y atoms.

Similarly, for inverse full-Heusler compounds, the origin of the half-metallic gap is explained by the same arguments used for the regular Heusler structure. The transition metal in the B site hybridizes with the bonding states of the X(A)-Y. The half-metallic gap locates in-between the antibonding states of the X(A)-Y atoms (non-bonding to X(B))[75].

- **Slater-Pauling rule: The integer spin magnetic moment**

  In band-structure theory, the spin magnetic moment m per unit cell is defined as the difference in the number of valence electrons N between majority-spin and minority-spin bands

$$\begin{aligned} m &= (N_\uparrow - N_\downarrow)\,\mu_\mathrm{B} \\ &= (N - 2N_\downarrow)\,\mu_\mathrm{B}. \end{aligned} \tag{3.2}$$

  As a consequence, Heusler compounds with half-metallicity show integer spin magnetic moments. In many Heusler alloys, the total magnetic moment can be tuned

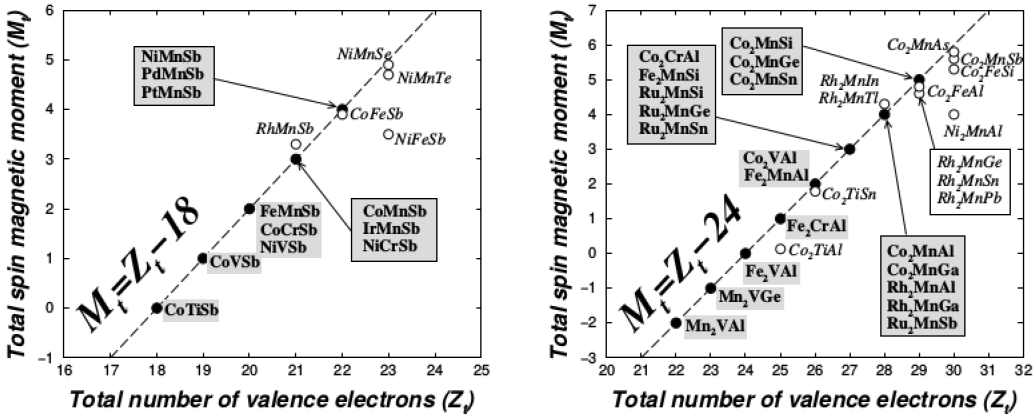

Figure 3.6: The valence linear dependence of the magnetic moment. The left panel indicates the half-Heusler compounds, and the right panel shows the case of full-Heusler compounds [74, 72].

by chemical substitution. They scale linearly with the number of valence electrons as depicted in Figure 3.6. This property is known as the Slater-Pauling rule [71]. For the half-metallic Half-Heusler compounds, there is a place for only nine valence electrons in the minority bands, and thus the magnetic moment is

$$m = (N - 18)\,\mu_{\mathrm{B}}. \tag{3.3}$$

The NiMnSb compound contains 22 valence electrons, and according to the Slater-Pauling rule, the total spin magnetic moment is $4\mu_{\mathrm{B}}$. Similarly, CoMnSb has shown in the literature a net spin moment of $3\mu_{\mathrm{B}}$ in an agreement with the Slater-Pauling rule.

The presence of the fourth transition-metal element in the case of full-Heusler compounds adds three bands below the Fermi level in the gapped channel. The change from half- to full-Heusler is the effect of adding three electrons to the minority channel and thus 12 electrons are occupied in the minority bands. Hence, the Slater-Pauling rule is written

$$m = (N - 24)\,\mu_{\mathrm{B}}. \tag{3.4}$$

3.3.2 Half-metallic ferrimagnet/antiferromagnet

Half-metallic ferrimagnetism/antiferromagnetism are new properties that characterize Heusler compounds of more than one magnetic sublattice [76, 77, 78, 79, 80]. Ferrimagnetism appears in materials whose crystal structures are characterized by magnetic

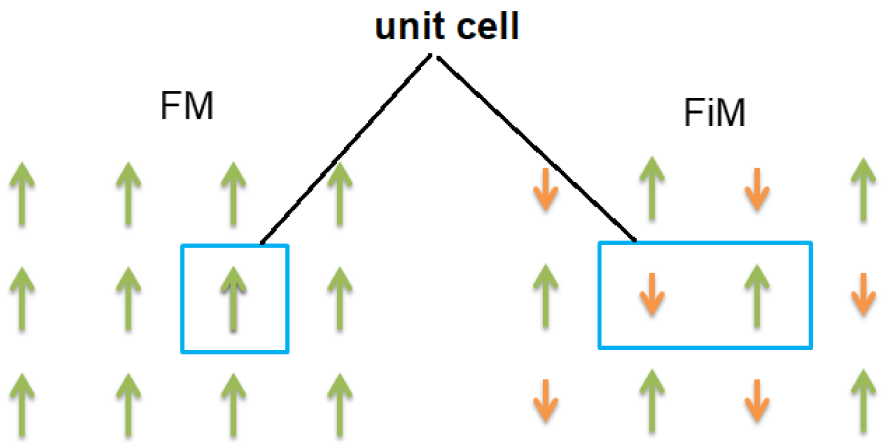

Figure 3.7: Schematic representation of the arrangement of magnetic moments in the ferromagnetic (FM) and ferrimagnetic (FiM) structure. The arrows indicate the magnetic directions. The magnetic moments align with a parallel orientation in the FM structure. While in the FiM state, the magnetic moments of unequal magnitude align with an antiparallel orientation. If the moments in the FiM arrangement are equal, the structure is called antiferromagnetic (not shown).

sublattices that are chemically or by symmetry inequivalent, such as in Heusler materials with the Mn_2YZ formula [75, 81, 82, 83, 84, 85, 86, 87, 88, 89, 50, 90, 91, 92, 93]. The simplified picture of ferromagnetic and ferrimagnetic structure is depicted in Figure 3.7. The antiparallel alignment of the spin moments at inequivalent sites allows for the spin-asymmetry of the corresponding band structure, producing a spin polarization with low net magnetic moment. Half-metallic ferrimagnets are the compounds that combine the Slater-Pauling behavior with the antiferromagnetic coupling of the magnetic moments.

From the technological aspect, half-metallic materials with low net magnetization are more desirable in spintronics. Since they do not give rise to large stray fields and their properties are less affected by external magnetic fields, maximizing the efficiency of spintronic devices. In addition, half-metallic ferrimagnets exhibit faster spin dynamics, an advantageous feature for producing small switching currents in spin-transfer torque-based MTJ devices [94]. Furthermore, a half-metallic ferrimagnetic tip can improve the performance of the spin-polarized scanning tunneling microscope.

The Heusler Mn_2VAl having the $L2_1$ structure structure is among the first compounds in which theoretically and experimentally the half-metallic ferrimagnetism with high Curie temperature has been studied [80]. Experimentally, antiparallel alignment between magnetic moments was observed in the inverse Heusler Mn_2CoGa [90]. Recently the ferrimagnetism with low net magnetic moment was directly observed in the inverse Heusler

spin-gapless semiconductor Mn_2CoAl. The magnetic moments were revealed using x-ray magnetic circular dichroism (XMCD), and an opposite sign was observed between magnetic moments at Mn(A) and Co sites [95].

Zero moment Spintronics materials, such as the half-metallic antiferromagnets, which are characteristic of some Heusler compounds, are more advantageous for applications [96]. Ideally, they are magnetically transparent against external magnetic fields, and no magnetic dipole fields can emerge from them to disturb the neighboring elements when they integrate into spintronic devices [97]. This advantage could pave the way for high-density integrated circuits. Of course, antiferromagnets have no magnetization. However, due to symmetry consideration, their band structures are identical for both spin directions, and hence the charge carries cannot be spin-polarized. In contrast, the characteristic rotational symmetry of antiferromagnets is not present in half-metallic antiferromagnets (also known as fully compensated half-metallic ferrimagnets). As a result, their electronic behavior is different for the two spin directions with zero total magnetic moments [98, 99, 100, 101, 102]. The exact zero net spin moment in conventional antiferromagnets is characteristic of spin rotational symmetry. Whereas it is related to the nature of spin-resolved electronic structure—one of the spin bands must have an energy gap at the Fermi energy—in half-metallic antiferromagnet [103]. We note that the exact zero spin magnetic moments are restricted to the zero-temperature limit in half-metallic antiferromagnets. At finite temperature, the half-metallic gap is not a well-defined quantity due to noncollinear spin excitations, and thus the net spin moment deviates from its exact (integer) value.

3.3.3 Spin-gapless semiconductor

Spin-gapless semiconductor (SGS) presents a new type of spin-dependent electronic structure. It was proposed with the study of the Co-doped $PbPdO_2$ by Wang and collaborators in 2008 [104]. This class of spintronics material is unique because its electronic structure at the Fermi level shows an energy band-gap that is zero for one spin direction while it is finite in the opposite spin. Thus, the excited charge carriers both electrons and holes can be fully spin-polarized. Additionally, the presence of a real gap for one spin band leads to the voltage-tunable spin-polarized transport properties by shifting the Fermi level in this gap. SGSs can be the appropriate magnetic materials for semiconductor spintronics, which can serve the spin-injectors due to their high electrical resistivity compared to magnetic metal. Therefore, the resistivity mismatch can be overcome in the junction SGS/semiconductor for efficient spin injection [105, 106, 107].

For Heusler compounds, Ouardi *et al.*, are the first to have experimentally verified the unique SGS behavior at room temperature in the inverse full-Heusler compound Mn_2CoAl

[108]. After that, Heusler compounds were considered as potential candidates for hosting the SGS property. Skaftouros *et al* [109]., have reported using first-principles electronic-structure calculations of several potential candidates for the SGS state. Some of them display zero total magnetic moments with high Curie temperature, an additional desirable feature [110]. Unfortunately, recent total energy calculations from first principles show that these compounds are never stable in the inverse Heusler cubic structure. They all except the Ti_2MnAl compound prefer to crystallize in the tetragonal structure, and their unique properties were lost in this low symmetry structure [47].

3.4 Formation and interaction of the magnetic moments

Besides the technological interest, magnetic Heusler compounds provide a new area for studying the fundamental aspects of magnetism like itinerant and localized magnetism as well as the magnetic interaction. Many promising Heusler compounds contain Mn atoms as one of their constituent elements. The Mn element which is surrounded by main group elements in the octahedral environment has a well-defined local magnetic moment in Heusler compounds. Kubler and collaborators are among the first which address this feature by employing *ab-initio* electronic structure calculations [70]. They have found in their study in the case of Co_2MnAl, Co_2MnSn, Ni_2MnSn, Cu_2MnAl, Pd_2MnIn, Pd_2MnSn, and Pd_2MnSb that the magnetization of these compounds is mainly confined at Mn sites. They show that the magnetic moments of Mn are of localized character despite the delocalization of their electrons.

The authors have explained the microscopic mechanism of this localized behavior by comparing the partial DOS of Mn and (X=Co, Ni, Cu, and Pd) atoms for both spin directions. They have observed that Mn and X atoms participate by their d states in forming a common d band around the Fermi level. Therefore, the occupied part of the d states of the Mn atoms delocalized through the whole crystal due to their strong hybridization with the d states of X atoms, forming itinerant electrons. However, due to the large exchange splitting of Mn $3d$ states, the minority band is mainly empty by Mn occupations, resulting in an exclusion of minority electrons from the Mn $3d$ shell. Therefore, in real space, this exclusion occurs only in localized regions around the Mn centers, leading to Mn magnetic moments with a very localized character. On the other hand, Co_2TiZ compounds with Z are Si, Ge and Sn fully exhibit itinerant magnetism [111].

With DFT, the itinerant or localized behavior of the spin moments can be revealed

using the disordered local moment (DLM) procedure in the coherent potential approximation (CPA), or the fixed magnetic moment (FSM) calculations. While magnetic moments of localized nature are robust to rotations, those of itinerant character are not. The magnitudes of itinerant moments vary significantly, depending on the deviation of the constrained magnetic state from the ground state (unconstrained). Accordingly, Qin *et al* [112]., show that the Fe and Mn magnetic moments are well-defined local moments embedded in an itinerant ferromagnetic background provided by the Co atoms in Co_2FeSi and Co_2MnSi compounds. By combining experimental and *ab-initio* studies, similar behavior was found in Mn_2CoGa compound [90]. In the Co_2TiSi compound, Co atoms carry almost the magnetic moments. These moments are itinerant because both the DLM and FSM significantly affect their magnitudes [111, 112].

The spin magnetic moments in a magnet interact with each other via the exchange mechanism. According to the nature of this interaction the magnetic state can be classified. One can typically observe that magnetic Heusler alloys behave as a local-moment system [70, 113, 114]. This fact implies that the Heisenberg model can be considered for the description of magnetic Heusler compounds.

The mapping of the *ab-initio* electronic structure calculations to the Heisenberg model allows for determining the exchange couplings. In recent studies, both direct and indirect exchange interactions have been found to contribute to the magnetic coupling in Heusler compounds. The first contribution to this study using *ab-initio* methods was also made by Kubler and his collaborators in the article where they studied the mechanism of local moment formation, as mentioned above. They conclude that indirect exchange interaction, both RKKY and superexchange, are responsible for coupling the local Mn moments separated by about 4Å. Şaşıoğlu *et al* [115]., performed more systematic first-principles calculations to study Mn-based Heusler alloys. They used the frozen-magnon approach to determine the exchange interactions of different sublattices. Their study revealed indirect coupling between Mn moments, where they found that the conduction *sp* electrons play an important role in mediating the interaction. Meinert *et al* [50]., have calculated the exchange coupling of the Mn_2CoZ (Z = Al, Ga, In, Si, Ge, Sn, Sb) inverse Heusler compounds from the first principles. Their calculations are based on the real-space magnetic force theorem. They found that the direct exchange between moments in the inter-sublattice dominates the pattern of exchange interaction. Their calculated Curie temperature is very high due to the large direct exchange. The same authors have shown that the hypothetical Mn_2TiZ (Z = Al, Ga, In, Si, Ge, Sn, P, As, Sb) compounds have complex exchange interactions, where both direct and indirect exchange couplings are present [89].

Part III

Results and Discussions

Chapter 4

Prediction of High T_C Half-Metallic Ferrimagnetism: Mn_2LiZ (Z = Si, Ge and Sn)

4.1 Introduction

Based on *ab-initio* calculations, the properties of the new Mn_2LiZ Heusler compounds are presented and discussed. The compounds are designed from the concept that filling the voids contained in some hypothetical half-Heusler compounds can lead to the stability of new Heusler compounds. Some Li-based Heusler compounds exist, like Co_2LiGe and Ni_2LiSi, but none of them present magnetic behavior[116]. Theoretically, Mn_2LiZ Heusler compounds with Z is As and Sb are reported to be interesting half-metallic ferrimagnetic materials [117].

The electronic structure calculations presented in this study are performed using the more accurate method, namely the full-potential linearized augmented plane wave method, implemented in the WIEN2k code [118, 119]. A $17 \times 17 \times 17$ **k**-point grid is used for the Brillouin zone integration. The number of plane waves is truncated to $R_{\mathrm{MT}} \times K_{\mathrm{max}} = 8$, where K_{max} is the maximum of the wave vector. The muffin-tin radii R_{MT} is chosen for all atoms equal to 2 a.u. to avoid overlaps at small lattice parameters. The energy and charge convergence criteria are set to less than 0.00001 Ry and 0.00001 e/a.u.^{3}, respectively.

We use the BoltzTraP code for the calculation of electronic transport properties [65]. As discussed previously, this program is based on the semiclassical Boltzmann transport theory in constant relaxation time and rigid band approximation. In determining the thermoelectric transport properties, the band energies are recalculated by WIEN2k with

a high **k**-points mesh of 79^3 to obtain accurate results.

The exchange coupling parameters J_{ij} are determined by employing the full-potential spin-polarized relativistic Korringa-Kohn-Rostoker Green's function as incorporated in the SPRKKR program [62, 29]. From the calculation of the exchange couplings, the Curie temperature is inferred in the mean-field approximation. The calculations are carried out on the equilibrium lattice parameter determined by WIEN2K. The angular momentum cut-off $\ell_{\max} = 3$ is used with about 300 **k**-points in the irreducible wedge of the Brillouin zone. We calculate the exchange coupling parameters on a high denser mesh of about 1000 **k**-points. The self-consistency was achieved for the energy convergence criterion of less than 0.00001 Ry.

All self-consistent calculations presented in this study are carried out within the generalized gradient approximation of Perdew, Burke, and Ernzerhof for the exchange-correlation functional [22]. The scalar-relativistic representation of the valence states is considered, while the core states are treated in an entirely relativistic manner. The results in this chapter were published in Reference [120]

4.2 Structural, mechanical and thermodynamic stability

Structural optimization is done to determine the equilibrium crystal structures. The minimization is carried out by fitting the total energy as a function of unit cell volume to the Birch-Murnaghan equation of state for both $L2_1$ and XA structures. These two structures are the only possible ordered arrangements for atoms in ternary cubic-Heusler compounds. For magnetic competition, the total energy is calculated for each structure in the non-spin-polarized (nonmagnetic) and spin-polarized cases. To address whether or not the assumed cubic structures may or may not have a tetragonal distortion and their stability, we also calculated the total energy with various c/a_t ratios at different constant unit cell volumes.

In the $L2_1$ structure, the results indicate that spin-polarized calculations converge to the ferromagnetic state. However, only the ferrimagnetic state can be stabilized in the case of the XA structure. We denote that the ferrimagnetic solution of the Mn_2LiSn in the XA structure is only reached when constraining the calculations to the antiferromagnetic configuration. In Figure 4.1, we can see that all energy curves present parabolic behavior around the equilibrium lattice constants, which correspond to the lowest total energies. For all three compounds, the ferrimagnetic state in the XA structure presents the lowest total energy, as can be seen in Figure 4.1. Although the number of valence electrons of Mn

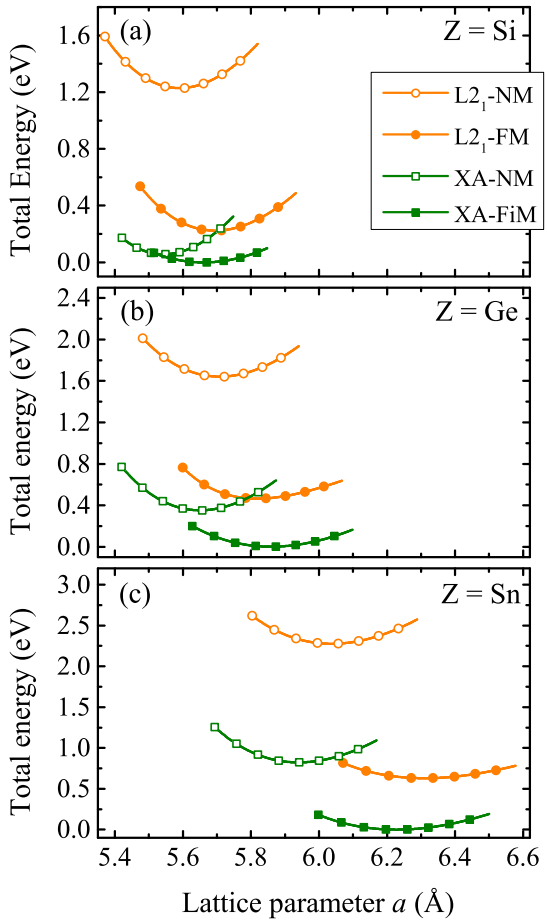

Figure 4.1: The calculated total energy of Mn_2LiZ compounds as a function of lattice parameters for both $L2_1$ and XA cubic structures, and with non-magnetic (NM), ferromagnetic (FM) and ferrimagnetic (FiM) configurations.

is not smaller than that of Li, the compounds prefer to crystallize in the XA structure. It is observed that the equilibrium lattice parameter increases with increasing atomic number of the main group element.

Now we focus on the tetragonal distortion of the cubic structures for the three compounds. In Figure 4.2, the results of the calculated total energy as a function of the c/a_t ratio are presented for all compounds. They are calculated on the equilibrium conserved-unit cell volume in both $L2_1$ and XA structures in their magnetic states. We can see that the two structures behave differently under tetragonal distortion and show two different characteristics. In the XA structure, we found no preference for tetragonal structure. In all compounds, we see only one minimum total energy with $c/a_t = \sqrt{2}$ associated to the cubic inverse-Heusler structure. However, we find that the case is different for the $L2_1$ structure. While the total energy curve of the Mn_2LiSi compound shows only one minimum located at $c/a_t = \sqrt{2}$, the increasing of the atomic number of Z atom results in that the energy curve develops toward those of tetragonal character. This is illustrated

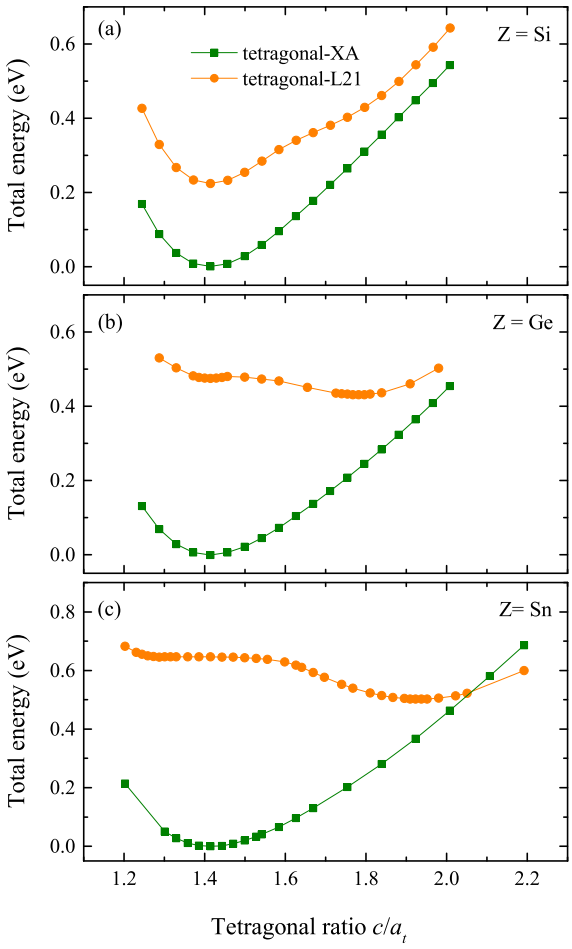

Figure 4.2: The calculated total energy of Mn_2LiZ compounds as a function of the c/a_t ratio for $L2_1$ and XA tetragonal structures in their magnetic configurations. a_t is the lattice constant of the tetragonal phase and thus $c/a_t = \sqrt{2}$ corresponds to the cubic lattice.

in Figure 4.2, where in addition to the cubic minimum, there is a tetragonal minimum of the total energy. In Ge- and Sn-based compounds, the tetragonal structure has lower total energy than the cubic $L2_1$ structure. Hence, with the increasing atomic number of the Z elements, the tetragonal structure becomes more and more stable.

The detailed description of the tetragonal distortion in Heusler compounds is beyond the scope of this thesis, and for more details, we suggest References [68, 69]. What is essential is that the present compounds are still stable in the assumed XA cubic structure, which shows lower total energy, as is plotted in Figure 4.2. Thus all that follows will be carried out in the cubic XA structure in a ferrimagnetic state.

For mechanical stability, the elastic constants C_{ij} are calculated, which in the case of the cubic symmetry, the analysis reduces to the three independent constants, namely C_{11}, C_{12} and C_{44}. The elastic constants are determined from the calculated total energies of different strains. The total energies of the monoclinic, orthorhombic, and tetragonal strain types are fitted to a 4th-order polynomial. A more recent and detailed study on

Table 4.1: Calculated lattice parameters (in Å), elastic constants (in GPa), formation energies (in eV) and hull distance (in meV/atom) of Mn_2LiZ (Z = Si, Ge, Sn).

Compound	a	C_{11}	C_{12}	C_{44}	E_f	ΔH
Mn_2LiSi	5.66	141.74	46.57	122.39	−1.07	40
Mn_2Si	5.40				−0.45	
Mn_2LiGe	5.86	125.36	57.36	99.18	−0.74	20
Mn_2Ge	5.60				0.00	
Mn_2LiSn	6.23	104.45	52.18	80.26	−0.39	90
Mn_2Sn	6.04				0.47	

the derivation and analysis of the mechanical properties of cubic systems is presented in Reference [121]. Here we only address the mechanical stability of our Heusler compounds. All the present Mn_2LiZ compounds are stable against small mechanical deformation, because the elastic constants, as summarized in Table 4.1, meet the criteria of mechanical stability [122]

$$\begin{aligned} C_{11} + 2C_{12} > 0, \\ C_{11} - C_{12} > 0, \\ C_{44} > 0. \end{aligned} \tag{4.1}$$

For thermodynamic stability, at least the formation energy must be negative. This quantity is defined as the total energy difference between the compound and its constituent elements, given by

$$E_f = E_{\mathrm{Mn_2LiZ}} - (2E_{\mathrm{Mn}} + E_{\mathrm{Li}} + E_{\mathrm{Z}}), \tag{4.2}$$

where $E_{\mathrm{Mn_2LiZ}}$ is the total energy of Mn_2LiZ compound in the XA structure. E_{Mn}, E_{Li} and E_{Z} are respectively the total energies of Mn, Li and Z in their bulk phases. The equilibrium lattice parameters and formation energies are listed in Table 4.1. As one descends the periodic table, the increased lattice constant of Mn_2LiZ (Z = Si, Ge and Sn) is attributed to the increase in the atomic radius of Z elements. We can see that all three compounds show negative formation energy and thus meet one of the requirements of thermodynamic stability. The formation energy correlates with the lattice constant, where its absolute value decreased in the sequence Si–Ge–Sn. The calculated lattice constants of the Mn_2LiZ compounds are in the range of that of zinc-blend semiconductors. The lattice constant of Mn_2LiSi is well matched to that of both GaAs ($a = 5.65$ Å) and ZnSe ($a = 5.66$ Å), as well as to the diamond semiconductor Ge ($a = 5.65$ Å). The lattice of

Mn_2LiGe and Mn_2LiSn compounds can be matched with that of InP ($a = 5.86$ Å) and ZnTe ($a = 6.1$ Å), respectively. This lattice matching is necessary for the epitaxial growth of these compounds on top of semiconductor substrates for use in spintronics applications and spin injection.

The Mn_2LiZ compounds in the XA structure can be regarded as a simple design of filling the voids of Mn_2Z compounds in the $C1_b$ structure with Li atoms. This design scheme was recently adopted in order to discover new semiconducting quaternary Heusler compounds based on the 18-electron rule [3]. The Li atom is suitable to fill the void in the half-Heusler structure due to its small size, and it can donate the only electron in its outer shell to participate in the covalent bonding. This strategy may lead to the stability of compounds in the Heusler structure. For example, we also calculated the formation energy of Mn_2Z half-Heusler compounds, and the results are summarized in Table 4.1. The results indicate that only the Mn_2Si compound exhibits negative formation energy. The value of its formation energy is about twice that of the Li-compound, Mn_2LiSi. As the atomic number of the Z element increases, the formation energy increases, and the compounds become more and more thermodynamically unstable. Therefore, compared to Mn_2Z half-Heusler compounds, the Mn_2LiZ are stable compounds due to Li filling of voids in the half-Heusler structure.

Negative formation energy is necessary but not a sufficient condition for the requirement of energetic stability. It only indicates that a compound is stable against decomposition into its constituent elements, not into binary, ternary phases, or a linear combination of the respective composition. One way to address this thermodynamic issue is to calculate the hull distance ΔH; The energy difference between the formation energy and the convex hull. On the convex hull point, a phase is in its stable ground state with the lowest energy than any other state in the same composition. Therefore, a zero hull distance indicates that the compound is thermodynamically stable.

The convex hull can be obtained from the linear interpolation between stable phases. A simple example is the compounds with the binary composition, AB. If we assume A, B and $A_{1-x_0}B_{x_0}$ at a specific composition x_0 are stable phases, then we can construct the energy curve from linear interpolation of their formation energies, *i.e.*, the convex hull energy curve for any composition x between 0 and 1, as illustrated in Figure 4.3. For ternary phases, the energy surface in the composition space must be constructed from the formation energies of known phases to determine the convex hull. In our case, we utilize the convex hull energies available in the Open Quantum Materials Database (OQMD) to evaluate the hull distance of the Mn_2LiZ compounds [123, 124]. As is illustrated in Table 4.1, all calculated ΔH of the present compounds are less than 100 meV. A recent study shows that inverse full-Heusler compounds with a hull distance of less than 52 meV

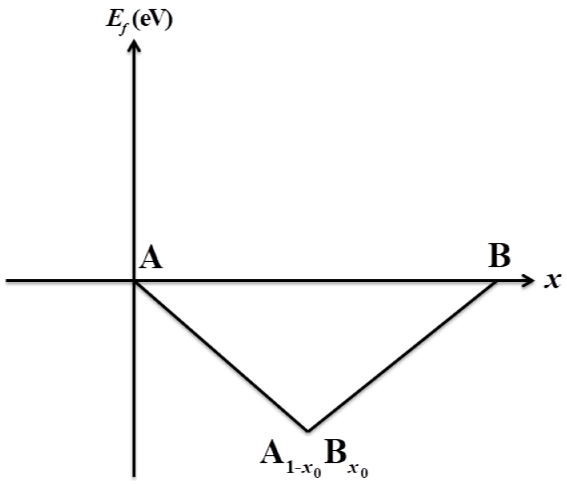

Figure 4.3: Schematic illustration for the construction of the convex hull in the case of binary compounds.

can be possibly synthesized because many Heusler compounds that have been synthesized have a hull distance that falls in the range $(0-52)$ meV [125]. Accordingly, Mn_2LiSi and Mn_2LiGe compounds that have hull distances of 40 and 20 meV, respectively, are likely to be synthesized.

4.3 Electronic structure and magnetic moments

The calculated spin-resolved band structures of Mn_2LiZ compounds with the XA structure are displayed in Figure 4.4. Mn_2LiZ with Z is Si, Ge and Sn are isoelectronic compounds where one can expect similar electronic structures with a subtle difference, and this is what we found, as seen in Figure 4.4. The Fermi level is set to the origin, which cuts the conduction bands in all three compounds for spin-up (majority spin) electrons, indicating metallic nature in this spin channel, while a real energy gap exists at the Fermi level for spin-down (minority spin) electrons.

It can be seen that from about -11 to -8 eV, the compounds show the formation of a single band which is the s-band. For both spin directions, this band is nearly identical (spin unpolarized) in that it is not affected by the exchange splitting. As one approaches the Fermi level, spin-down bands differ from spin-up bands to the extent that an energy gap appears at the Fermi level.

Therefore, the compounds are half-metals with wide band gaps. For minority electrons, all band gaps are indirect. The minimum of the conduction band is positioned at X-point, and the maximum of the valence band changes its position from L- to G-point with the

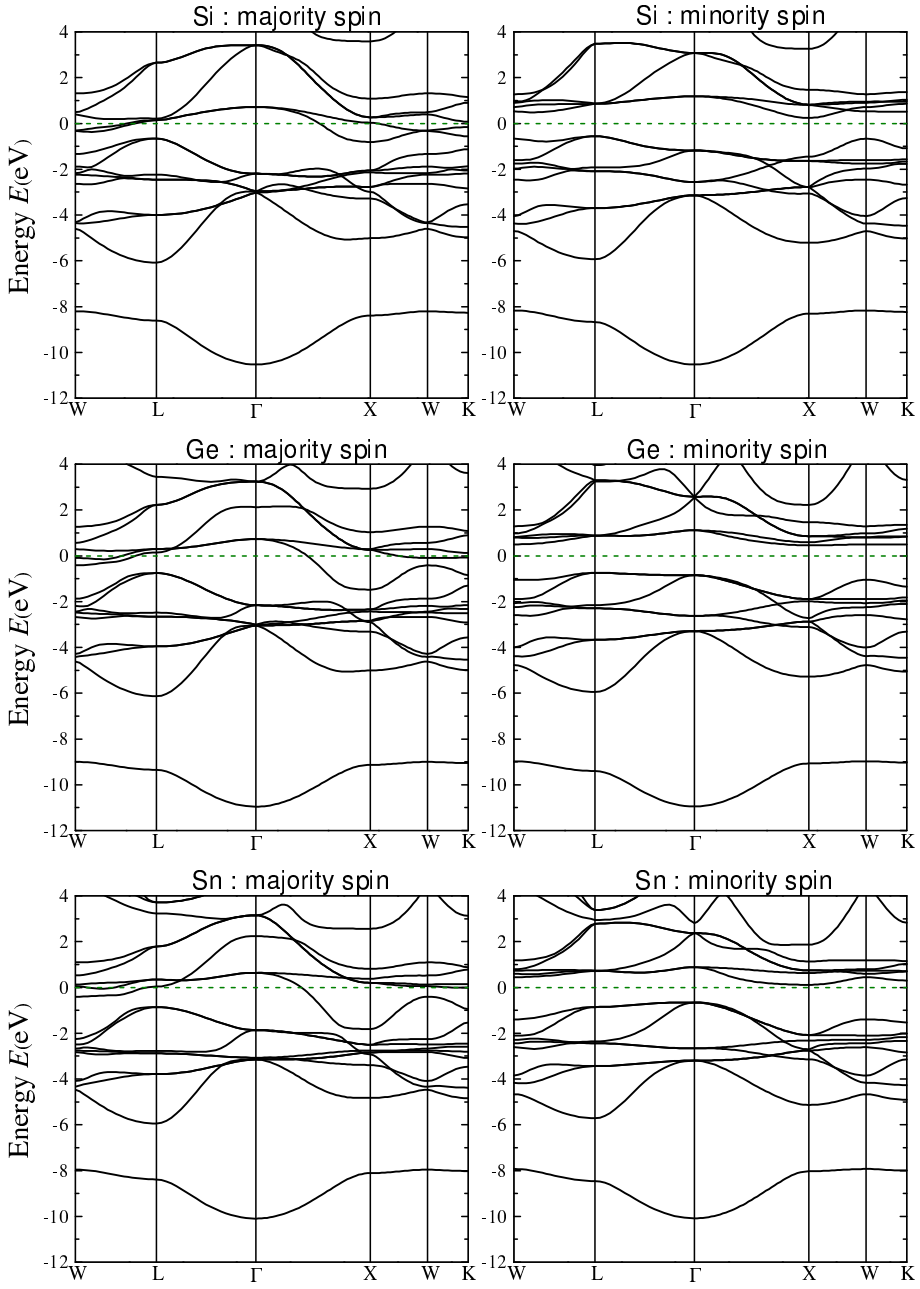

Figure 4.4: Calculated band structure for majority spin (left panel) and minority spin (right panel) of Mn_2LiZ (Z = Si, Ge and Sn).

increasing atomic number of Z elements. The electronic-band behavior of Mn_2LiGe around the Fermi level takes an intermediate position. The values of the band gap are shown in Table 4.2. The Mn_2LiGe compound has a larger band gap of about 1.15 eV. For majority

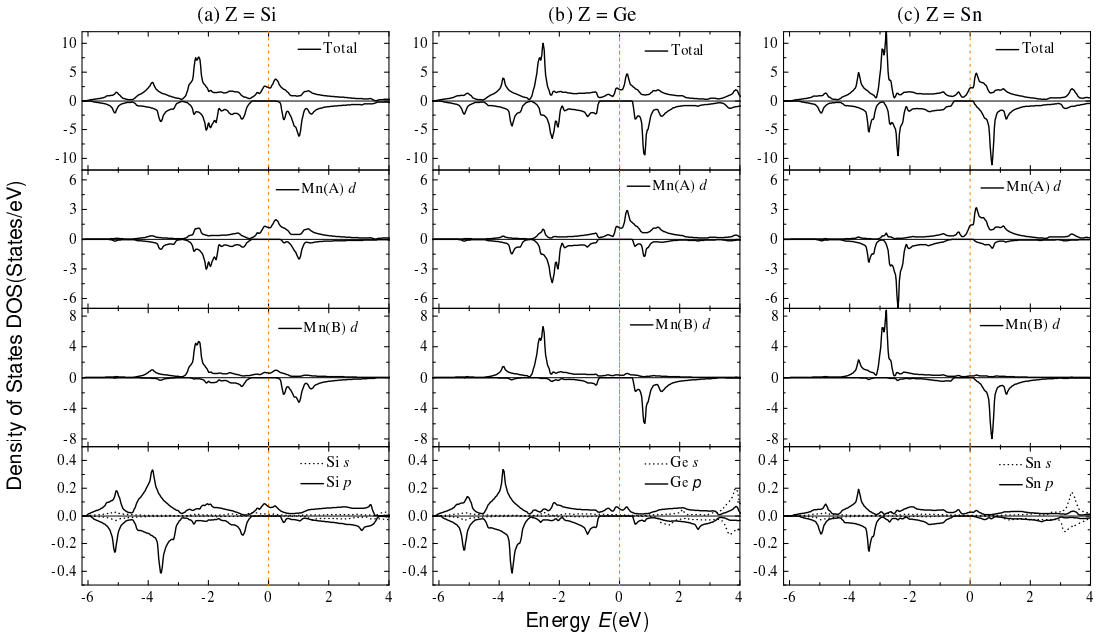

Figure 4.5: Total and Partial DOS of (a) Mn_2LiSi, (b) Mn_2LiGe and (c) Mn_2LiSn compounds.

spin, we found around the Fermi level that the width of one conduction band along the Γ-X high symmetry line increases with increasing the atomic number of the Z-element.

We also calculated the density of state (DOS) to obtain more information about the origin of the formation of the band structures. Figure 4.5 shows the total and partial DOS for both spin electrons. Positive (negative) DOS are plotted for majority (minority) electrons. One can see that the total DOS of all compounds are nearly identical, presenting the feature of a half-metal with a large gap. The low-lying bands from −11 to −8 eV originated from the *s* electrons of the Z atoms and are nearly identical for both spin directions. This contribution to the bands is omitted in Figure 4.5. The *s* bands are well separated from the other bands by a hybridization gap. The Ge-based compound has a larger hybridization gap similar to the Co_2TiGe alloy reported by Barth *et al.*, reflecting the strong chemical bonding between Ge and Mn atoms [111]. The high-lying energy from −6 to 4 eV consists mainly of *d* states of the Mn(A) and Mn(B) atoms, including the contribution from the *p* electrons of Z atoms. The contribution of the Li atom in the DOS is negligible, and we did not show it in Figure 4.5.

The minority gap is in-between the bonding and antibonding bands, originated from the hybridization of *d* states of the two inequivalent Mn atoms. Hence, the electronic structure of our full-Heusler compounds is similar to the usual half-metallic half-Heusler compounds [72]. This is not surprising, because one can see that our compounds are those of a half-Heusler structure with voids occupied by Li atoms, and the latter does not

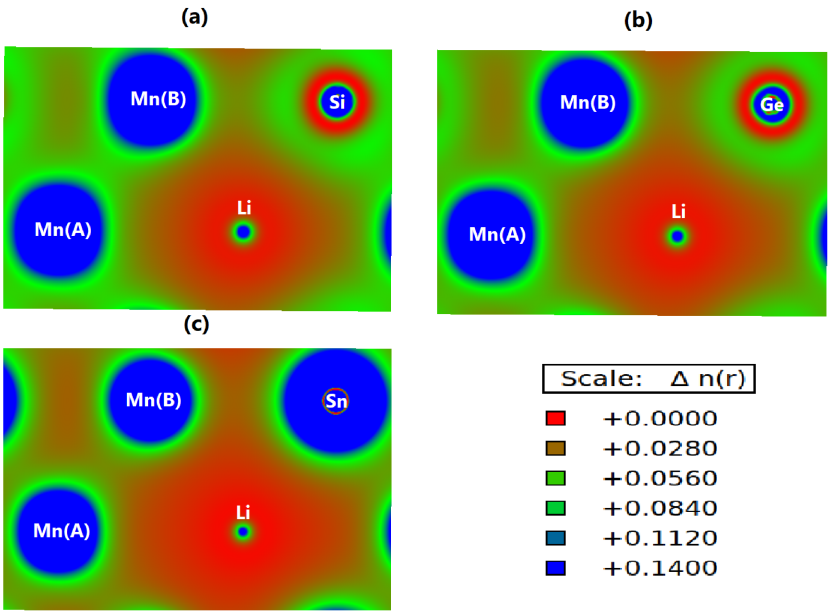

Figure 4.6: The distribution of the valence electron charge density of (a) Mn_2LiSi, (b) Mn_2LiGe and (c) Mn_2LiSn compounds, plotted on the $(01\bar{1})$ surface.

contribute to the hybridization.

It appears from the inspection of the DOS that bonding bands consist mainly of the Mn(A) minority d states and Mn(B) majority d states. The order reversed above the Fermi level, where the formation of the anti-bonding bands has mainly contributed from Mn(A) majority d states and Mn(B) minority d states. As discussed by Williams and coworkers, instead of most magnetic materials where their magnetism is described by the Stoner model (rigid-band theory), the compounds studied here show a particular spin-dependent hybridization attributed to the covalent-magnetism [126].

The valence electron density is calculated to illustrate the distribution of the charge

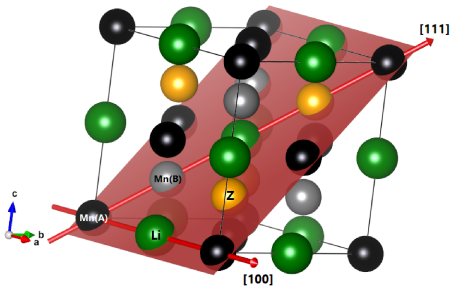

Figure 4.7: Schematic illustration of the $(01\bar{1})$ plane section in the case of Mn_2LiZ compound in the inverse Heusler structure.

density inside the lattice in order to reveal more about the nature of the bonding. Figure 4.6 depicts the pattern of the charge density of Mn_2LiZ compounds (Z = Si, Ge and Sn) on the $(01\bar{1})$ plane (see Figure 4.7). It is seen that a significant charge density is concentrated in between Mn(A) and Mn(B) atoms, indicating a covalent bonding due to the large hybridization of the d state of the inequivalent Mn elements, which are along [111] direction. The strength of this covalent nature seems to decrease going from Figure 4.6(a) to 4.6(c); *i.e.*, it decreases with increasing the atomic number of Z atoms (expansion of the lattice constant).

Along [100] direction, the charge distribution is also noticeable between Mn(B) and Z elements, which decreases from covalent in Mn_2LiSi to ionic nature in Mn_2LiSn compound.

It can be seen that there is a charge depletion (region of the lowest density) around the Li atom, which indicates that electrons in this region is transferred from Li to its neighboring elements, thus revealing a ionic bonding between the corresponding elements.

In Table 4.2, the calculated partial (site projection) and total spin magnetic moments of the Mn_2LiZ compounds are summarized. We find that the magnetization is confined to the Mn sites. The elements Z, Li and the interstitial region show a negligible contribution to the net spin magnetic moment. One can see that the value of the Mn(A) magnetic moment is negative, while it is positive for that of Mn(B). Therefore, the spin moments between neighboring Mn moments are antiferromagnetically coupled.

The half-metallic property of our compounds constrains the total spin moment to integral values. As can be seen, all three compounds have smaller integer magnetic moment of $1\mu_B$ per unit cell. The compensation of spin moment in sublattices A and B produces smaller total magnetic moments. As will be discussed in the following paragraph, the exact (integer) value of the total spin moment results from the existence of a minority band-gap (Slater-Pauling rule). We find that Mn(B) element carries a magnetic moment larger than that of the absolute value of Mn(A). Since the lattice parameter of Mn_2LiZ increases with an increasing atomic number in the same group of Z elements, the hybridization between the Mn(A) and Mn(B) atoms decreases. As a result, their atomic-like (localized) character increases, and thus their absolute spin magnetic moments are increased.

The Mn_2LiZ alloys have $N = 19$ valence electrons per unit cell. From the band structure of our compounds, there are 9 minority bands below the Fermi level, and hence the minority channel contains 9 valence electrons. So, the remaining 10 electrons have to occupy the opposite spin bands. Therefore, the spin magnetic moment m of Mn_2LiZ compounds obeys the following Slater-Pauling rule [72]:

$$m = (N - 18)\mu_B. \tag{4.3}$$

Table 4.2: Calculated partial and total magnetic moments (in μ_B), minority band gaps (in eV) of Mn_2LiZ (Z= Si, Ge and Sn).

Compound	Mn(A)	Mn(B)	Z	Li	Interstitial	m	Gap
Mn_2LiSi	−1.27	2.25	0.00	0.02	0.01	1.00	0.82
Mn_2LiGe	−2.02	2.92	0.02	0.03	0.05	1.00	1.15
Mn_2LiSn	−2.51	3.36	0.02	0.03	0.10	1.00	0.66

This suggests that Mn_2LiZ compounds with 18 valence electrons such as Z are Al, Ga and In should have a magnetic structure with zero net spin moments, as can be seen in the next chapter.

4.4 Exchange interactions and Curie temperature

To know more about both the strength and range of the exchange interactions of the three compounds, the calculated exchange couplings as a function of the normalized distance in Mn(A)-Mn(B) inter-sublattice, Mn(A)-Mn(A) and Mn(B)-Mn(B) intra-sublattices are displayed Figure 4.8. In all compounds, the exchange parameters are confined within a radius of 1.5 a. It seems that exchange interaction in the Mn(A)-Mn(B) inter-sublattice is the strongest and contributes the most to the overall interaction.

In the inter-sublattice, the interaction with the first and the second coordination

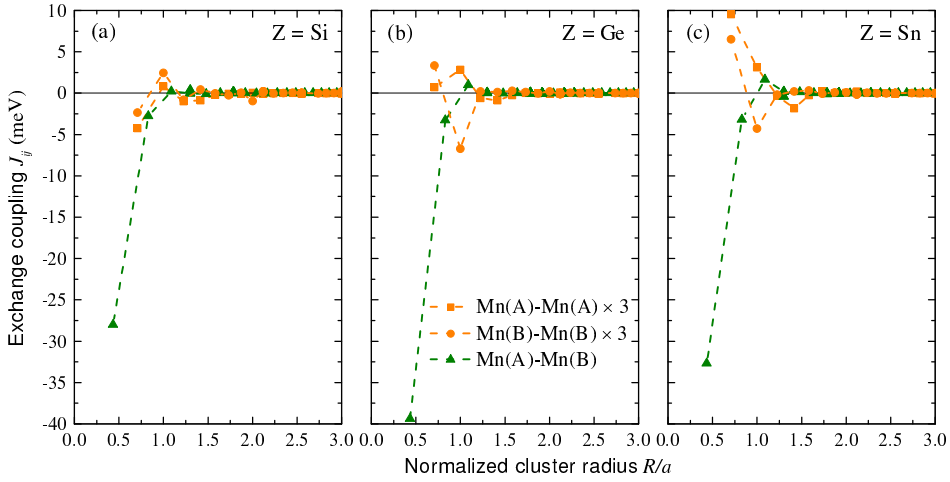

Figure 4.8: Exchange interaction parameters as a function of the normalized cluster radius of Mn_2LiZ (Z = Si, Ge and Sn). The intra-sublattice exchange interactions are multiplied by 3 for more illustration.

spheres is negative, reflecting the anti-parallel alignment between magnetic moments in Mn(A) and Mn(B). In the second sphere, the absolute value of the interaction is much weaker than in the first one. With the first sphere, the antiferromagnetic interaction increases from Si- to Ge-based compound, then decreases slightly to Mn_2LiSn. The Mn_2LiGe compound presents a larger value in agreement with its wider minority gap formed mainly by Mn(A) and Mn(B). However, the weaker interaction in the second sphere is almost independent of the type of the compound. The antiferromagnetic interaction with the third sphere has zero magnitude in Mn_2LiSi, and seems to slightly increase but remains weak. Due to the smaller distance between Mn(A) and Mn(B), the exchange is classified as direct in the first coordination sphere.

The interaction in the intra-sublattices is much weaker, but it shows a strong dependence on the type of Z atom. With the increasing atomic number of Z elements, the interaction with the first coordination sphere increases from negative in Mn_2LiSi to positive values in Mn_2LiGe and Mn_2LiSn. The interaction with the second sphere in Mn(B)-Mn(B) changes its sign to a negative value in the sequence Si-Ge, and then its absolute value increases slightly in the subsequent Z-based compound. For the Mn(A)-Mn(A) sublattice, the interaction with the second sphere is positive for all compounds and increases slightly. For further coordination, the interaction is negligible.

For practical applications, the Curie temperature T_C of the compounds must be equal to or exceed the room temperature. From the previous discussion, we found two coupled magnetic sublattices in Mn_2LiZ compounds. Thus the on-site interaction $\mathbf{J}$ is a 2×2 square matrix, allowing to write

$$T_C = \frac{1}{3k_B}\left[\operatorname{Tr}\mathbf{J} + \sqrt{\left(\operatorname{Tr}\mathbf{J}^2\right) - 4\det\mathbf{J}}\right], \tag{4.4}$$

where Tr and det denote the trace and the determinant, respectively. On the right-hand side of Equation 4.4, the second term always has a positive sign and is contributed by both intra- and inter-sublattice exchange interactions. The first term has contribution only from the exchange interaction in the intra-sublattices, which can be positive or negative. Therefore, the negative onsite interaction in intra-sublattice reduces T_C, and conversely, the positive interaction enhances it. In Table 4.3, the calculated onsite interaction $J_0^{\mathrm{Mn}(\mu)-\mathrm{Mn}(\nu)}$, mean-field approximation of T_C for inter-sublattice T_C^{inter} and all magnetic sublattices T_C^{all} of the compounds are summarized. For all compounds, we find that T_C is higher than 1000 K. This large value is mainly due the onsite inter-sublattice exchange interaction. As we can see, the Curie temperature calculated only for inter-sublattice interaction is nearly the same as that calculated from all contributions. The value of T_C^{inter} of Mn_2LiSi compound is slightly reduced due to negative Mn(A)-Mn(A)

Table 4.3: Calculated $J_0^{\mathrm{Mn}(\mu)-\mathrm{Mn}(\nu)}$ onsite sublattices (in meV), inter-sublattice and all-sublattices mean field Curie temperature (in K) of Mn_2LiZ (Z=Si, Ge and Sn).

Compound	$J_0^{\mathrm{Mn(A)-Mn(A)}}$	$J_0^{\mathrm{Mn(B)-Mn(B)}}$	$J_0^{\mathrm{Mn(A)-Mn(B)}}$	$T_{\mathrm{C}}^{\mathrm{inter}}$	$T_{\mathrm{C}}^{\mathrm{all}}$
Mn_2LiSi	−30.58	8.66	−141.94	1096	1022
Mn_2LiGe	−2.93	4.33	−184.75	1427	1433
Mn_2LiSn	33.86	19.72	−148.54	1147	1356

interaction, while both positive Mn(A)-Mn(A) and Mn(B)-Mn(B) interactions significantly enhance it by about of 200 K in Sn-based compound. Finally, the interaction in intra-sublattices of Mn_2LiGe can be omitted from the discussion due to their negligible contributions in computed T_{C}.

4.5 Thermoelectric transport

In Figure 4.9, we display the calculated temperature-dependent conductivity integrals σ/τ and Seebeck coefficients of Mn_2LiZ compounds. The conductivity integrals show weak dependence on the temperature, where they decrease slightly with increasing temperature. This behavior is typical for metals. The inset of Figure 4.9(a) shows the temperature dependence of the spin-polarization of the electric current

$$P = \frac{\sigma_\uparrow - \sigma_\downarrow}{\sigma_\uparrow + \sigma_\downarrow}. \tag{4.5}$$

It can be observed that the predicted 100% spin-polarized current at zero temperature can be preserved up to high temperatures in the two-current model. In particular, the electric current can be almost fully spin-polarized over the entire considered temperature range in a Ge-based compound. This is due to the large gap in the minority spin bands and the Fermi level being in the middle of the band gap.

Figure 4.9(b) depicts the Seebeck coefficient of all three compounds. In Si- and Ge-based compounds, the Seebeck coefficient is up to the room temperature nearly negligible. After that, its absolute value starts to increase smoothly for Mn_2LiGe and linearly to rather high values for Mn_2LiSi. The maximum absolute value of the Seebeck coefficient for Mn_2LiZ with Z is Si and Ge is 14.80 and 3.43 μV/V, respectively.

For the Mn_2LiSn compound, the Seebeck coefficient changes smoothly with increasing temperature. It slightly increases from a low positive value and then decreases to negative values crossing a line that separates positive and negative values. Interestingly, although the Seebeck coefficient in this compound is small, it shows two different behaviors with a

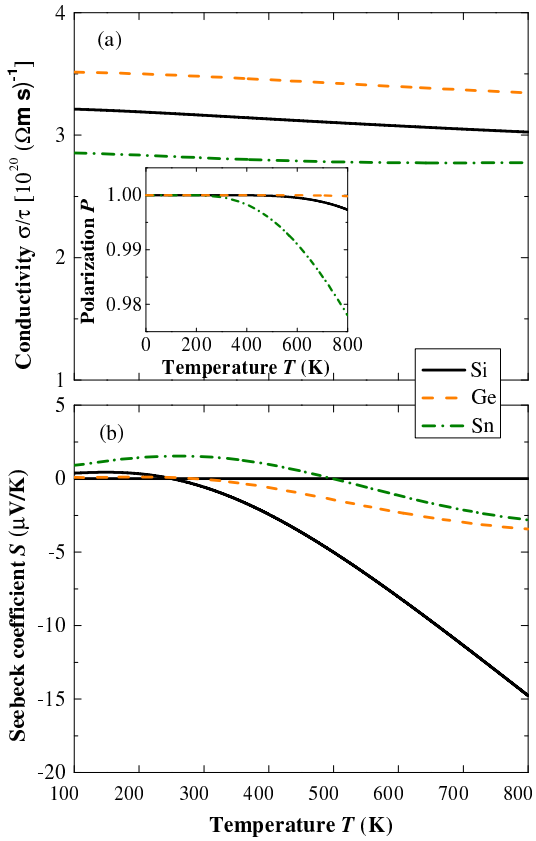

Figure 4.9: Temperature dependence of (a) conductivity integral σ/τ, where τ is a relaxation time and (b) Seebeck coefficient of Mn_2LiZ (Z = Si, Ge and Sn). The inset of (a) shows a spin-polarization of electric current P.

temperature gradient. One can observe in this compound p-type (n-type) thermoelectric transport at low (high) temperatures.

We note that the magnitude of the Seebeck coefficient is considerably smaller in magnetic materials than in nonmagnetic semiconductors. Small impurities or native defects which are inherent in the experiment can result in enhancing the Seebeck coefficient and also reversing its sign [127].

Chapter 5

Prediction of Spin Gapless Semiconductor and Nearly Spin Semimetal Antiferromagnets: The case of Mn_2LiZ (Z = Al, Ga)

5.1 Introduction

Spin gapless semiconductor (SGS) and spin semimetal (SM) antiferromagnets are interesting spintronic materials. They constitute new materials for spin logic devices based on spin injection schemes. Although they have great potential for use in spintronics with faster devices and low power consumption, they are still unexplored to be exploited. It is worth looking for SGS and SM among magnetic Heusler compounds because Heusler materials are a family of compounds that contain a huge number of compounds that are flexible to chemical substitution and have a high Curie temperature. In this respect, Mn_2LiZ (Z = Al, Ga and In) are studied in Heusler structures by first-principles methods to predict their properties. These compounds are characterized by two interesting points which should be mentioned. The first point is that Mn atoms in the octahedral environment provided by the Z atoms are known to have a well-defined localized magnetic moment known as the *Kubler rule*. The second point is that Mn_2LiZ (Z = Al, Ga and In) compounds all have $N = 18$ valence electrons which fulfill the 18-electron rule for semiconductivity, and according to the Slater-Pauling (SP) rule, they must show zero net magnetic moments. This leads to the interplay of the electronic structure with magnetism. The second magnetic moment in the tetrahedral environment adjusts to respect the SP

rule, while the Mn octahedral moment remains nearly unchanged because it is highly localized. With this fact, unconventional antiferromagnetism (ferrimagnetism with fully compensated magnetic moments) is achieved in these compounds.

In the framework of DFT, the electronic structure calculations are performed using the WIEN2k code. The muffin-tin radii are chosen for all atoms equal to 2 a.u. The number of plane waves is restricted to $R_{\mathrm{MT}} \times K_{\max} = 9$. We use about 15000 **k**-points for Brillouin zone integrations. The self-consistency is reached when the energy and charge convergence criteria are less than 0.00001 Ry and 0.00001 e/a.u.^{3} , respectively.

The transport properties are calculated within the Boltzmann transport theory under constant relaxation time using the BoltzTraP code. A denser mesh with about 88^3 **k**-points is used in the WIEN2k to calculate spin-dependent transport quantities. We use the SPRKKR program to determine the exchange coupling parameter. The calculations are carried out on the equilibrium lattice parameters determined with WIEN2K. In the self-consistent calculations, the angular momentum cutoff $\ell_{\max} = 3$ is used with about 300 **k**-points in the irreducible wedge of the Brillouin zone. The energy convergence criterion is less than 0.00001 Ry. J_{ij} is calculated on a denser mesh of about 1000 **k**-points.

All self-consistent calculations are carried out within the generalized gradient approximation of Perdew, Burke, and Ernzerhof for the exchange-correlation functional. The scalar-relativistic representation of the valence states is considered, while the core states are treated in a fully relativistic manner. The results in this chapter were published in Reference [128]

5.2 Structural, mechanical and thermodynamic stability

The total energies of Mn_2LiZ (Z = Al, Ga and In) compounds are calculated for various unit cell volume ($V = \frac{1}{4}a^3$) both in the $L2_1$ and XA structure. The calculations are performed in magnetic and non-magnetic configurations. The results are then fitted to the Birch-Murnaghan equation of states and presented in Figure 5.1. The cubic structural stability against tetragonal distortion has to be addressed, where many Mn_2-based Heusler compounds are known to crystallize in the tetragonal structure. To do this, the total energy is calculated with different c/a_t ratios while keeping the unit cell volume constant.

First of all, we must highlight the role of the inversion symmetry in the existence of the magnetic state within the present compounds. In the $L2_1$ structure, the atoms in the A and C sublattices are equivalent. As a result, the magnetic moments in A and C exactly compensate one another in the antiparallel coupling, giving an antiferromagnetic

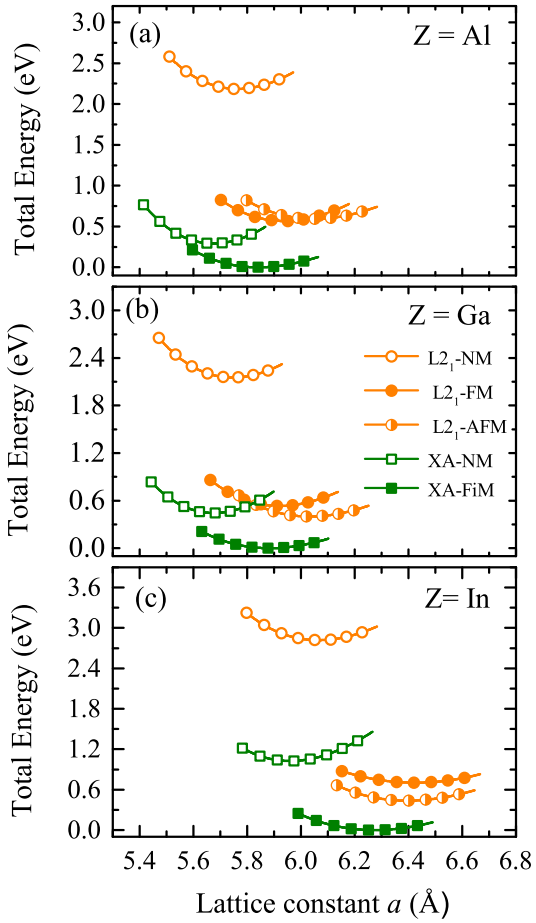

Figure 5.1: The total energy as a function of the lattice parameter of the Mn_2LiZ compounds (Z = Al, Ga and In) in the two structures. For the $L2_1$ structure non-magnetic (NM), ferromagnetic (FM) and antiferromagnetic (AFM) states are presented. In the XA structure only the non-magnetic and ferrimagnetic (FiM) states is considered.

structure. However, in the XA structure, inversion symmetry is absent where all sublattices are symmetrically inequivalent. The antiparallel alignment of the spin moments in the A and B sublattices leads to the formation of the ferrimagnetic structure. We recall that the complete compensation in this state does not occur without other considerations, such as the half-metallicity at zero temperature.

Accordingly, for calculations, we consider the ferromagnetic and antiferromagnetic configurations in the $L2_1$ structure, while we assume the ferrimagnetic state in the XA structure. The ferromagnetic state in the XA structure did not converge in our calculations. The non-magnetic configuration is calculated for both structures.

In Figure 5.1 all energy curves show parabolic behavior, and each energy curve has a minimum at its corresponding equilibrium lattice constant. We find that for both structures $L2_1$ and XA, the magnetic configurations have lower total energies, and hence they are more favorable than the corresponding non-magnetic states. In the $L2_1$ structure, the Mn_2LiAl compound shows that the ferromagnetic state is more stable than the antifer-

romagnetic one. However, the antiferromagnetic state becomes stable in the case of Ga- and In- based compounds. In all three compounds, the ferrimagnetic state in the XA structure has lower total energy than all reported structures. This result contradicts the observed rule that Heusler compounds prefer the inverse structure (XA structure) when the number of valence electrons of the X atoms is smaller than that of Y atoms. This may be the reason why the Mn_2NaAl compound and its isoelectronic Mn_2LiAl were reported as having the $L2_1$ structure [129]. Therefore, the present calculations reveal that the two compounds prefer to crystallize in the XA structure with the ferrimagnetic state. In Table 5.1, the lattice constants of Mn_2LiZ compounds are presented, where we find that Al- and Ga-based compounds have nearly the same lattice constant; this is because their Z atoms have a very close atomic radius. For thin film preparation, the semiconductor InP which has a lattice constant $a = 5.86$ Å, can be chosen for the epitaxial growth of Mn_2LiAl or Mn_2LiGa compounds on it owing to the good lattice matching.

The total energy as a function of the c/a_t ratio is calculated with different constant volumes and in both Heusler structures. In Figure 5.2, we present the results of the calculations for the stable magnetic configurations at constant equilibrium volume. The results indicate that the compounds are more stable in their cubic inverse structure over tetragonal distortion; there is neither stable nor metastable tetragonal structure. Both structures show only one minimum in the total energy curves associated with the cubic lattice structure $a_t = a/\sqrt{2}$. Therefore, the present Mn_2-based Heusler compounds are more stable in the cubic structure similar to Mn_2LiZ (Z = Si, Ge and Sn) compounds presented in chapter 4. As we will see, this can be motivating results, as many if not all zero spin moment SGS Heusler candidates have a stable tetragonal structure, and their unique properties are lost at this structure [47]. In what follows, the calculations are performed for the XA structure.

The elastic constants of Mn_2LiZ (Z = Al, Ga and In) are calculated to test the com-

Table 5.1: Calculated lattice parameters (in Å), elastic constants (in GPa), formation energies (in eV) and hull distance (in meV/atom) of Mn_2LiZ ($Z = Al, Ga, In$).

Compound	a	C_{11}	C_{12}	C_{44}	E_f	ΔH
Mn_2LiAl	5.84	132.08	44.83	117.89	−0.55	51
Mn_2Al	5.58				+0.70	
Mn_2LiGa	5.88	109.47	49.92	105.45	−0.57	19
Mn_2Ga	5.67				+0.69	
Mn_2LiIn	6.27	89.07	47.87	81.52	+0.01	150
Mn_2In	6.12				+1.32	

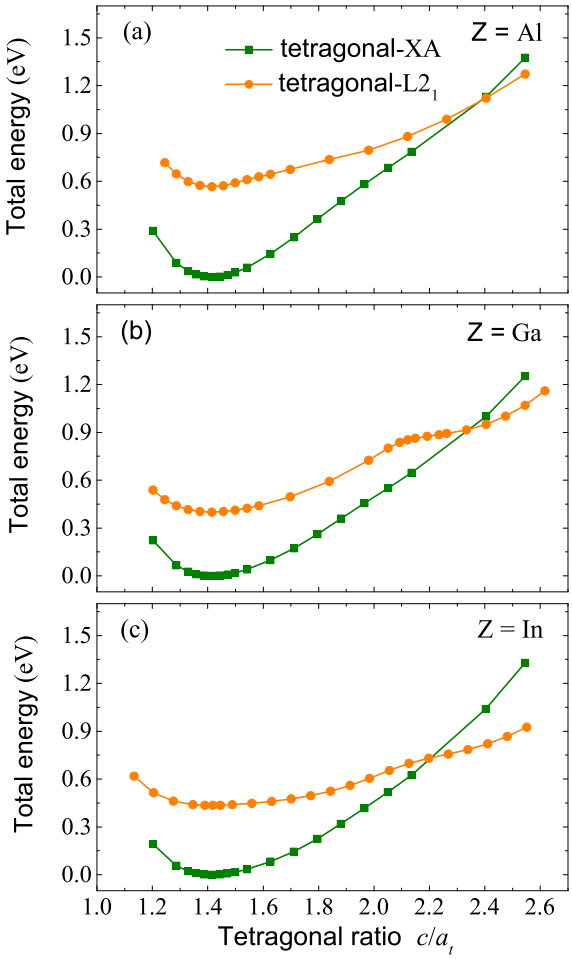

Figure 5.2: The total energy as a function of the c/a_t ratio of the two structures in their stable magnetic configurations.

pounds for their mechanical stability. The calculated results are summarized in Table 5.1. From Table 5.1, we find that all compounds meet the elastic stability requirement. One can see that the C_{11} and C_{44} coefficients decrease with increasing the atomic number of Z elements.

For thermodynamic stability, the formation energy, which is defined as the energy difference between the total energy of the compound and the sum of its constituent elements, is calculated. The calculated results for each compound are summarized in Table 5.1. It can be seen that only Mn_2LiAl and Mn_2LiGa compounds exhibit negative formation energy. This energy is approximately the same for these compounds and correlates with the lattice parameter. Mn_2LiIn compound shows nearly zero formation energy, and hence it may be thermodynamically unstable. Therefore the calculations indicate that Al- and Ga-based compounds meet one of the conditions for thermodynamic stability. Compared to Mn_2LiZ compounds, we also calculated the formation energies of Mn_2Z compounds, which are presented in Table 5.1. The results reveal that all Mn_2Z compounds are un-

stable because they show positive formation energies and thus cannot be synthesized in the $C1_b$ structure. Consequently, the filling of the voids of Mn_2Z half-Heusler compounds is energetically favorable and can yield stable Mn_2LiZ Heusler compounds. In the last column of Table 5.1, the hull distance is presented. Al- and Ga-based compounds are likely to be synthesized because they show a smaller ΔH which is 51 meV for Mn_2LiAl and 19 meV for Mn_2LiGa, and all are less than the empirical criterion of 52 meV [125].

5.3 Electronic structure and magnetic moments

The spin-resolved band structure calculations of the Mn_2LiZ (Z = Al, Ga and In) compounds are presented in Figure 5.3. The Left (right) panel depicts the spin-up (spin-down) bands. One can expect that the pattern of the band structure does not show significant changes between isoelectronic compounds. The case is different for Mn_2LiZ compounds with Z are Al, Ga and In around the Fermi energy despite having the same number of valence electrons. The Mn_2LiAl ompound exhibits SGS behavior with a large finite gap in spin-down bands, while an indirect zero gap in the spin-up bands with the top of the valence band at L-point while the bottom of the conduction band lies at X-point. The conduction band of the Mn_2LiGa compound in the spin-up channel is very dispersed so that the Fermi level well crosses it. For the spin-down bands, the Fermi energy falls in a gap far away from the top of the conduction band. As a result, the band structure of the Mn_2LiGa compound is almost similar to those showing spin semimetallicity behavior. By definition, spin semimetal compounds exhibit semimetallic behavior for one spin direction and show semiconductor character in the opposite one [130]. At finite temperature, the transport properties related to the SGS materials are also exhibited by spin semimetallic compounds, and they can show almost similar behavior. In the case of the Mn_2LiIn compound, the dispersion of the conduction band about the Fermi level increases in the spin-up direction, while the Fermi energy intersects the top of the valence band in the spin-down channel. Therefore, a metallicity is shown for this compound which is thermodynamically unstable. The presence of a band gap at the Fermi level appears to contribute to the chemical stability.

For spin-up direction, the conduction band along the Γ-X line becomes much wider if the atomic number of Z element increases. We attribute this to the increased hybridization along this line as we go down the same column of the periodic table. In the spin-down channel, the position of the top of the valence band changes from L to Γ point along the sequence Al-Ga-In. These behaviors are also observed for Mn_2LiZ (Z = Si, Ge and Sn) compounds in chapter 4, which are the characteristic of Mn_2LiZ compounds that seem to

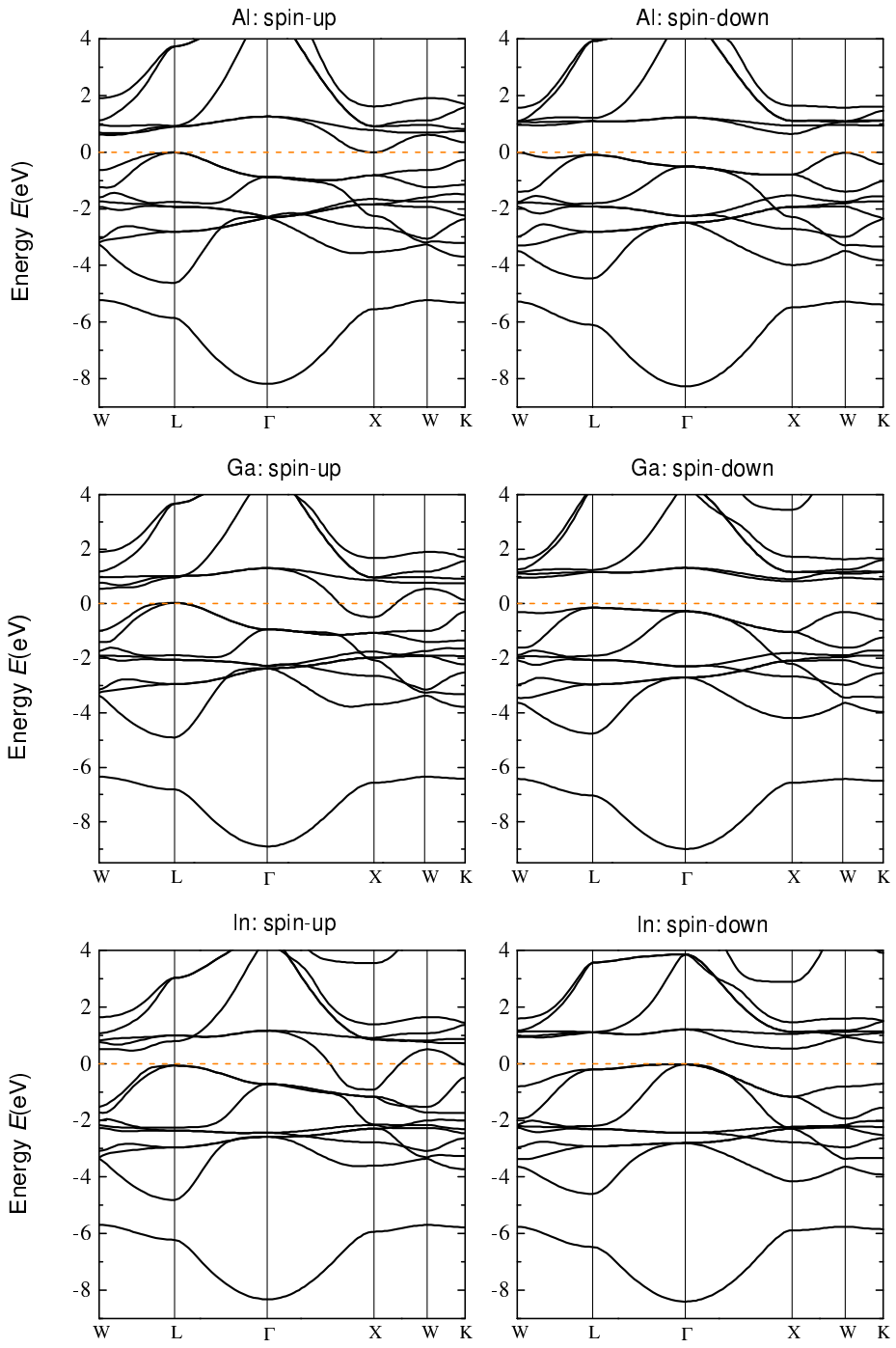

Figure 5.3: Calculated band structure for spin-up (left panel) and spin-down (right panel) of Mn_2LiZ (Z = Al, Ga and In).

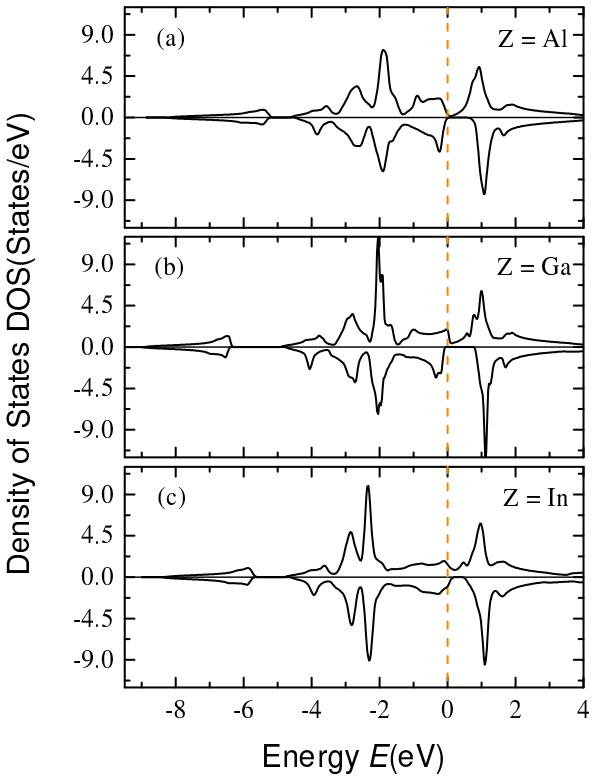

Figure 5.4: Total DOS of (a) Mn_2LiAl, (b) Mn2LiGa and (c) Mn2LiIn compounds. The dashed line indicates the Fermi level which is set to the origin.

be independent of the number of valence electrons.

The properties that appear on the band structure can be confirmed by the calculated density of states (DOS). Figure 5.4 depicts the results of the total DOS of the Mn_2LiZ compounds. Positive (negative) DOS is related to spin-up (spin-down) channels. The Mn_2LiAl and Mn_2LiGa compounds show a real band gap in the spin-down channel at the Fermi level. The case of the Mn_2LiGa compound is interesting because it shows a larger band gap of about 0.93 eV, which is attractive for retaining the high spin-polarization at elevated temperatures. The spin-down band gap of these two compounds is summarized in Table 5.2. In the case of spin-up direction, Mn_2LiAl presents a zero state (zero-gap) at the Fermi energy, confirming the SGS behavior of this compound, while small finite states are presented Mn_2LiGa. In the latter compound, the Fermi level is just near a region of small DOS. This small finite DOS forms a valley around the Fermi energy, which is the characteristic of semimetallic compounds, and hence the Mn_2LiGa compound is a nearly spin-semimetal. Mn_2LiIn compound displays a metallic behavior, where for both spin directions, there is a finite state at the Fermi energy.

For more comprehension of the band structure formation process of the present compounds, we calculated the atom-resolved DOS, and due to the similar behavior, we plot in Figure 5.5 only the results of that of Mn_2LiAl. As can be seen, the energy region

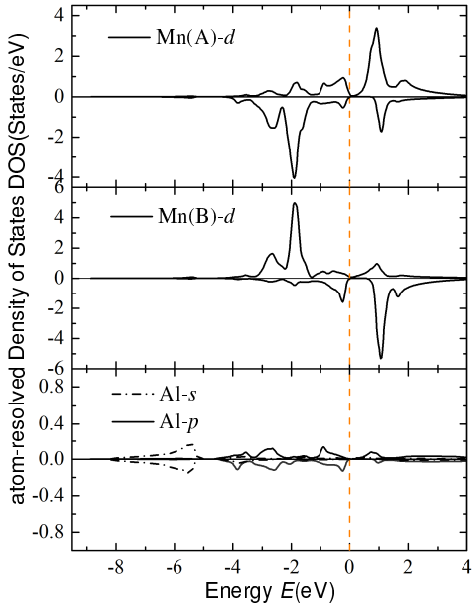

Figure 5.5: Atom-resolved DOS of the Mn_2LiAl compound.

from approximately -8 to -5 eV mainly originated from Al s states. This energy band is identical for both spin directions and is well separated by an energy gap from higher energy bands. These latter bands widen around the Fermi energy, which mainly arises from the hybridization of the two inequivalent Mn d states with the admixture of Sb p states. Although the crystal structure of Mn2LiZ compounds is full-Heusler structure, their electronic structure appears similar to those of half-Heusler compounds [74, 72]. The energy gap is formed in a way that is in-between the bonding (mainly contributed by Mn(A) atoms) and antibonding bands (mainly of Mn(B) atoms). The contribution from Lithium atom has little effect on the formation of the DOS and is not presented in Figure 5.5. The DOS of the bonding bands is mainly contributed by both the Mn(A) d spin-down states and Mn(B) d spin-up states. While the order is reversed in the region of antibonding bands, the contribution comes mainly from the Mn(A) d spin-up states and Mn(B) d spin-down states. This magneto-electronic behavior is ascribed to covalent magnetism [126].

For charge distribution, we calculated the electron density of all compounds. Figure 5.6 depicts the results plotted on the (011) surface plan. As for the case of Mn_2LiZ (Z = Si, Ge and Sn) compounds, the charge distributes considerably between Mn(A) and Mn(B) as well as between Mn(B) and Z, which is a characteristic of covalent bonding. The charge density in the middle of the Mn(A)-Mn(B) line is higher than that in-between Mn(B)-Z atoms, indicating a stronger covalent bonding between Mn(A) and Mn(B). We can see that the charge density in these regions decreases with increasing the atomic number of Z elements. However, around the Li atom, there is almost no charge distribution. This

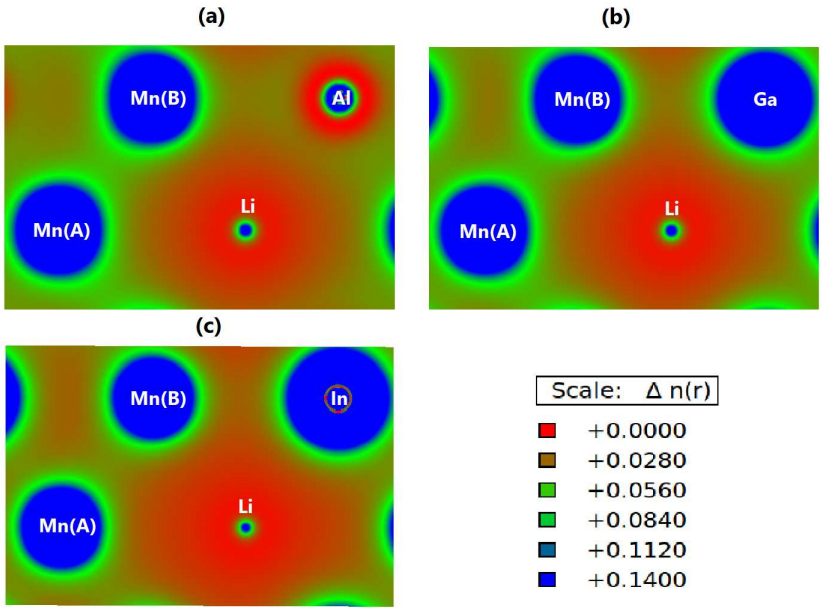

Figure 5.6: The distribution of the valence electron charge density of (a) Mn_2LiAl, (b) Mn_2LiGa and (c) Mn_2LiIn compound, plotted on the (011) surface.

indicates that electrons in this region are transferred from the more electropositive Li to the neighborhood elements. Thus the corresponding bondings are of ionic characters.

Finally, the total and atomic magnetic moments of the compounds are listed in Table 5.2. Interestingly, the net spin moment of both Mn_2LiAl and Mn_2LiGa compounds is exactly zero, while that of Mn_2LiIn considerably deviates from the zero value. The zero moments finding is expected because the valence electrons N of the present compounds is 18 per unit cell, and according to the Slater-Pauling rule $m = (N-18)\mu_B$, the compounds must exhibit a net spin moment of $0\mu_B$ per unit cell. Mn_2LiIn does not satisfy the Slater-Pauling rule because it has no energy gap at its Fermi level. The present zero-moment materials share the same behavior with the conventional antiferromagnets in that they have the same number of valence electrons for both spin directions. However,

Table 5.2: Calculated partial and total magnetic moments (in μ_B), spin-down band gaps (in eV) of Mn_2LiZ (Z= Al and Ga.

Compound	Mn(A)	Mn(B)	Z	Li	Interstitial	m	Gap
Mn_2LiAl	−2.24	2.32	−0.03	0.02	−0.08	0.00	0.67
Mn_2LiGa	−2.53	2.62	−0.02	0.02	−0.09	0.00	0.93
Mn_2LiIn	−3.06	3.24	−0.01	0.02	−0.07	0.12	—

due to non symmetrical band structures with respect to spin direction, the atomic (local) magnetic moments are coupled antiferromagnetically but with nearly (not exactly) the same absolute magnetic moments. The magnetic moments are confined at the A and B sublattices. The antiparallel alignment of these inequivalent sublattices leads to an incomplete compensation. Here, the exact compensation originates from the spin-down gap, which induces small magnetic moments in other sites such as Li, Z and the interstitial region, in order to reach the full compensation. This can be seen in Table 5.2.

5.4 Exchange interactions and Curie temperature

Exploring the exchange interactions is crucial for understanding magnetism and predicting the Curie temperature of the compounds. Thus, we present in Figure 5.7 the exchange coupling parameters for various cluster radius of the thermodynamically stable compounds, Mn_2LiAl and Mn_2LiGa. Because the self-consistent calculation does not converge at the equilibrium lattice parameter in the SPRKKR program, the results of the Mn_2LiAl compound are determined on a slightly expanded lattice parameter, about 0.51%. The results show that all the exchange interactions are confined within a cluster radius of less than $1.5a$. The Mn(A)-Mn(B) inter-sublattice exchange interaction dominates the exchange with a negative contribution, revealing the antiferromagnetic coupling of the corresponding Mn magnetic moments. Consequently, the antiferromagnetic inter-sublattice interaction stabilizes the ferrimagnetic order of the compounds. For the two compounds, the inter sublattice interaction shows almost similar patterns, they all present stronger interaction in the first coordination sphere (nearest-neighbor of Mn atom). However, their interaction drops significantly in the second sphere. Due to the smaller distance between the nearest neighbor of Mn in the Mn(A)-Mn(B) inter-sublattice, with about 2.54 Å, the inter-sublattice interaction is classified as direct. The Mn nearest-neighbor distance is critical for the existence of the direct interaction, and it is nearly equal for both compounds, which may explain the similar range order and strength of the Mn(A)-Mn(B) interaction.

We can see from Figure 5.7 that the intra-sublattice interactions are much weaker than the inter-sublattice ones. In contrast, intra-sublattice interactions are highly dependent on the Z atom, being stronger in Mn_2LiGa than in Mn_2LiAl. This can be explained by the fact that the Mn_2LiAl compound is a more semiconductor-type in which the indirect interactions (intra-sublattice interactions) are much weaker. The intra-sublattice exchange interactions in Mn_2LiGa are significantly larger due to the semimetallic behavior of the compound. For the two compounds, one observes that the two intra-sublattices

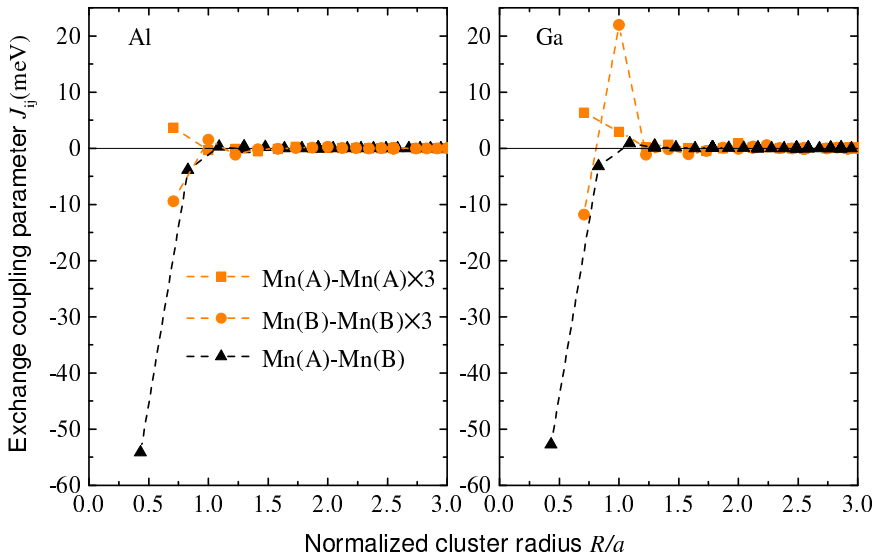

Figure 5.7: Exchange coupling parameters as a function of the normalized cluster radius of Mn_2LiZ (Z = Al and Ga)compounds. The intra-sublattice exchange interactions are multiplied by 3 for better illustration.

A and B show two distinct behaviors. The Mn(A)-Mn(A) interaction is positive for all coordination spheres. On the other hand, the Mn(B)-Mn(B) interaction displays an oscillatory behavior. It is negative in the first coordination sphere while positive in the second, and it is much weaker for other coordination spheres.

Due to the presence of the energy gap, all the exchange interactions decay rapidly with distance. Therefore only the first-nearest neighbor and second-nearest neighbor interactions can be significant [131].

The on-site sublattice interactions J_0 and the mean-field Curie temperature of both inter-sublattice T_C^{inter} and all-sublattices T_C^{all} are presented in Table 5.3. The calculated Curie temperature T_C^{all} of the two compounds is very high and reaches 1800 K. As we have seen, the inter-sublattice interaction that dominates in the exchange and its on-site interaction also exhibits a higher value for both compounds, resulting in a higher Curie temperature.

The special-chemical structure of Mn_2YZ, where Y is a magnetically inert element, is characterized by the very high Curie temperature [132]. The Y site may be empty or filled by the Li atom, for example. As an illustration, the calculated Curie temperature of Mn_2CoAl in Reference [50], determined by the same methodology as we used, is 890 K, which slightly deviates from the experimental one, 720 K [108]. The Mn_2LiAl compound can be viewed as Mn_2CoAl, with the Co being replaced by the Li atom. Interestingly, we

Table 5.3: Calculated $J_0^{\mathrm{Mn}(\mu)-\mathrm{Mn}(\nu)}$ onsite sublattices (in meV), inter-sublattice and all-sublattices mean field Curie temperature (in K) of Mn_2LiZ (Z=Al and Ga).

Compound	$J_0^{\mathrm{Mn(A)-Mn(A)}}$	$J_0^{\mathrm{Mn(B)-Mn(B)}}$	$J_0^{\mathrm{Mn(A)-Mn(B)}}$	$T_{\mathrm{C}}^{\mathrm{inter}}$	$T_{\mathrm{C}}^{\mathrm{all}}$
Mn_2LiAl	13.81	−41.44	−255.38	1973	1878
Mn_2LiGa	39.81	−14.42	−227.12	1755	1865

find that the consequence of this chemical substitution leads to the increase of the Curie temperature more than twice that of Mn_2CoAl.

The on-site intra-sublattice exchange interactions show opposite behaviors between the compounds. We obtain that intra-sublattice exchange interactions slightly reduce (enhance) the Curie temperature of Mn_2LiAl (Mn_2LiGa) compounds. Indeed, the sum of the two on-site intra-sublattice interactions is negative for Mn2LiAl while it is positive in the case of Mn2LiGa. Therefore negative intra-sublattice interaction destabilizes the antiferromagnetic inter-sublattice interaction. In conclusion, the intra-sublattice exchange interactions are less important for our compounds, and we can neglet them for determining the Curie temperature.

5.5 Thermoelectric transport

The temperature dependence of the electrical conductivity and Seebeck coefficient of the compounds are illustrated in Figure 5.8. As can be seen, the electrical conductivity of Mn_2LiAl shows non-metallic behavior because it increases rapidly with increasing temperature. The Mn_2LiAl compound has a predominantly semiconducting character, consistent with the electronic structure prediction of the spin-gapless semiconductivity. However, the electrical conductivity of Mn_2LiGa shows two different regimes as the temperature increases. At lower temperatures, the electrical conductivity is typical of metals, being mainly constant with increasing temperature. However, the conductivity increases linearly from approximately 150 K, showing the semiconductivity behavior.

In the lower panel of Figure 5.8, the Seebeck coefficient of the compounds is presented. The Seebeck coefficient of the two compounds is considerably larger and shows a positive value for a wide temperature range. In both compounds, the Seebeck coefficient increases with increasing temperature. For Al-based compound, it increases sharply from −100 to 100 μV/K at a small temperature range. The Mn_2LiAl compound shows an interesting thermoelectric behavior, with the Seebeck coefficient reaching about 175 μV/K at room temperature. This is typical of a potential p-type thermoelectric material.

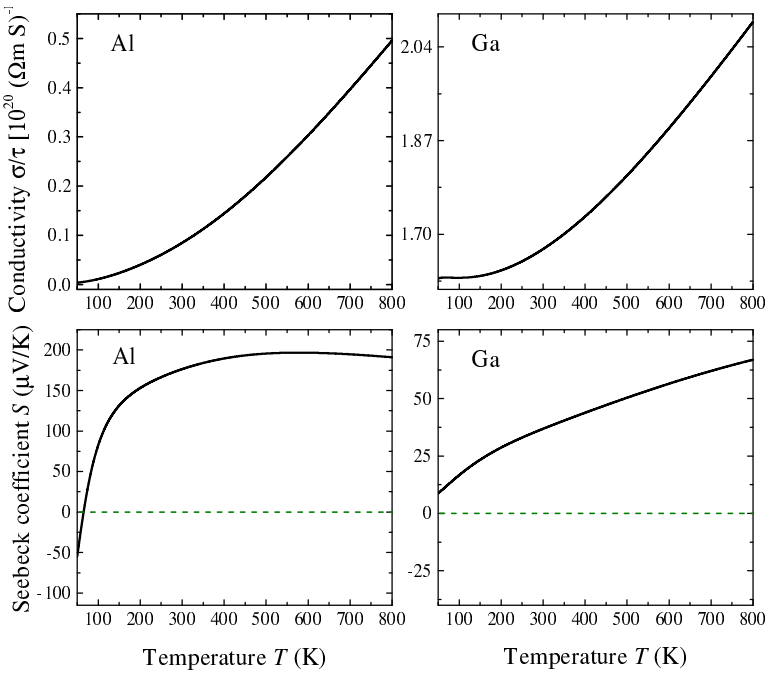

Figure 5.8: The temperature dependence of the conductivity integral σ/τ (upper panel) where τ is a relaxation time and Seebeck coefficient S (lower panel) of Mn_2LiZ (Z = Al and Ga).

Chapter 6

Summary and Conclusion

In this thesis, Li-based Heusler compounds are studied on their potential use in spintronics and thermoelectrics applications. We performed first-principles calculations to report various physical properties of the compounds, including structural, magneto-electronic, magnetic interaction and transport properties. In the framework of density functional theory, the electronic structure is done with the LAPW method. The exchange interactions are calculated in the real-space approach using the state-of-the-art KKR-GF method. We calculated the electron transport within the Boltzmann transport theory and determined the Curie temperature in the mean-field approximation.

First, the structural analysis shows that the compounds Mn_2LiZ (Z = Si, Ge, Sn, Al and Ga) are structurally and energetically stable in the inverse Heusler structure with the ferrimagnetic state. We obtained no stable tetragonal distortion and found that each compound can be lattice-matched with one of the zinc-blende semiconductors.

For Mn_2LiZ (Z = Si, Ge and Sn) compounds, the band structure reveals that all these compounds are half-metallic ferrimagnets with higher minority-band gaps and small net magnetic moments of μ_B. For electronic transport, the temperature dependence of the electrical conductivity shows a metallic behavior, and the spin-polarized current is still nearly 100% at room temperature based on the two current-model. The compounds present a weak contribution to the thermoelectric transport, except for Mn_2LiSn, which has a significant Seebeck coefficient at very high temperatures.

In the case of Mn_2LiZ (Z = Al and Ga) compounds, we predict unusual half-metallic properties. We found that the Mn_2LiAl compound exhibits a spin gapless semiconductivity, while Mn_2LiGa behaves as a spin semimetal compounds. Moreover, their ferrimagnetic structure is fully compensated, yielding a $0\mu_B$ total magnetic moments. Thanks to the lack of inversion symmetry, these compounds are fully spin-polarized at zero temperature, consistent with the Slater-Pauling rule. At elevated temperatures, we revealed

the semiconductor behavior of the compounds based on the relationship between electrical conductivity and temperature. In this study, much higher Seebeck coefficients are shown for these compounds for a wide temperature range, thanks to their semiconducting behavior at high temperatures.

The compounds studied in this work also present common features characteristic of the inverse Heusler structure. From the inspection of DOS, we found that the principal mechanism of minority-gap formation is the strong hybridization of d states of the inequivalent Mn atoms. The charge density distribution displays a covalent nature of some bonds while the ionic character for others. Interestingly, the compounds have high T_{C} , well above room temperature. This high value of T_{C} is a consequence of the strong Mn(A)-Mn(B) inter-sublattice exchange interaction. This interaction is antiferromagnetic and short-ranged (direct exchange).

Finally, we demonstrated several desirable properties in this study, including the half-metallicity, ferrimagnetism, zero spin moment, spin gapless semiconductivity, and importantly, the high Curie temperature that characterizes Mn_2LiZ (Z = Al, Ga, Si, Ge and Sn) compounds. For future work, it can be interesting to expand the search for spintronics materials to the Li-based Quaternary Heusler compounds. We emphasize that our predictive results can serve as a guide for future experimental work to fabricate and investigate our spintronics materials. Due to the structure compatibility of Mn_2LiZ compounds with Co_2LiZ and Ni_2LiZ non-magnetic Heusler compounds, it is desirable to study Mn_2LiZ/Co_2LiZ and Mn_2LiZ/Ni_2LiZ bilayers and test which parameters influence the spin polarization.

Bibliography

[1] Michel Julliere. Tunneling between ferromagnetic films. *Physics letters A*, **54**(3), 1975.

[2] LM Sandratskii. Thermal magnetic properties of the Ni sublattice in half-metallic NiMnSb : A theoretical study based on first-principles calculations. *Physical Review B*, **78**(2):094425, 2008.

[3] Jiangang He, S Shahab Naghavi, Vinay I Hegde, Maximilian Amsler, and Chris Wolverton. Designing and discovering a new family of semiconducting quaternary Heusler compounds based on the 18-electron rule. *Chemistry of Materials*, **30**(15):4978–4985, 2008.

[4] E. Schrdinger. Quantisierung als Eigenwertproblem. *Annalen Der Physik*, **79**:361–376, 1926.

[5] Max Born and Robert Oppenheimer. Zur Quantentheorie der Molekeln. *Annalen der Physik*, **389**:457–484, 1927.

[6] Vladimir Fock. Näherungsmethode zur Lösung des quantenmechanischen Mehrkörperproblems. *Zeitschrift für Physik*, **61**(1-2):126–148, 1930.

[7] Douglas R Hartree. The wave mechanics of an atom with a non-Coulomb central field. Part I. Theory and methods. In *Mathematical Proceedings of the Cambridge Philosophical Society*, volume **24**, pages 89–110. Cambridge university press, 1928.

[8] J. C Slater. A simplification of the Hartree-Fock method. *Physical review*, **81**(3):385, 1951.

[9] Pierre Hohenberg and Walter Kohn. Inhomogeneous electron gas. *Physical review*, **136**(3B):B864, 1964.

[10] Eberhard Engel and Reiner M Dreizler. *Density Functional Theory: An Advanced Course*. Theoretical and Mathematical Physics. Springer Berlin Heidelberg, Berlin, Heidelberg, 2013.

[11] James F Janak. Proof that $\frac{\partial E}{\partial n} = \varepsilon_i$ in density-functional theory. *Physical Review B*, **18**(12):7165, 1978.

[12] Kieron Burke and John Kozlowski. Lies My Teacher Told Me About Density Functional Theory: Seeing Through Them with the Hubbard Dimer. In Eva Pavarini and Erik Koch, editors, *Simulating Correlations with Computers*, volume **11** of *Schriften des Forschungszentrums Jülich Modeling and Simulation*, page 420, Jülich, 2021. Forschungszentrum Jülich GmbH Zentralbibliothek, Verlag.

[13] Ulf Von Barth and Lars Hedin. A local exchange-correlation potential for the spin polarized case. i. *Journal of Physics C: Solid State Physics*, **5**(13):1629, 1972.

[14] MM Pant and AK Rajagopal. Theory of inhomogeneous magnetic electron gas. *Solid State Communications*, **10**(12):1157–1160, 1972.

[15] Llewellyn H Thomas. The calculation of atomic fields. In *Mathematical proceedings of the Cambridge philosophical society*, volume **23**, pages 542–548. Cambridge University Press, 1927.

[16] Enrico Fermi. Eine statistische Methode zur Bestimmung einiger Eigenschaften des Atoms und ihre Anwendung auf die Theorie des periodischen Systems der Elemente. *Zeitschrift für Physik*, **48**(1-2):73–79, 1928.

[17] Paul AM Dirac. Note on exchange phenomena in the Thomas atom. In *Mathematical proceedings of the Cambridge philosophical society*, volume **26**, pages 376–385. Cambridge University Press, 1930.

[18] S. H. Vosko, L. Wilk, and M. Nusair. Accurate spin-dependent electron liquid correlation energies for local spin density calculations: a critical analysis. *Canadian Journal of Physics*, **58**(8):1200–1211, 1980.

[19] John P Perdew and Alex Zunger. Self-interaction correction to density-functional approximations for many-electron systems. *Physical Review B*, **23**:5048, 1981.

[20] G. Ortiz and P. Ballone. Correlation energy, structure factor, radial distribution function, and momentum distribution of the spin-polarized uniform electron gas. *Physical Review B*, **50**:1391, 1994.

[21] John P Perdew and Yue Wang. Accurate and simple analytic representation of the electron-gas correlation energy. *Physical review B*, **45**:13244, 1992.

[22] John P. Perdew, Kieron Burke, and Matthias Ernzerhof. Generalized Gradient Approximation Made Simple. *Physical review letters*, **77**:3865, 1996.

[23] John C Slater. Wave functions in a periodic potential. *Physical Review*, **51**(10):846, 1937.

[24] Terry L Loucks. *Augmented plane wave method: a guide to performing electronic structure calculations*. Number 28. WA Benjamin, New York, 1967.

[25] Ole Krogh Andersen. Linear methods in band theory. *Physical Review B*, **12**:3060–3083, 1975.

[26] David J Singh and Lars Nordstrom. *Planewaves, Pseudopotentials, and the LAPW method*. Springer US : Imprint: Springer, New York, NY, 2006.

[27] DR Hamann. Semiconductor charge densities with hard-core and soft-core pseudopotentials. *Physical Review Letters*, **42**(10):662, 1979.

[28] Erich Wimmer, Henry Krakauer, Michael Weinert, and AJ Freeman. Full-potential self-consistent linearized-augmented-plane-wave method for calculating the electronic structure of molecules and surfaces: O_2 molecule. *Physical Review B*, **24**(2):864, 1981.

[29] Hubert Ebert, Diemo Koedderitzsch, and Jan Minar. Calculating condensed matter properties using the KKR-Green's function methodrecent developments and applications. *Reports on Progress in Physics*, **74**(9):096501, 2011.

[30] Gerald Rickayzen. *Green's functions and condensed matter*. Techniques of physics ; 5. Academic Press, London, 1980.

[31] I. Mertig, E. Mrosan, and P. Ziesche. *Multiple Scattering Theory of Point Defects in Metals: Electronic Properties*. Teubner Verlag, Leipzig, 1987.

[32] J. Zabloudil, R. Hammerling, L. Szunyogh, and P. Weinberger. *Electron Scattering in Solid Matter: A Theoretical and Computational Treatise*, volume **147** of *Springer Series in Solid-State Sciences*. Springer Berlin Heidelberg, Berlin, Heidelberg, 2006.

[33] OK Andersen and RG Woolley. Muffin-tin orbitals and molecular calculations: General formalism. *Molecular Physics*, **26**(4):905–927, 1973.

[34] Yang Wang, GM Stocks, and JS Faulkner. General method for evaluating shape truncation functions of Voronoi polyhedra. *Physical Review B*, **49**(7):5028, 1994.

[35] B.L. Gyrffy and G.M. Stocks. Band theory for random metallic alloys. In P. Phariseau and L. Scheire, editors, *Electrons in finite and infinite structures*, volume **B24** of *NATO ASI Series, Physics, Plenum Press*, New York, 1977.

[36] J Korringa. On the calculation of the energy of a Bloch wave in a metal. *Physica*, **13**(6-7):392–400, 1947.

[37] Wo Kohn and No Rostoker. Solution of the schrödinger equation in periodic lattices with an application to metallic lithium. *Physical Review*, **94**(5):1111, 1954.

[38] Antonios Gonis and William H Butler. *Multiple Scattering in Solids*. Graduate Texts in Contemporary Physics. Springer, New York, 2000.

[39] N David Mermin. Thermal properties of the inhomogeneous electron gas. *Physical Review*, **137**(5A):A1441, 1965.

[40] J. K. Kübler. *Theory of itinerant electron magnetism*, volume **106** of *International series of monographs on physics*. Clarendon Press, Oxford, 2000.

[41] John C Slater. The ferromagnetism of nickel. *Physical Review*, **49**(7):537, 1936.

[42] JC Slater. Magnetic effects and the Hartree-Fock equation. *Physical Review*, **82**(4):538, 1951.

[43] Jenö Sólyom. *Fundamentals of the Physics of Solids: Volume I: Structure and Dynamics*. Springer Berlin Heidelberg, Berlin, Heidelberg, 2007.

[44] Robert M White. *Quantum theory of magnetism*. Springer Series in Solid-State Sciences. Springer Berlin Heidelberg, Berlin, Heidelberg, 2007.

[45] R. Skomski. *Simple Models of Magnetism*. Oxford Graduate Texts. Oxford University Press, Oxford, 2008.

[46] J.B. Goodenough. *Magnetism and the Chemical Bond*. Inorganic chemistry section. Interscience Publishers, New York, 1963.

[47] Kemal Özdoğan and Iosif Galanakis. Stability of spin-gapless semiconducting behavior in Ti_2CoSi, Ti_2MnAl, and Ti_2VAs Heusler compounds. *Physical Review Materials*, **5**(2):024409, 2021.

[48] P.W. Anderson. Theory of magnetic exchange interaction: exchange in insulators and semiconductors. In F. Seitz and D. Turnbull, editors, *Solid State Physics*, volume **14**, page 99214, New York, 1963. Academic Press.

[49] E Şaşioglu, LM Sandratskii, and P Bruno. First-principles study of exchange interactions and Curie temperatures of half-metallic ferrimagnetic full Heusler alloys Mn_2VZ (Z= Al, Ge). *Journal of Physics: Condensed Matter*, **17**(6):995, 2005.

[50] Markus Meinert, Jan-Michael Schmalhorst, and G. Reiss. Exchange interactions and Curie temperatures of Mn_2CoZ compounds. *Journal of Physics: Condensed Matter*, **23**(11):116005, 2011.

[51] Julie B Staunton. The electronic structure of magnetic transition metallic materials. *Reports on Progress in Physics*, **57**(12):1289, 1994.

[52] Phivos Mavropoulos. Multiscale Modelling of Magnetic Materials: From the Total Energy of the Homogeneous Electron Gas to the Curie Temperature of Ferromagnets. In Johannes Grotendorst, Norbert Attig, Stefan Blügel, and Dominik Marx, editors, *Multiscale Simulation Methods in Molecular Sciences- Lecture Notes*, volume **42** of *Publication Series of the John von Neumann Institute for Computing (NIC)*, Forschungszentrum Jülich, 2009.

[53] PH Dederichs, S Blügel, R Zeller, and H Akai. Ground states of constrained systems: Application to cerium impurities. *Physical review letters*, **53**(26):2512, 1984.

[54] NM Rosengaard and Börje Johansson. Finite-temperature study of itinerant ferromagnetism in Fe, Co, and Ni. *Physical Review B*, **55**(22):14975, 1997.

[55] SV Halilov, H Eschrig, A Ya Perlov, and PM Oppeneer. Adiabatic spin dynamics from spin-density-functional theory: Application to Fe, Co, and Ni. *Physical Review B*, **58**(1):293, 1998.

[56] LM Sandratskii and P Bruno. Exchange interactions and curie temperature in (Ga, Mn) As. *Physical Review B*, **66**(13):134435, 2002.

[57] J Kübler. Ab initio estimates of the Curie temperature for magnetic compounds. *Journal of Physics: Condensed Matter*, **18**(43):9795, 2006.

[58] A Il Liechtenstein, MI Katsnelson, VP Antropov, and VA Gubanov. Local spin density functional approach to the theory of exchange interactions in ferromagnetic metals and alloys. *Journal of Magnetism and Magnetic Materials*, **67**(1):65–74, 1987.

[59] A. K. Mackintosh and O. K. Andersen. The electronic structure of transition metals. In M. Springford, editor, *Electrons at the Fermi Surface*, page 149, Cambridge, 1975. Cambridge Press.

[60] A Oswald, R Zeller, PJ Braspenning, and PH Dederichs. Interaction of magnetic impurities in Cu and Ag. *Journal of Physics F: Metal Physics*, **15**(1):193, 1985.

[61] P Lloyd and PV Smith. Multiple scattering theory in condensed materials. *Advances in Physics*, **21**(89):69–142, 1972.

[62] http://olymp.cup.uni-muenchen.de/ak/ebert/SPRKKR.

[63] N. W. Ashcroft and N. D. Mermin. *Solid State Physics*. Saunders College, Philadelphia, 1976.

[64] M. P. Marder. *Condensed matter physics*. John Wiley, New York, 2000.

[65] Georg KH Madsen and David J Singh. BoltzTraP. A code for calculating band-structure dependent quantities. *Computer Physics Communications*, **175**(1):67–71, 2006.

[66] Nevill F Mott. Electrons in transition metals. *Advances in Physics*, **13**(51):325–422, 1964.

[67] Tanja Graf, Claudia Felser, and Stuart SP Parkin. Simple rules for the understanding of Heusler compounds. *Progress in solid state chemistry*, **39**(1):1–50, 2011.

[68] Sergey V Faleev, Yari Ferrante, Jaewoo Jeong, Mahesh G Samant, Barbara Jones, and Stuart SP Parkin. Origin of the tetragonal ground state of Heusler compounds. *Physical Review Applied*, **7**(3):034022, 2017.

[69] Lukas Wollmann, Stanislav Chadov, Jürgen Kübler, and Claudia Felser. Magnetism in tetragonal manganese-rich Heusler compounds. *Physical Review B*, **92**(6):064417, 2015.

[70] J Kübler, AR William, and CB Sommers. Formation and coupling of magnetic moments in Heusler alloys. *Physical Review B*, **28**(4):1745, 1983.

[71] C. Felser and A. Hirohata. *Heusler Alloys: Properties, Growth, Applications*. Springer Series in Materials Science. Springer International Publishing, 2015.

[72] I Galanakis, PH Dederichs, and NJPRB Papanikolaou. Origin and properties of the gap in the half-ferromagnetic Heusler alloys. *Physical Review B*, **66**(13):134428, 2002.

[73] Jianhua Ma, Vinay I Hegde, Kamaram Munira, Yunkun Xie, Sahar Keshavarz, David T Mildebrath, C Wolverton, Avik W Ghosh, and WH Butler. Computational investigation of half-Heusler compounds for spintronics applications. *Physical Review B*, **95**(2):024411, 2017.

[74] I Galanakis, PH Dederichs, and N Papanikolaou. Slater-Pauling behavior and origin of the half-metallicity of the full-Heusler alloys. *Physical Review B*, **66**(17):174429, 2002.

[75] GD Liu, XF Dai, HY Liu, JL Chen, YX Li, Gang Xiao, and GH Wu. Mn_2CoZ (Z= Al, Ga, In, Si, Ge, Sn, Sb) compounds: Structural, electronic, and magnetic properties. *Physical Review B*, **77**(1):014424, 2008.

[76] Hiroshi Itoh, Takurô Nakamichi, Yasuo Yamaguchi, and Noriaki Kazama. Neutron diffraction study of Heusler type alloy $Mn_{0.47}V_{0.28}Al_{0.25}$. *Transactions of the Japan institute of metals*, **24**(5):265–271, 1983.

[77] C Jiang, M Venkatesan, and JMD Coey. Transport and magnetic properties of Mn_2VAl: Search for half-metallicity. *Solid state communications*, **118**(10):513–516, 2001.

[78] Ruben Weht and Warren E Pickett. Half-metallic ferrimagnetism in Mn_2VAl. *Physical Review B*, **60**(18):13006, 1999.

[79] H Van Leuken and RA De Groot. Half-metallic antiferromagnets. *Physical review letters*, **74**(7):1171, 1995.

[80] K-W Lee and WE Pickett. Half semimetallic antiferromagnetism in the Sr_2CrTO_6 system (T= Os, Ru). *Physical Review B*, **77**(11):115101, 2008.

[81] N. Lakshmi, R. K. Sharma, and K. Venugopalan. Evidence of Clustering in Heusler like Ferromagnetic Alloys. *Hyperfine Interactions*, **160**:227233, 2005.

[82] Xuefang Dai, Guodong Liu, Lijie Chen, Jinglan Chen, and Guangheng Wu. Mn_2CoSb compound: Structural, electronic, transport and magnetic properties. *Solid state communications*, **140**(11-12):533–537, 2006.

[83] A Abada, K Amara, S Hiadsi, and B Amrani. First principles study of a new half-metallic ferrimagnets Mn_2-based full Heusler compounds: Mn_2ZrSi and Mn_2ZrGe. *Journal of Magnetism and Magnetic Materials*, **388**:59–67, 2015.

[84] Hongzhi Luo, Guodong Liu, Zhongqiu Feng, Yangxian Li, Li Ma, Guangheng Wu, Xiaoxi Zhu, Chengbao Jiang, and Huibin Xu. Effect of the main-group elements on the electronic structures and magnetic properties of Heusler alloys Mn_2NiZ (Z= In, Sn, Sb). *Journal of magnetism and magnetic materials*, **321**(24):4063–4066, 2009.

[85] L. Wollmann, S. Chadov, J. Kübler, and C. Felser. Magnetism in cubic manganese-rich Heusler compounds. *Physical Review B*, **90**(21):214420, 2014.

[86] Xiao-Ping Wei, Xian-Ru Hu, Ge-Yong Mao, Shi-Bing Chu, Tao Lei, Lei-Bo Hu, and Jian-Bo Deng. Half-metallic ferrimagnetism in Mn_2CuGe. *Journal of magnetism and magnetic materials*, **322**(20):3204–3207, 2010.

[87] H Zenasni, HI Faraoun, and C Esling. First-principle prediction of half-metallic ferrimagnetism in Mn-based full-Heusler alloys with highly ordered structure. *Journal of magnetism and magnetic materials*, **333**:162–168, 2013.

[88] HZ Luo, HW Zhang, ZY Zhu, L Ma, SF Xu, GH Wu, XX Zhu, CB Jiang, and HB Xu. Half-metallic properties for the Mn_2FeZ (Z= Al, Ga, Si, Ge, Sb) Heusler alloys: A first-principles study. *Journal of Applied Physics*, **103**(8):083908, 2008.

[89] Markus Meinert, Jan-Michael Schmalhorst, and Günter Reiss. Ab initio prediction of ferrimagnetism, exchange interactions and curie temperatures in Mn_2TiZ Heusler compounds. *Journal of Physics: Condensed Matter*, **23**(3):036001, 2010.

[90] Markus Meinert, Jan-Michael Schmalhorst, Christoph Klewe, Günter Reiss, Elke Arenholz, Tim Böhnert, and Kornelius Nielsch. Itinerant and localized magnetic moments in ferrimagnetic Mn_2CoGa thin films probed by x-ray magnetic linear dichroism: Experiment and ab initio theory. *Physical Review B*, **84**(13):132405, 2011.

[91] Hongzhi Luo, Fanbin Meng, Zhongqiu Feng, Yangxian Li, Wei Zhu, Guangheng Wu, Xiaoxi Zhu, Chengbao Jiang, and Huibin Xu. Ferromagnetism in the Mn-based Heusler alloy Mn_2NiSb. *Journal of Applied Physics*, **105**(10):103903, 2009.

[92] ST Li, Z Ren, XH Zhang, and CM Cao. Electronic structure and magnetism of Mn_2CuAl: A first-principles study. *Physica B: Condensed Matter*, **404**(14-15):1965–1968, 2009.

[93] ZQ Feng, HZ Luo, YX Wang, YX Li, W Zhu, GH Wu, and FB Meng. Phase stability and magnetic properties of the Heusler alloy Mn_2CuAl ribbons. *physica status solidi (a)*, **207**(6):1481–1484, 2010.

[94] Kaiming Cai, Zhifeng Zhu, Jong Min Lee, Rahul Mishra, Lizhu Ren, Shawn D Pollard, Pan He, Gengchiau Liang, Kie Leong Teo, and Hyunsoo Yang. Ultrafast and energy-efficient spin–orbit torque switching in compensated ferrimagnets. *Nature Electronics*, **3**(1):37–42, 2020.

[95] Zhendong Chen, Wenqing Liu, Peng Chen, Xuezhong Ruan, Jiabao Sun, Ruobai Liu, Cunxu Gao, Jun Du, Bo Liu, Hao Meng, et al. Direct observation of ferrimagnetic ordering in inverse Heusler alloy Mn_2CoAl. *Applied Physics Letters*, **117**(1):012401, 2020.

[96] Michelle E Jamer, Yung Jui Wang, Gregory M Stephen, Ian J McDonald, Alexander J Grutter, George E Sterbinsky, Dario A Arena, Julie A Borchers, Brian J Kirby, Laura H Lewis, et al. Compensated ferrimagnetism in the zero-moment heusler alloy Mn_3Al. *Physical Review Applied*, **7**(6):064036, 2017.

[97] Xingxing Li and Jinlong Yang. First-principles design of spintronics materials. *National Science Review*, **3**(3):365–381, 2016.

[98] I Galanakis, K Özdoğan, E Şaşıoğlu, and B Aktaş. Ab initio design of half-metallic fully compensated ferrimagnets: The case of Cr_2MnZ (Z= P, As, Sb, and Bi). *Physical Review B*, **75**(17):172405, 2007.

[99] I Galanakis, Kemal Özdoğan, and E Şaşıoglu. High-T_C fully compensated ferrimagnetic semiconductors as spin-filter materials: the case of CrVXAl (X= Ti, Zr, Hf) heusler compounds. *Journal of Physics: Condensed Matter*, **26**(8):086003, 2014.

[100] Rolf Stinshoff, Ajaya K Nayak, Gerhard H Fecher, Benjamin Balke, Siham Ouardi, Yurii Skourski, Tetsuya Nakamura, and Claudia Felser. Completely compensated ferrimagnetism and sublattice spin crossing in the half-metallic Heusler compound $Mn_{1.5}FeV_{0.5}Al$. *Physical Review B*, **95**(6):060410, 2017.

[101] Y Venkateswara, Sachin Gupta, S Shanmukharao Samatham, Manoj Raama Varma, KG Suresh, Aftab Alam, et al. Competing magnetic and spin-gapless semiconducting behavior in fully compensated ferrimagnetic CrVTiAl: Theory and experiment. *Physical Review B*, **97**(5):054407, 2018.

[102] Gregory M Stephen, Christopher Lane, Gianina Buda, David Graf, Stanislaw Kaprzyk, Bernardo Barbiellini, Arun Bansil, and Don Heiman. Electrical and magnetic properties of thin films of the spin-filter material CrVTiAl. *Physical Review B*, **99**(22):224207, 2019.

[103] Ersoy Şaşıoğlu. Nonzero macroscopic magnetization in half-metallic antiferromagnets at finite temperatures. *Physical Review B*, **79**(10):100406, 2009.

[104] XL Wang. Proposal for a new class of materials: spin gapless semiconductors. *Physical review letters*, **100**(15):156404, 2008.

[105] Xiaotian Wang, Zhenxiang Cheng, Gang Zhang, Hongkuan Yuan, Hong Chen, and Xiao-Lin Wang. Spin-gapless semiconductors for future spintronics and electronics. *Physics Reports*, **888**:1, 2020.

[106] Thorsten Aull, Ersoy Şaşıoğlu, Igor V Maznichenko, Sergey Ostanin, Arthur Ernst, Ingrid Mertig, and Iosif Galanakis. Ab initio design of quaternary Heusler compounds for reconfigurable magnetic tunnel diodes and transistors. *Physical Review Materials*, **3**(12):124415, 2019.

[107] Ersoy Şaşıoğlu, Thorsten Aull, Dorothea Kutschabsky, Stefan Blügel, and Ingrid Mertig. Half-Metal–Spin-Gapless-Semiconductor Junctions as a Route to the Ideal Diode. *Physical review applied*, **14**(1):014082, 2020.

[108] Siham Ouardi, Gerhard H Fecher, Claudia Felser, and Jürgen Kübler. Realization of spin gapless semiconductors: The Heusler compound Mn_2CoAl. *Physical review letters*, **110**(10):100401, 2013.

[109] S Skaftouros, Kemal Özdoğan, E Şaşıoğlu, and I Galanakis. Search for spin gapless semiconductors: The case of inverse heusler compounds. *Applied Physics Letters*, **102**(2):022402, 2013.

[110] Adam Jakobsson, Phivos Mavropoulos, E Şaşıoğlu, S Blügel, M Ležaić, Biplab Sanyal, and Iosef Galanakis. First-principles calculations of exchange interactions, spin waves, and temperature dependence of magnetization in inverse-Heusler-based spin gapless semiconductors. *Physical Review B*, **91**(17):174439, 2015.

[111] Joachim Barth, Gerhard H Fecher, Benjamin Balke, Siham Ouardi, Tanja Graf, Claudia Felser, Andrey Shkabko, Anke Weidenkaff, Peter Klaer, Hans J Elmers,

et al. Itinerant half-metallic ferromagnets Co_2TiZ (Z= Si, Ge, Sn): Ab initio calculations and measurement of the electronic structure and transport properties. *Physical Review B*, **81**(6):064404, 2010.

[112] Guanhua Qin, Wei Ren, and David J Singh. Interplay of local moment and itinerant magnetism in cobalt-based Heusler ferromagnets: Co_2TiSi, Co_2MnSi and Co_2FeSi. *Physical Review B*, **101**(1):014427, 2020.

[113] A Hamzic, R Asomoza, and IA Campbell. The transport properties of Heusler alloys:'ideal' local moment ferromagnets. *Journal of Physics F: Metal Physics*, **11**(7):1441, 1981.

[114] Y Ishikawa. Differing degrees of itinerancy in $3d$ alloys revealed by measurements of neutron spin wave scattering. *Physica B+ C*, **91**:130–137, 1977.

[115] E Şaşıoğlu, LM Sandratskii, and P Bruno. Role of conduction electrons in mediating exchange interactions in Mn-based Heusler alloys. *Physical Review B*, **77**(6):064417, 2008.

[116] A Mewis and H-U Schuster. Die Struktur der Phasen $LiCo_2Ge$ und $LiNi_2Sn$/The Structure of the Phases $LiCo_2Ge$ and $LiNi_2Sn$. *Zeitschrift für Naturforschung B*, **26**(1):62–62, 1971.

[117] Weibo Yao, Jie Zhou, Dongwen Zeng, Huijun Wan, Wen Ruan, Lina Liu, and Yufeng Wen. Computational discovery of the novel half-metallic full-Heusler alloys Mn_2LiAs and Mn_2LiSb. *Journal of Magnetism and Magnetic Materials*, 503:166642, 2020.

[118] P. Blaha, K. Schwarz, G. K. H. Madsen, D. Kvasnicka, J. Luitz, R. Laskowski, F. Tran, and L. D. Marks. ***WIEN2k****, An Augmented Plane Wave + Local Orbitals Program for Calculating Crystal Properties.* (Karlheinz Schwarz, Vienna University of Technology, Austria), 2018.

[119] Peter Blaha, Karlheinz Schwarz, P Sorantin, and SB Trickey. Full-potential, linearized augmented plane wave programs for crystalline systems. *Computer physics communications*, **59**(2):399–415, 1990.

[120] Tariq Hadji, Hafid Khalfoun, Habib Rached, and Ahmed Azzouz-Rached. Ab-initio prediction of high t_C half-metallic ferrimagnetism in Li-based heusler compounds Mn_2LiZ (Z= Si, Ge and Sn). *Computational Condensed Matter*, **27**:e00557, 2021.

[121] Shu-Chun Wu, Gerhard H Fecher, S Shahab Naghavi, and Claudia Felser. Elastic properties and stability of Heusler compounds: Cubic Co_2YZ compounds with $L2_1$ structure. *Journal of Applied Physics*, 125(8):082523, 2019.

[122] M. Born and K. Huang. *Dynamical Theory of Crystal Lattices*. Clarendon Press, Oxford, 1956.

[123] Scott Kirklin, James E Saal, Bryce Meredig, Alex Thompson, Jeff W Doak, Muratahan Aykol, Stephan Rühl, and Chris Wolverton. The Open Quantum Materials Database (OQMD): assessing the accuracy of DFT formation energies. *npj Computational Materials*, **1**(1):1–15, 2015.

[124] http://www.oqmd.org.

[125] Jianhua Ma, Jiangang He, Dipanjan Mazumdar, Kamaram Munira, Sahar Keshavarz, Tim Lovorn, C Wolverton, Avik W Ghosh, and William H Butler. Computational investigation of inverse Heusler compounds for spintronics applications. *Physical Review B*, **98**(9):094410, 2018.

[126] AR Williams, R Zeller, VL Moruzzi, CD Gelatt Jr, and J Kubler. Covalent magnetism: An alternative to the Stoner model. *Journal of Applied Physics*, **52**(3):2067–2069, 1981.

[127] V. Popescu, P. Kratzer, S. Wimmer, and H. Ebert. Native defects in the Co_2TiZ ($Z = Si, Ge, Sn$) full Heusler alloys: Formation and influence on the thermoelectric properties. *Physical Review B*, **96**:054443, 2017.

[128] Tariq Hadji, Hafid Khalfoun, Habib Rached, and Ahmed Azzouz-Rached. Spin gapless semiconductor and nearly spin semimetal antiferromagnets: The case of the inverse heusler compounds Mn_2LiZ (Z= Al and Ga). *Materials Research Bulletin*, 143:111461, 2021.

[129] M. Tas, E. Şaşıoğlu, C. Friedrich, S. Blügel, and I. Galanakis. Design of $L2_1$-type antiferromagnetic semiconducting full-Heusler compounds: A first principles DFT + GW study. *Journal of Applied Physics*, **121**:053903, 2017.

[130] Y. Venkateswara, S. Shanmukharao Samatham, P. D. Babu, K. G. Suresh, and Aftab Alam. Coexistence of spin semimetal and Weyl semimetal behavior in FeRhCrGe. *Physical Review B*, **100**:180404(R), 2019.

[131] J. Rusz, L. Bergqvist, J. Kudrnovský, and I. Turek. Exchange interactions and Curie temperatures in $Ni_{2-x}MnSb$ alloys: First-principles study. *Physical Review B*, **73**:214412, 2006.

[132] I. Galanakis, K. Özdoğan, and E. Şaşıoğlu. Half-metallic antiferromagnetism in $Cr_{2+x}Se$ ($0 \leq x \leq 1$): A first-principles study. *Physical Review B*, **86**:134427, 2012.